Nuclear Compton scattering from ^{12}C

Author:
Markus F. Preston

Supervisor:
Kevin G. Fissum

Master's Degree Project

June 10, 2014

LUNDS UNIVERSITET
Naturvetenskapliga fakulteten

MAX IV
LABORATORY

Abstract

Nuclear Compton scattering — the elastic scattering of photons — from ^{12}C has been studied at the Tagged-Photon Facility at MAX IV in Lund, Sweden. The differential cross section for the reaction was determined at laboratory angles of 60° and 120° in the energy range 65-95 MeV. The cross section for nuclear Compton scattering is related to the electric and magnetic polarisabilities of the proton and the neutron. The polarisabilities are fundamental structure constants that describe how nucleons are affected by an external electromagnetic field. The determination of the electric and magnetic polarisabilities of the neutron through measurements of the deuterium Compton scattering cross section is the goal of a recent large scale experimental effort spanning almost a decade at the Tagged-Photon Facility at MAX IV. The purpose of this experiment was twofold: to verify the procedure for normalisation of Compton scattering data by investigating ^{12}C and comparing to a well-established and comprehensive existing body of data, and to determine whether the electric and magnetic polarisabilities of free nucleons are affected when they are bound inside a nucleus.

Populärvetenskaplig sammanfattning

En stor del av dagens forskning inom kärn- och partikelfysik behandlar de fyra fundamentala naturkrafterna: den starka växelverkan, den svaga växelverkan, elektromagnetismen och gravitationen. Den starka växelverkan beskrivs idag av teorin QCD (Quantum ChromoDynamics, kvantkromodynamik), i vilken sex kvarkar växelverkar med hjälp av den masslösa partikeln gluonen. Dessa partiklar utgör byggstenarna i bland annat protonen och neutronen, två partiklar som tillsammans brukar kallas nukleoner. Nukleonerna utgör i sin tur byggstenarna i atomkärnan, ett fysikaliskt system på femtometerskalan (1 femtometer = 0.000000000000001 meter).

Trots att QCD erbjuder en metod för att utföra beräkningar på system som påverkas av den starka växelverkan, gör den starka växelverkans natur dessa beräkningar väldigt tidskrävande. Detta gäller särskilt för system inom kärnfysiken, då dessa innehåller väldigt många kvarkar som är bundna i nukleoner. Metoder håller på att utvecklas för att beskriva sådana system (ett exempel är kiral effektiv fältteori, χEFT), och för att kontrollera dessa modellers riktighet krävs kärnfysikaliska experiment.

MAX IV i Lund är den nationella elektronacceleratoranläggningen i Sverige. Elektronerna, som accelereras upp till hastigheter nära ljusets, används i forskning inom många olika områden. Ett av dessa är produktion av högenergetiska fotoner. Energin på dessa fotoner är sådan ($\sim$100 MeV) att fotonerna lämpar sig utmärkt för experiment som kan användas för att testa χEFT.

Under det senaste decenniet har ett experimentellt program genomförts på MAX IV med syftet att bestämma neutronens polariserbarhet. Protonens och neutronens polariserbarhet är kopplad till hur partiklarna inuti nukleonen — alltså partiklarna inom QCD — reagerar på ett externt elektromagnetiskt fält. Nukleonens polariserbarhet är en naturkonstant som beror på partikelns inre struktur, och som kan användas för att testa χEFT. Målet med experimenten på MAX IV har varit att bestämma tvärsnittet[1] för Comptonspridning — elastisk spridning av fotoner — från deuterium. Deuterium är den lättaste atomkärnan innehållande en neutron, och tvärsnittet för Comptonspridning är direkt relaterat till neutronens polariserbarhet.

Eftersom tvärsnittet för Comptonspridning från deuterium är mycket litet, krävs en noggrann undersökning av huruvida analysmetoden som används är korrekt. Denna undersökning görs genom att studera Comptonspridning från kol-12; en reaktion med betydligt större tvärsnitt. I denna uppsats presenteras resultaten av en analys av sådana mätningar genomförda på MAX IV. Under experimentet skickades en stråle av fotoner i energiområdet 60-100 MeV mot ett stycke grafit, i vilket en liten andel av fotonerna sedan genomgick den önskade reaktionen. Fotonerna som spridits elastiskt detekterades sedan med stora fotondetektorer av natriumjodid-kristall.

Utöver att användas som en bekräftelse av analysmetoden, kan resultaten även användas för att undersöka hur nukleonernas polariserbarhet påverkas då nukleonerna är bundna i en atomkärna.

[1] Tvärsnittet för en reaktion är ett mått på hur sannolik en reaktion är.

Contributions of the Author

During the execution of this project, the author of this thesis

- assisted in the setup of the experiment, including
  - moving the photon detectors.
  - repairing the in-beam monitor detector.
  - connecting the data-acquisition electronics to the detectors.
  - setting up the Pb-glass detector before tagging-efficiency measurements.
- sat data-acquisition shifts during the experimental run.
- performed a complete analysis of ^{12}C Compton scattering data.
  - Used C++ and the analysis framework ROOT.
  - Improved the calibration analysis software to allow for improved energy resolution.
  - Performed extensive simulations of the experimental setup using GEANT4 and a Monte Carlo simulation of the focal-plane electronics.
  - Demonstrated internal self-consistency between single-hit TDC data and multi-hit TDC data obtained at very high rates (see publication 1 below).
  - Extracted absolute differential cross sections for single-hit TDC data and multi-hit TDC data obtained at very high rates (see publication 2 below).
- consulted on Compton scattering data analysis issues with American undergraduate students taking part in the U. S. National Science Foundation's International Research Experience for Students exchange program.
- presented results as a speaker at two conferences:
  - Nordic Physics Days, June 2013, Lund, Sweden.
  - Swedish Nuclear Physicists Meeting, November 2013, Stockholm, Sweden.
- published two articles in peer-reviewed journals (see App. B).
  - M. F. Preston, ..., *Nucl. Instrum. Methods Phys. Res. Sect. A* **744**, 17 (2014)
  - ..., M. F. Preston, ..., *Phys. Rev. C* **89**, 035202 (2014)

Acknowledgements

I would like to start by thanking my supervisor Kevin Fissum, to whom I am very grateful for his constant encouragement during the past two years, and for all support during the writing of this thesis. A big thank you goes to Luke Myers at Jefferson Lab, who has invested much time in helping me with the analysis procedure — especially the software and the simulations involved. Without you this work would not have been possible. Thank you to the people from the University of Glasgow, especially to John Annand for involving me in the original experiment in 2012, and for showing an interest in the progress of my analysis over the course of this project. Thanks also to Seian Al Jebali, Jason Brudvik, Mohsen Meshkian and Magnus Lundin for helping with and answering questions about the electronics, tagging efficiency and the GEANT4 simulation. Thanks to Julius Scherzinger and Samuel Bengtsson. I am grateful to the Data Management and Software Centre, a Danish Contribution to the European Spallation Source ESS AB, for generously providing access to their computations cluster. Finally, I am grateful to Olivia for her support in everything.

Contents

List of Tables

List of Figures

List of Abbreviations

ADC	Analog-to-digital converter
χEFT	Chiral effective field theory
CW	Continuous wave
DAQ	Data acquisition
EM	Electromagnetic
FP	Focal plane
FWHM	Full width at half maximum
LEX	Low-energy expansion
LINAC	Linear accelerator
ME	Missing energy
MeV	Mega electron volt
NaI(Tl)	Sodium Iodide (Thallium activated)
Pb-glass	Lead glass
PMT	Photomultiplier tube
PSR	Pulse-stretcher ring
ROI	Region of integration
QCD	Quantum chromodynamics
QED	Quantum electrodynamics
TDC	Time-to-digital converter
TPF	Tagged-photon facility

Chapter 1

Introduction

1.1 Models of the nucleon

Nucleons — protons and neutrons — were among the first subatomic particles to be experimentally observed. Nucleons make up the atomic nucleus, and were until the 1960s thought of as elementary (point-like) particles, thereby having no internal structure. In the mid-1930s, just a few years after the first observation of the neutron by Chadwick in 1932, Yukawa [1] suggested that the attractive force between the nucleons was mediated via the exchange of massive virtual particles called π mesons. In 1947, the existence of such particles was confirmed experimentally [2], stimulating work in the field of hadronic structure.

In 1964, Gell-Mann [3] and Zweig [4] each independently proposed the Quark Model to describe hadronic structure, in which new elementary particles called quarks were introduced. According to this model, the quarks (together with their antiparticles) combine to form hadrons. Hadrons may be classified as baryons or mesons depending on the number of quarks/antiquarks that are combined. A baryon (such as a proton or neutron) consists of three quarks, while a meson such as the π meson consists of a quark and an antiquark. Table 1.1 lists some of the basic properties of the nucleons.

Particle	Symbol	Quark content[1]	Rest mass [MeV/c^2]	Charge [e]
Proton	p	uud	938.3	+1
Neutron	n	udd	939.6	0

[1] See Table 1.2 for further details.

Table 1.1: Basic properties of nucleons.

Subsequent to the proposal of the quarks as the fundamental building blocks of hadrons, the theory of Quantum Chromodynamics (QCD) was developed. QCD describes the strong interaction; that is, the interaction between quarks. It also introduces the gluon, a massless particle that mediates the strong interaction. Table 1.2 lists the particles of QCD. The concept of a massless force mediator is very similar to the situation in the highly successful Quantum Electrodynamics (QED) theory, in which photons act as force mediators between

Type	Particle	Symbol	Bare mass [MeV/c^2]	Charge [e]
Quark	up quark	u	1.5-3.3	+2/3
	down quark	d	3.5-6.0	-1/3
	charm quark	c	1,160-1,340	+2/3
	strange quark	s	70-130	-1/3
	top quark	t	169,100-173,300	+2/3
	bottom quark	b	4,130-4,370	-1/3
Force mediator	gluon	g	0	0

Table 1.2: Basic properties of the particles of QCD.

charged particles. However, the exact nature of the strong force makes it much more difficult to study theoretically than QED. QCD calculations of many-nucleon systems are highly demanding for two reasons. First, since each nucleon consists of three quarks, even the simple two-nucleon system deuterium which contains one proton and one neutron becomes a six-body problem on the quark scale. Second, the strong interaction is unique among the fundamental forces in that it grows stronger as the energy of the system decreases. Thus, the force mediated by the gluons will be very strong at the energy scale of nuclear physics, and the perturbative techniques which are successfully employed in QCD calculations at a higher energy scale may not be employed. The most popular method for calculations involving few-nucleon systems in the low-energy regime of QCD is Chiral Effective Field Theory (χEFT). In χEFT, the symmetries of QCD are utilised such that the number of possible interactions are restricted, so that the quark and gluon fields of QCD may be replaced by hadronic degrees-of-freedom and the QDC Lagrangian density may be replaced by an effective Lagrangian density. The details of this theory are beyond the scope of this work[1].

1.2 Nucleon polarisabilities

As explained in Sec. 1.1, nucleons are non-fundamental particles consisting of charged particles known as quarks. Any system of charged particles is affected by an external electromagnetic (EM) field. Applying an EM field to such a system will induce an electric dipole moment $\vec{p}$ and a magnetic moment $\vec{m}$. The induced moments are related to the applied fields by two parameters, the electric (α) and magnetic (β) polarisabilities. These are in turn related to the applied electric and magnetic fields $\vec{E}$ and $\vec{B}$ and the induced moments by

$$\vec{p} = \alpha \vec{E} \tag{1.1}$$

$$\vec{m} = \beta \vec{B}. \tag{1.2}$$

In Fig. 1.1, the response of the systems to the applied fields is shown. The induced electric dipole moment originates in the alignment of the charges with the electric field so

[1]See for example Ref. [5] for further details.

that $\vec{p}$ points in the same direction as $\vec{E}$. The induced magnetic moment has two components: paramagnetic and diamagnetic. The paramagnetic component originates in the alignment of the intrinsic magnetic moments of the particles with the magnetic field, meaning that the paramagnetic portion of $\vec{m}$ points in the same direction as $\vec{B}$. The diamagnetic component originates in the current induced in the system of charges by $\vec{B}$, which in turn induces a magnetic field and moment directed opposite to that of $\vec{B}$ according to Lenz's law [6]. Thus, the polarisability parameters α and β are measures of how strongly a system of charged particles is affected by the applied fields. By determining these parameters, information may be obtained on the internal structure of the system. As nucleons are composite particles consisting of charged quarks while the neutron is neutral as a whole, the particles on the sub-nucleon scale are all charged. As such, both the proton and the neutron have associated polarisability parameters which can provide information on internal nucleon structure.

1.3 Compton scattering

The elastic scattering of photons from electrons was first described by Compton [7] in 1923 using a quantum-mechanical treatment of electromagnetic radiation and a relativistic treatment of the electron. Since kinetic energy and momentum must be conserved in such a process, the target electron will recoil, and the photon will scatter with a lower energy and thus a longer wavelength than it had before the collision. Fig. 1.2 shows the process of Compton scattering.

The term Compton scattering is also used in the context of elastic scattering of a high-energy photon from a nucleon or atomic nucleus. In his original paper, Compton derived the relationship between the wavelength shift of the photon and the scattering angle. The derivation is exactly the same in the case of nuclear Compton scattering except that the electron mass is replaced by the mass of the nucleon or nucleus. Further, in the context of this work, it is more meaningful to describe the process in terms of a shift in photon energy given by

$$\omega' = \frac{\omega}{1 + (\omega/M) \cdot (1 - \cos\theta)} \tag{1.3}$$

rather than wavelength. It can be seen that the energy ω' of the photon after scattering is related to the pre-scattering photon energy ω, the target mass M and the scattering angle θ.

1.3.1 Nucleon Compton scattering

Compton scattering may be utilised to probe the internal structure of nucleons. However, this is only the case if the photon energy is sufficiently high for the Compton scattering process to depend on parameters describing the interior of the nucleon. The differential cross section for photon scattering from a structureless spin-$\frac{1}{2}$ particle with an anomalous

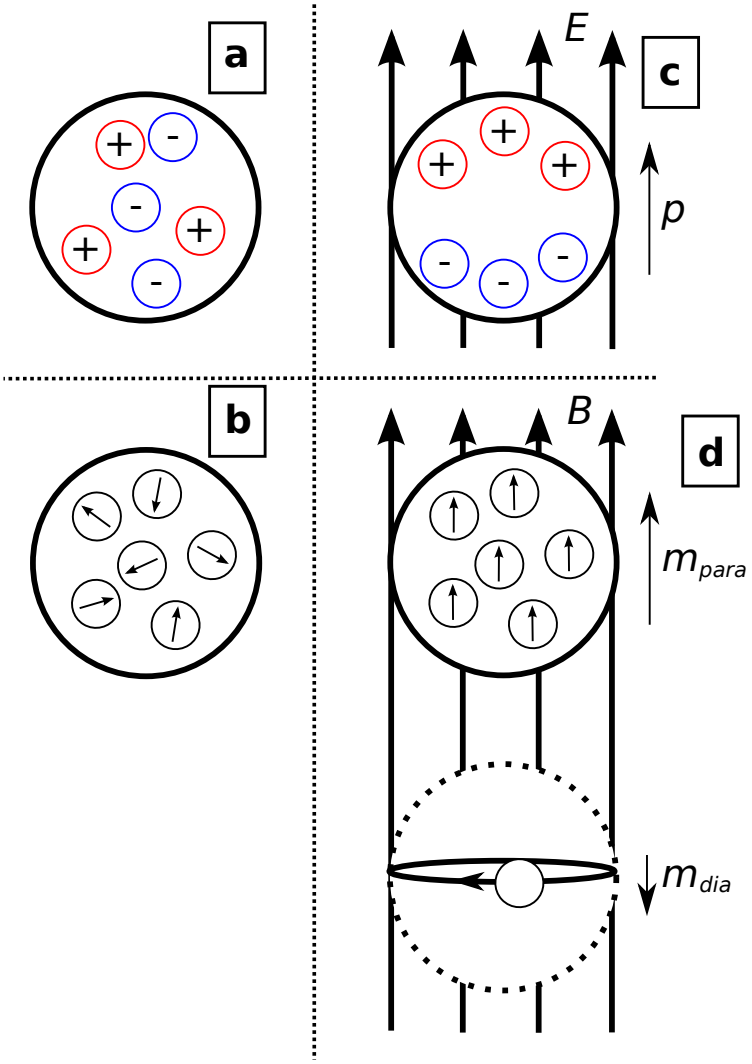

Figure 1.1: The response of a charged-particle system to an external EM field. In cases (a) and (b), no field is applied, and there are no induced electric or magnetic moments. In case (c), an external electric field has been applied inducing an electric dipole moment $\vec{p}$. In case (d), an external magnetic field has been applied inducing a magnetic moment $\vec{m}$ consisting of a paramagnetic and a diamagnetic term. The total magnetic moment $\vec{m}$ is given by the sum of the paramagnetic and diamagnetic terms. See text for details.

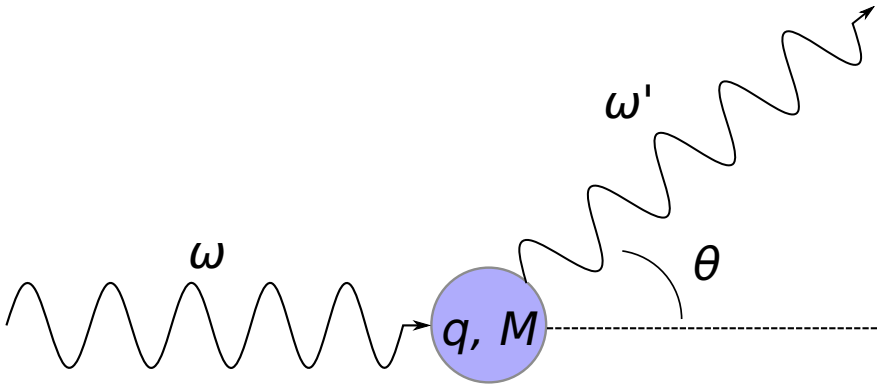

Figure 1.2: Compton scattering of a photon off a particle with mass M and charge q. The scattering results in a decrease in photon energy according to Eq. 1.3.

magnetic moment λ was calculated by Powell [8] to be

$$\begin{aligned}\left(\frac{d\sigma}{d\Omega}\right)_{\text{Powell}} =& \frac{1}{2}\left(\frac{q^2}{M\,c^2}\right)^2\left(\frac{\omega'}{\omega}\right)^2\left\{\left[\frac{\omega}{\omega'}+\frac{\omega'}{\omega}-\sin^2\theta\right]\right. \\ &+\lambda\left[\left(\frac{2\omega'\,\omega}{M^2\,c^4}\right)(1-\cos\theta)^2\right] \\ &+\lambda^2\left[\left(\frac{\omega'\,\omega}{M^2\,c^4}\right)\left(4(1-\cos\theta)+\frac{1}{2}(1-\cos\theta)^2\right)\right] \\ &+\lambda^3\left[\left(\frac{\omega'\,\omega}{M^2\,c^4}\right)\left(2(1-\cos\theta)+\sin^2\theta\right)\right] \\ &\left.+\lambda^4\left[\left(\frac{\omega'\,\omega}{2\,M^2\,c^4}\right)\left(1+\frac{1}{2}\sin^2\theta\right)\right]\right\}.\end{aligned} \tag{1.4}$$

where q is the nucleon charge, M is the nucleon mass, c is the speed of light in vacuum, ω (ω') is the photon energy before (after) scattering, θ is the scattering angle, and λ is the anomalous magnetic moment of the nucleon. The Powell cross section equation is valid only for nuclear Compton scattering in the region below 20 MeV [9]. At photon energies above 20 MeV but still far below the π-production threshold at $\sim$140 MeV, the differential cross section becomes sensitive to the properties of the interior of the nucleon, and is given by the Low Energy Expansion (LEX) [10]

$$\begin{aligned}\left(\frac{d\sigma}{d\Omega}\right)_{\text{LEX}} =& \left(\frac{d\sigma}{d\Omega}\right)_{\text{Powell}} - \frac{q^2}{M\,c^2}\left(\frac{\omega'}{\omega}\right)^2\left(\frac{\omega'\,\omega}{(\hbar\,c)^2}\right) \\ &\times\left(\frac{\alpha_N+\beta_N}{2}(1+\cos\theta)^2+\frac{\alpha_N-\beta_N}{2}(1-\cos\theta)^2\right).\end{aligned} \tag{1.5}$$

The differential cross section for nuclear Compton scattering in the LEX contains both the point-like Powell cross section which does not take into account any sub-nucleon structure

and a second term which allows for sub-structure of the nucleon[2]. In addition to the previously defined variables, this second term contains the reduced Planck constant $\hbar$, and the electric (magnetic) polarisability α_N (β_N) of the nucleon. Thus, if the cross section for Compton scattering off the nucleon at photon energies below 100 MeV — the photon energy range in which the LEX is valid [10] — can be measured, the polarisabilities of the nucleon may be extracted. Compton scattering is thus a valuable tool for determining these fundamental structure constants.

Eq. 1.5 does not lead to singular values for α_N and β_N, but rather includes a combination of the two. Therefore other means are needed for constraint. For this purpose, the Baldin sum rule [12] is often used

$$\alpha + \beta = \frac{1}{2\pi^2} \int_{\omega_{\text{th}}}^{\infty} \frac{\sigma_\gamma(\omega)}{\omega^2} \, \mathrm{d}\omega. \tag{1.6}$$

Here, α and β are the polarisabilities, $\sigma_\gamma(\omega)$ is the total photoabsorption cross section for the nucleon, and ω_{th} is the pion photoproduction threshold energy. By applying Eq. 1.5 and Eq. 1.6 to existing experimental data for photon scattering from hydrogen, the electric and magnetic polarisabilities for the proton have been determined to be (in units of 10^{-4} fm^3) [13]

$$\alpha_p = 10.7 \pm 0.3_{\text{stat}} \pm 0.2_{\text{BSR}} \pm 0.8_{\text{th}}$$
$$\beta_p = 3.1 \mp 0.3_{\text{stat}} \pm 0.2_{\text{BSR}} \pm 0.8_{\text{th}}.$$

Here, the first uncertainty is statistical, the second comes from uncertainties in the Baldin sum rule, and the third is due to uncertainty in the theory.

The situation for the neutron is more complex. While hydrogen targets are readily available, there are no free-neutron targets. In addition, if one were able to perform Compton scattering experiments off a free neutron, the cross section would only be sensitive to the neutron polarisabilities at $\mathcal{O}(\omega^4)$ in the LEX as the $\mathcal{O}(\omega^2)$ term vanishes for the electrically neutral neutron. Given the problems with extracting the neutron polarisabilities from Compton scattering off a free neutron, various alternate experimental approaches have been employed for the determination of the neutron polarisabilities.

The most popular method involves Compton scattering off deuterium. Deuterium is the simplest many-nucleon system, and contains one proton and one neutron. Because of the small uncertainties in the proton polarisabilities, the goal of deuterium Compton scattering experiments is to measure the deuterium Compton scattering cross section and thereby determine the deuterium polarisabilities. The neutron polarisability may then be extracted by subtracting the proton values from the deuterium values. To date, only a few experiments have been successful in extracting the deuterium Compton scattering cross section, one of which [14] was performed at MAX-lab in Lund in the 1990s [15]. This is reflected in the relatively high uncertainty in the current values for the neutron polarisabilities [13]

$$\alpha_n = 11.1 \pm 1.8_{\text{stat}} \pm 0.4_{\text{BSR}} \pm 0.8_{\text{th}}$$
$$\beta_n = 4.1 \mp 1.8_{\text{stat}} \pm 0.4_{\text{BSR}} \pm 0.8_{\text{th}}.$$

[2]It is worth noting that while Eq. 1.5 only contains terms up to $\mathcal{O}(\omega^2)$, higher-order terms become non-negligible when the photon energy increases even further. For example, the $\mathcal{O}(\omega^4)$ term contains a non-linear dependence on α_N and β_N, as shown in Ref. [11].

The fact that the statistical uncertainties in the neutron polarisabilities are as high as 44% has prompted further experiments in the field. These experiments have been performed at MAX-lab, and are currently being analysed.

1.3.2 Bound-nucleon polarisabilities

In addition to determining the nucleon polarisabilities, it is also of interest to see whether they are changed when the nucleons are bound inside a nucleus. Various experiments involving Compton scattering off light nuclei have been performed and are summarised in Table 1.3. The purpose of these experiments has been to look for changes in the bound-nucleon polarisabilities relative to the values for the free nucleon.

Nucleus	Reference
^{2}H	[14, 16, 17]
^{4}He	[18, 19, 20]
^{6}Li	[21]
^{12}C	[22, 23, 24, 25, 26]
^{16}O	[20, 21, 24, 25, 27, 28]
^{40}Ca	[20, 22]

Table 1.3: Previous measurements of Compton scattering off light nuclei.

When describing a nucleus consisting of many nucleons, one may introduce the nucleon-averaged polarisabilities α_N and β_N, where N is either the proton or the neutron. These are the multi-nucleon equivalents of the free-nucleon polarisabilities presented in Sec. 1.3.1. Introducing nuclear-modification parameters $\Delta\alpha$ and $\Delta\beta$ [26] which describe how the free-nucleon polarisabilities are altered inside the nucleus allows for the effective bound-nucleon polarisabilities to be written as

$$\alpha_{\text{eff}} = \alpha_N + \Delta\alpha, \qquad \beta_{\text{eff}} = \beta_N + \Delta\beta. \tag{1.7}$$

In the limit of no binding effects, $\Delta\alpha = \Delta\beta = 0$, and the bound-nucleon polarisabilities are the same as the free-nucleon polarisabilities. If binding effects exist, then $\Delta\alpha \neq 0$ and $\Delta\beta \neq 0$. In this case, the bound-nucleon polarisabilities are not the same as the free-nucleon polarisabilities.

The non-deuterium data presented in Table 1.3 have[3] been analysed with a phenomenological model first used in Ref. [22]. This model describes how sensitive the nuclear Compton scattering cross section is to the bound-nucleon polarisabilities α_{eff} and β_{eff} by utilising the total photoabsorption cross section and its expansion into electromagnetic multipoles for the relevant nucleus. Recent theoretical development [29] may lead to the possibility of extracting the bound-nucleon polarisabilities from targets heavier than deuterium.

[3]The deuterium data have been analysed within the framework of χEFT [13].

1.3.3 ^{12}C Compton scattering

While deuterium Compton scattering has been the primary experimental effort at MAX-lab over the past few years, ^{12}C Compton scattering experiments have been conducted for the purpose of cross-checking the normalisation of the deuterium data. These complimentary experiments are thus of major importance for the success of the deuterium program. This is because they confirm the normalisation[4] procedure used in the data analysis. The same analysis methods are used in both the deuterium and ^{12}C experiments, and by comparing the results of the ^{12}C analysis to published results, the validity of the experimental normalisation method may be determined. These experiments are also interesting on their own. This is because they provide information on changes to the nucleon polarisabilities when the nucleons are bound inside a nucleus. This investigation is possible through the comparison of results with phenomenological models.

As seen in Table 1.3, a number of ^{12}C Compton scattering experiments have been performed. Therefore, results from a new ^{12}C Compton scattering experiment can directly and reliably be compared with existing data. ^{12}C has a clear advantage over ^{2}H as a target in that the scattering cross section is much larger. Since the energy of the incident photon is below 100 MeV, the scattering process is coherent. This means that the total scattering amplitude $R(E,\theta)$ for a nucleus containing Z protons is given by a simple sum over the individual protons [13]. Thus

$$R(E,\theta) \sim \sum_{Z} \frac{e^2}{M_p} \sim \frac{Ze^2}{M_p}, \tag{1.8}$$

where e is the elementary charge and M_p is the proton mass. The fact that the scattering amplitude is proportional to Z means that the differential cross section for scattering is proportional to Z^2, as

$$\frac{d\sigma}{d\Omega} = |R(E,\theta)|^2 \sim \left|\frac{Ze^2}{M_p}\right|^2 \propto Z^2. \tag{1.9}$$

This relation implies that the differential cross section is ∼36 times larger for ^{12}C which contains six protons than for deuterium which contains only one proton. This means that data with high statistical precision may be obtained in a much shorter time for the ^{12}C case[5]. Figure 1.3 shows two examples of the Z^2 evaluation of the differential cross section obtained at a fixed energy an angle for a number of light nuclei.

1.4 Goal

The purpose of this experiment was twofold: to verify the procedure for normalisation of Compton scattering data by investigating ^{12}C and comparing to a well-established and com-

[4]The normalisation of the experimental data refers to the practice of correcting the measured yield for various experimental parameters such as detector efficiency, target thickness, and incident photon flux, such that the true absolute cross section is determined.

[5]In addition to the much larger cross section, a solid ^{12}C target is much easier to handle than a liquid deuterium target.

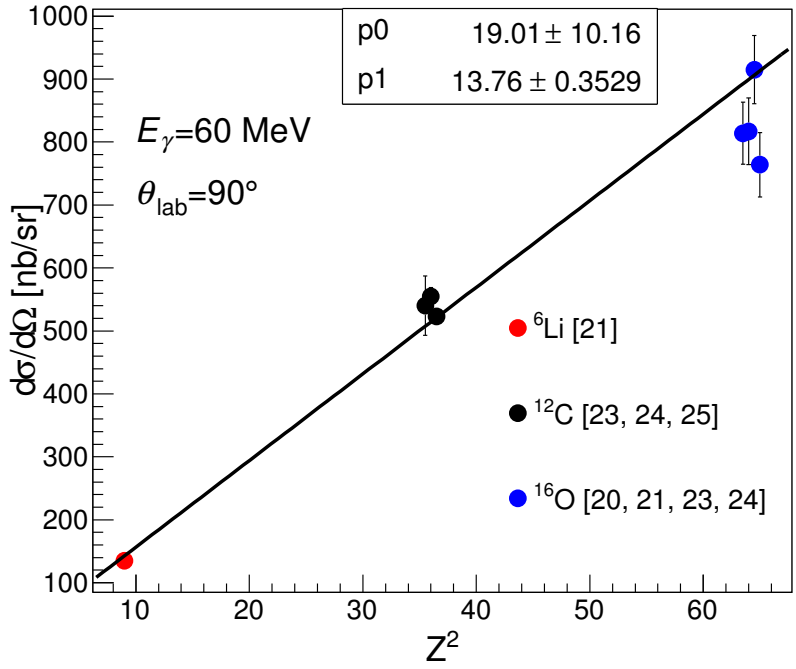

(a)

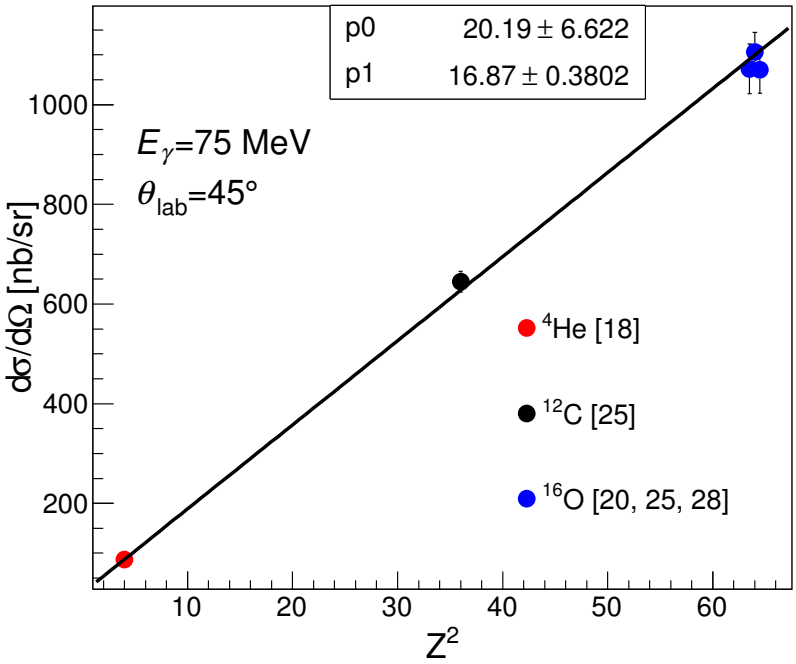

(b)

Figure 1.3: (Colour online) Previous measurements of the cross section for Compton scattering off various light nuclei at (a) $E_\gamma = 60$ MeV and $\theta_{\rm lab} = 90°$and (b) $E_\gamma = 75$ MeV and $\theta_{\rm lab} = 45°$. The good agreement between the data and the straight-line fit demonstrates that the cross section is proportional to Z^2, as predicted by Eq. 1.9. The fit parameters are shown.

prehensive existing body of data, and to determine whether the electric and magnetic polarisabilities of free nucleons are affected when they are bound inside a nucleus.

Chapter 2

Experimental Setup

2.1 Overview

The experiment forming the basis for this thesis was performed during a two-week run period at the MAX IV laboratory in Lund, Sweden. MAX IV[1] is the national electron accelerator facility in Sweden, and is mainly used for experiments involving synchrotron radiation. However, the laboratory also contains a Tagged-Photon Facility (TPF) [30] in which photonuclear experiments may be performed. The electrons used to produce the photons used in these photonuclear experiments come from MAX I, the electron storage ring which may also be used as a pulse-stretcher (PSR) ring (see Sec. 2.2). An overview of the facility is shown in Fig. 2.1.

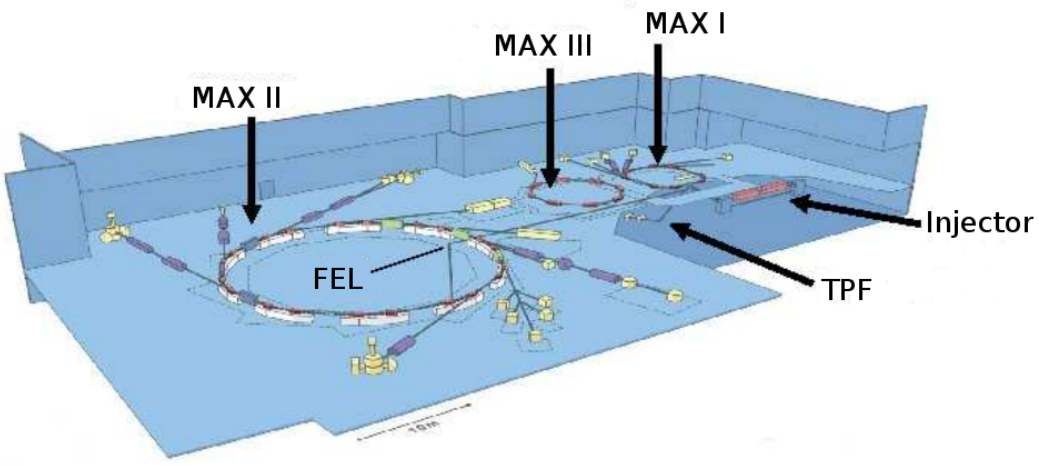

Figure 2.1: Overview of the MAX IV facility. Figure from Ref. [31].

[1]The existing MAX-lab was recently renamed the MAX IV Laboratory in anticipation of the move to the brand-new accelerator facility in 2016.

2.2 Electron-beam production

The electrons used for all research at MAX IV are produced in the injector. The injector [32] consists of a thermionic electron gun and two consecutive linear accelerators (LINACs). The electron gun is designed to produce electrons and accelerate them to kinetic energies of 2.3 MeV. These electrons are then fed into the two LINACs which can increase the kinetic energy of the electrons by ∼125 MeV per LINAC. After passing through the two LINACs, the electrons that are to be used for photonuclear research are directed into the MAX I pulse-stretcher ring [33]. These electrons have nominal kinetic energies of 250 MeV, and are injected in 200 ns pulses at 10 Hz [33].

The MAX I ring acts as a pulse stretcher, with the purpose of dramatically extending the width of the electron pulses and lowering the instantaneous current from the injector. The reason for this is that a pulsed electron beam is not experimentally ideal as short and intense electron pulses can lead to very large rate-dependent effects in the experiment detectors and associated electronics. Instead, a continuous wave (CW) electron beam, which results in a smooth data flow with fewer rate-dependent effects, is preferred.

The stored electrons in the pulse are slowly extracted from the PSR during the 100 ms subsequent to injection; that is, in the time period before the next pulse from the 10 Hz injector arrives. The procedure is repeated for the following pulses, creating a nearly CW electron beam which is then directed into the TPF. During the experiment presented in this thesis, the electron beam typically had a current of 15 nA, and a duty factor[2] of 45%.

As well as the features above, the electron beam had a significant time-dependent structure, as seen in Fig. 3.5. There were three reasons for this: [34]

- Uneven filling of the PSR due to the 200 ns pulse width from the injector and the 108 ns circumference of the PSR[3]. This gave rise to a 108 ns periodic time structure of varying intensity in the extracted electron beam.
- Time structures in the beam arising from the extraction shaker (the magnet which was used to extract the electron beam from the PSR). This microstructure had a period of 330 ns.
- The 500 MHz accelerating cavities in the accelerator gave rise to nanostructure with a period of 2 ns.

2.3 Photon-beam production

2.3.1 Bremsstrahlung

At the MAX IV TPF, the photons that are used in the experiment are produced by directing the electron beam with energy E_0 from the PSR onto a ∼100 μm thick aluminium radiator.

[2]The duty factor is essentially defined as the fraction of time the beam is on, which for a perfectly DC beam would be 100%.

[3]The PSR was originally built to complement a microtron. The microtron was subsequently replaced by LINACs. This resulted in the pulse-width/PSR circumference mismatch.

This results in bremsstrahlung, which arises when an electron is deflected by a nucleus in the radiator and a photon is emitted. This process will happen for a small fraction (about 0.1% [35]) of the electrons incident on the radiator, and results in decrease in the electron kinetic energy, so that a recoiling post-bremsstrahlung electron has a kinetic energy E'. Because of the conservation of energy, the energy of the bremsstrahlung photon E_γ is given by

$$E_\gamma = E_0 - E'. \tag{2.1}$$

The spectrum of bremsstrahlung photons from a thin radiator [36] is continuous in the range $0 \leq E_\gamma \leq E_0$. A typical bremsstrahlung-photon distribution measured in the experiment is shown in Fig. 2.2.

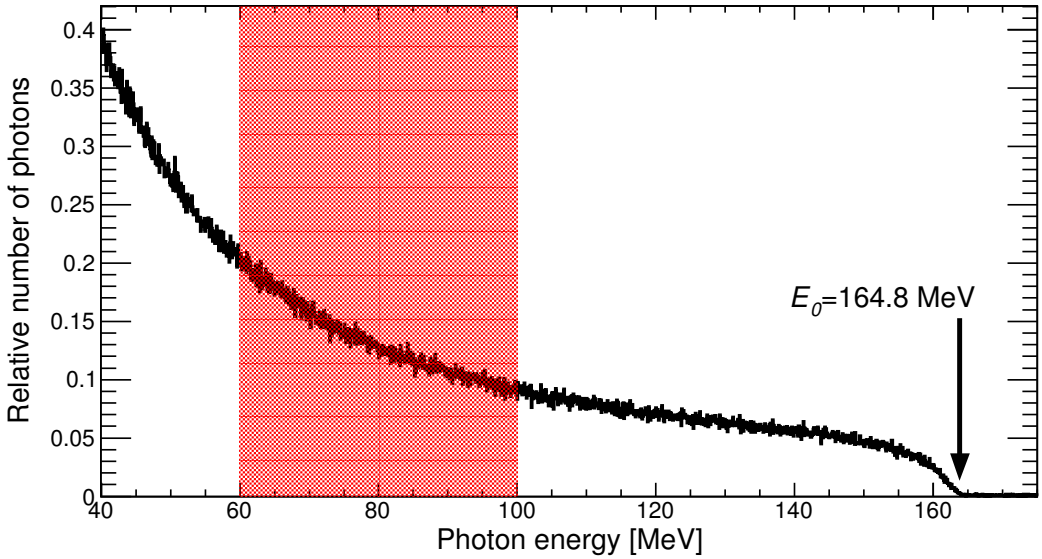

Figure 2.2: Distribution of bremsstrahlung photons. The maximum photon energy is equal to the electron beam energy, which for this experiment was 164.8 MeV. The red region shows the tagged photon energy range 60-100 MeV employed in this experiment, which was selected by positioning of the focal-plane (FP) hodoscope. See text for details.

2.3.2 Photon tagging

Knowledge of E_0 through the set up of the electron-accelerator system enables determination of the bremsstrahlung photon energy by measuring E'. This is done by using (essentially) a dipole magnet in combination with a segmented recoil electron detector (the FP hodoscope) placed at the focal plane of the "dipole". The system is referred to as a tagging spectrometer. Fig. 2.3 shows a layout of the experimental area. The radiator, tagger and hodoscope are all clearly shown.

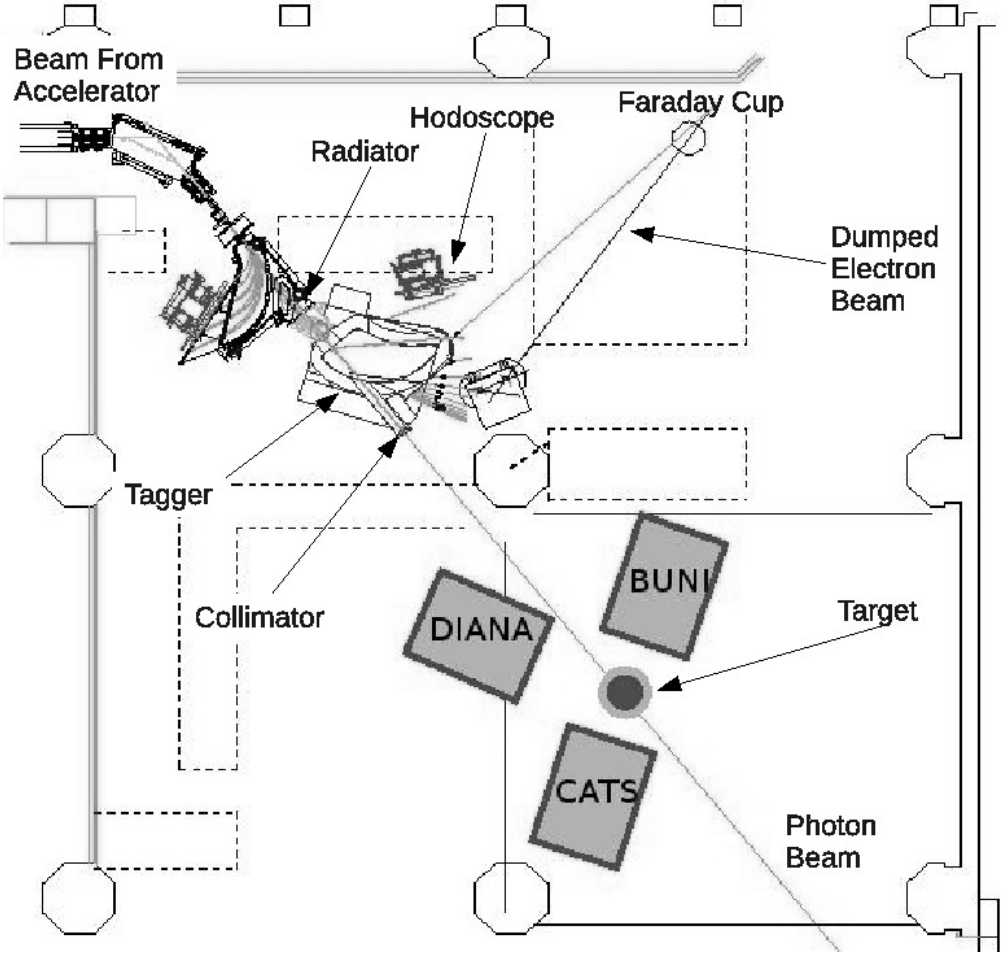

Figure 2.3: Layout of the experimental area, showing the tagging spectrometer, the FP hodoscope, the ^{12}C target, and the three photon detectors BUNI, CATS and DIANA.

Tagging spectrometer

Since the photon is electrically neutral while electrons are not, a magnetic field may be used to deflect the post-bremsstrahlung electron without disrupting the path of the photon. To accomplish this, the tagging spectrometer, which creates a magnetic field in the vertical direction in the lab perpendicular to the electron beam direction, is placed after the radiator. The Lorentz force $\vec{F}$ exerted on an electron with charge $-e$ and velocity v when it passes through a magnetic field with a magnetic flux density $\vec{B}$ is given by

$$\vec{F} = -e(\vec{v} \times \vec{B}). \tag{2.2}$$

The magnetic field thus deflects the post-bremsstrahlung electrons from their original path. Electrons that have not produced bremsstrahlung are also deflected from their original path and simply dumped.

The radius of the bend in the trajectory of the post-bremsstrahlung electrons caused by the magnetic field depends on the energy of the electron when it reaches the tagging spectrometer. A low-energy electron (which corresponds to a high-energy bremsstrahlung photon) will be deflected the most, while an electron that has passed through the radiator without interacting will be deflected the least.

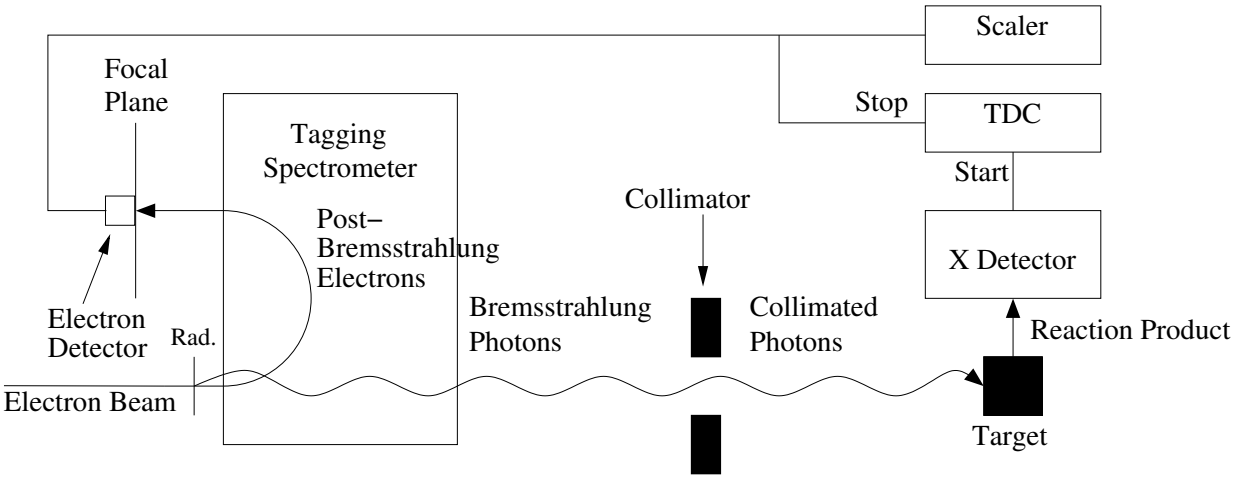

Figure 2.4: Overview of the photon-tagging process. Post-bremsstrahlung electrons are deflected in the tagging spectrometer through which the bremsstrahlung photons pass unaffected. A highly segmented hodoscope is placed at the focal plane of the spectrometer, such that the energy of the electrons may be determined. The beam of photons is collimated and directed towards the target. If an interaction between a photon and the target occurs, a reaction product (such as a scattered photon) may enter an X detector. A coincidence between an event in the X detector and a post-bremsstrahlung electron at the FP hodoscope is a candidate tagged event. Figure from Ref. [37].

FP hodoscope

For the experiment presented in this thesis, the photon energy range 60-100 MeV was of interest. Given the beam energy of 164.8 MeV, this corresponded to a post-bremsstrahlung electron energy range 104-65 MeV (see App. A). A plastic-scintillator hodoscope [30] placed at the FP of the tagging spectrometer enabled detection of these electrons. The location of the hodoscope together with precise knowledge of the magnetic field of the tagging spectrometer facilitated a momentum analysis which in turn enabled the determination of the energies of the corresponding photons, all on an event-by-event basis.

The hodoscope scintillators were arranged in two rows. There were 31 scintillators in the front row and 32 scintillators in the back row. Each scintillator had a width of 25 mm and a thickness of 3 mm. The two rows could be shifted with respect to each other, allowing for different degrees of overlap. In the experiment presented in this thesis, the overlap was 50% to allow for greater tagged-photon resolution. Each of the scintillators in the FP hodoscope was attached to a photomultiplier tube (PMT), which produced an analog output signal when an electron was detected the corresponding scintillator. Since an electron passed through both rows of the hodoscope, a coincidence between the front row and the back row could be established. In a 50% overlap situation, 62 possible coincidences, and thus 62 "FP channels" were defined geometrically, as shown in Fig. 2.5. By requiring a coincidence between the two rows, the background signal is greatly reduced.

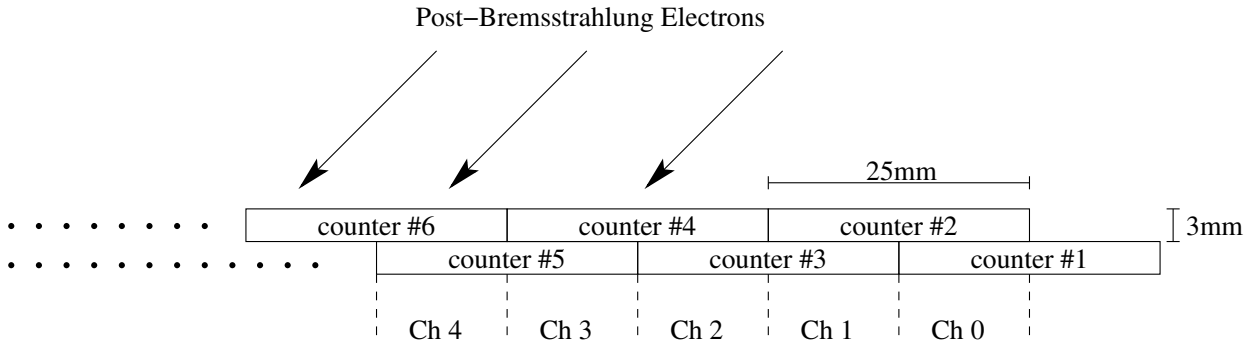

Figure 2.5: The FP hodoscope as set up during the experiment with a 50% overlap between the two plastic-scintillator rows. A post-bremsstrahlung electron within the momentum acceptance of the tagging spectrometer passed through both rows of the FP hodoscope, creating a coincidence signal. These coincidences defined the FP channels. Figure from Ref. [37].

2.3.3 Photon beam

The photon-tagging process described above allowed for the creation of a quasi-monoenergetic photon beam, since each FP channel corresponded to a narrow photon-energy band. The bremsstrahlung photons were emitted from the radiator in a cone centred about the direction of the incident electron beam with an opening angle θ, which depended on the Lorentz factor

γ. γ in turn depends on the electron beam energy E_0, the electron mass m_e and the speed of light c [35]. The opening angle was

$$\theta \approx \frac{1}{\gamma} \approx \frac{1}{\frac{E_0}{m_e c^2}} \approx 3.1 \text{ mrad}. \tag{2.3}$$

The photon beam was collimated using a 19 mm diameter tungsten-alloy primary collimator followed by a permanent sweeping magnet and a secondary collimator. This combination prevented any charged particles produced in the primary collimator from reaching the target. The setup of the collimators was such that at the location of the target, the cross-sectional area of the photon beam was smaller than the cross-sectional area of the target, so that all beam photons struck the target. The photon-beam diameter at the target was approximately 60 mm.

2.3.4 Tagging efficiency

Due to the collimation of the photon beam, not every bremsstrahlung photon produced in the radiator could strike the target. Some of the electrons detected by the FP hodoscope corresponded to photons which were collimated. The tagging efficiency ϵ_{tag} for a specific FP channel i is defined as the ratio of the number of tagged photons N_γ reaching the target to the number of post-bremsstrahlung electrons N_e detected by FP channel i

$$\epsilon_{\text{tag}}|_i = \left.\frac{N_\gamma}{N_e}\right|_i. \tag{2.4}$$

This is a purely geometric effect. Note that other non-geometric effects[4] also contributed to the tagging efficiency.

2.4 Carbon target

The ^{12}C target used was a 5.22 cm thick reactor grade graphite block with a density measured to be (1.83 ± 0.02) g/cm^3. The areal density of target nuclei κ is the number of nuclei per cm^2 in the target. Knowledge of the target thickness t, the target density ρ, Avogadro's number N_A and the mass per target nucleus A enabled the calculation of κ using

$$\kappa = \frac{\rho\, t\, N_A}{A}. \tag{2.5}$$

The areal density of target nuclei was $(4.80 \pm 0.07) \cdot 10^{23}$ cm^{-2} [39].

As this is a relatively thick target, a portion of the incident photon beam was attenuated via atomic processes (predominantly pair production). Attenuated photons were not considered in the overall normalisation of the experimental yield (see Chapter 4). Precision material-attenuation coefficients may be found in Ref. [40]. For this work, the NIST XCOM online tool [41] was used to determine the attenuation factor α for the ^{12}C target to be about 7% (see Sec. 4).

[4]Other effects included Coulomb multiple scattering in the radiator, the production of Møller electrons in the radiator and room-associated background in the FP hodoscope [38].

2.5 Photon detectors

Scattered photons were detected in three very large segmented NaI(Tl) crystal-scintillator detectors: BUNI, CATS, and DIANA. These three photon detectors are on loan from Boston University, Johannes-Gutenberg Universität Mainz and the University of Kentucky, respectively. For calibration purposes as well as tagging-efficiency measurements, a Pb-glass photon detector was used.

2.5.1 NaI(Tl) photon detectors

The three NaI(Tl) photon detectors each consist of a single large NaI(Tl) core crystal surrounded by a number of annular NaI(Tl) segments. The sizes of the different crystal segments differ between the three detectors. A common factor is that they are all very large, allowing for an energy resolution of about 2% at photon energies around 100 MeV (see below). This level of resolution is crucial to deuterium Compton scattering experiments, since the breakup of the deuterium nucleus requires just 2.2 MeV. The first excited state of ^{12}C is located at 4.44 MeV. Thus, the resolution of the photon detectors is such that the ^{12}C elastic-scattering peak may easily be studied.

When a highly energetic photon enters the NaI(Tl) crystal, it will produce an electron/positron pair. Both the electron and the positron will produce bremsstrahlung photons, which cause further electron/positron pairs. This process is known as an electromagnetic (EM) shower [42]. A scattered photon will lose all of its energy to such processes in the crystal. Because of the scintillating properties of the crystal used, the radiation from the EM shower is converted to visible light. The scintillation light is detected by photomultiplier tubes (PMTs) mounted on the detector. Together, the PMTs output a signal which is proportional to the energy deposited in the detector by the scattered photon (see Ref. [43]). The fact that the NaI(Tl) crystals used in the experiment are very large minimises the leakage of the EM shower associated with the scattered photon, allowing for the very good energy resolution discussed above.

The photon detectors are also sensitive to other particles, such as cosmic rays. In order for events corresponding to cosmic rays to be identified in the data set, each detector has a cosmic-ray veto. A highly energetic cosmic ray will simply pass straight through a detector. By requiring a coincidence between cosmic-ray detectors placed on either side of the core NaI(Tl) crystal, cosmic ray events may be identified.

BUNI

BUNI (Boston University Sodium Iodide) [44] consists of a cylindrical core crystal of diameter 26.7 cm and length 55.9 cm. Surrounding the core in the form of an annulus are four crystal quadrants of thickness 11.4 cm. These quadrants absorb any part of the EM shower that leaks out of the NaI(Tl) core. Further, a 12.7 cm thick layer of plastic scintillator divided into six annular segments is placed around the NaI(Tl) volume. The plastic-scintillator layer acts as a cosmic-ray veto. In total, 31 PMTs are attached to BUNI: 7 to the core, 3 to each NaI(Tl) quadrant, and 2 to each plastic segment.

CATS

CATS (Compton And Two photon Spectrometer) [45] is constructed in a fashion similar to BUNI. It consists of a cylindrical core crystal of diameter 26.7 cm and length 63.5 cm. Surrounding the core are six crystal segments of thickness 10.8 cm. These segments absorb any part of the EM shower that leaks out of the core. Around the NaI(Tl) volume, as well as on the back of the detector, a 10 cm thick layer of plastic scintillator is placed. The scintillator annulus has five segments. The plastic-scintillator layer acts as a veto against both cosmic rays and charged particles. A total of 50 PMTs are attached to the detector: 7 to the core, 4 to each NaI(Tl) segment, 3 to each plastic segment, and 4 to the plastic-scintillator veto at the back of the detector.

DIANA

DIANA (Detector of Iodine And Sodium) [39] consists of a huge cylindrical NaI(Tl) crystal of diameter 48 cm and length 51 cm. Surrounding the core is a 4 cm thick annular layer of crystal, which is divided both axially at its midpoint and into six annular segments. The outer layer of crystal is used both as a cosmic-ray veto and to absorb any part of the EM shower leaking out of the core. Also, a 6 mm thick layer of plastic scintillator acts as a cosmic-ray veto. 19 PMTs are attached to the core and 36 PMTs are attached to the annulus. The 19 core PMTs and half of the annulus PMTs are attached to the rear of the detector, while the other half of the annulus PMTs are attached to the front of the detector.

2.5.2 Pb-glass photon detector

The lead-glass (Pb-glass) photon detector utilises the Čerenkov effect for photon detection. Pb-glass has a very high refractive index. When a photon enters the detector, it gives rise to an EM shower. The speed of the particles in the shower may exceed the speed of light in Pb-glass, and thus Čerenkov light [46] is produced. The intensity of this light is proportional to the incident-photon energy. A single PMT is attached to the back of the detector. The Pb-glass detector was used solely for low-intensity tagging efficiency measurements and not to detect scattered photons.

2.6 Data Acquisition

In the experiment, the coincidence technique is employed to identify scattered photons. Coincidences between the FP hodoscope and the NaI(Tl) photon detectors are candidate tagged-photon events. Of particular interest is the time difference between an electron striking the FP hodoscope and a scattered photon entering a photon detector. This time difference is the same for all true coincidences; that is, events where the photon and the electron come from the same bremsstrahlung process. This is because all electrons are highly relativistic and have velocities very close to the speed of light. Also of interest is the energy deposited by a scattered photon in a photon detector. This energy can be compared to the photon energy predicted by the tagging process.

To determine these quantities, three main types of electronics are used in the data acquisition (DAQ): Time-to-digital converters (TDCs) (which determine the time difference between a scattered-photon start and a post-bremsstrahlung electron stop signal), analog-to-digital converters (ADCs) (which are used to determine the energy deposited by the scattered photons) and scalers (which count the number of electrons that strike each FP channel). Two types of TDCs were used in parallel during the experiment: single-hit TDCs and multi-hit TDCs. The single-hit TDC module used was the CAEN V775, which accepts a single start signal and a single stop signal for each trigger. The multi-hit TDC module used was the CAEN V1190B, which accepts a single start signal and up to four stop signals for each trigger. The advantage of using multi-hit TDCs is that the risk of an accidental electron stopping the TDCs before the true electron does so is lowered substantially, see Sec. 3.6.

Scattered photons triggered the system. An overview of the electronics is shown in Fig. 2.4. For a complete discussion, see Ref. [43].

2.6.1 Run types

The run types during the experiment may be divided into four categories: calibration runs, tagging-efficiency runs, cosmic-ray runs and scattering runs.

Calibration runs

Because of the many different detector components involved in the experiment (62 independent FP channels and the large number of PMTs attached to each of the NaI(Tl) detectors), the photon detectors had to be carefully calibrated in terms of both time and energy. To calibrate one of the NaI(Tl) detectors, it was placed directly into the collimated photon beam. The beam intensity was reduced to 10-100 Hz. This low intensity was necessary to avoid stressing the NaI(Tl) crystals or the DAQ system. Calibration runs for the different detectors were performed at the beginning of the experimental run period.

Tagging-efficiency runs

The tagging efficiency was determined once per day during the experiment. It was measured by placing the Pb-glass detector directly into the photon beam. As for the calibration runs, the beam intensity was reduced to 10-100 Hz. By counting the number of photons entering this 100%-efficient photon detector as well as the number of electrons striking each of the 100%-efficient FP channels, the tagging efficiency was determined.

Cosmic-ray runs

As discussed in Sec. 2.5.1, the three NaI(Tl) photon detectors are all instrumented for the detection of cosmic rays passing through them. However, the veto detectors that serve this purpose are only $\sim$97% efficient. If a cosmic event is not eliminated when "straight-through" veto cuts are placed on the data, it will contribute to the background. Dedicated cosmic runs are performed in order to account for this background. In these runs, the electron beam

is shut off. One cosmic-ray run was performed directly after each of the calibration runs for each of the NaI(Tl) detectors. In addition, a number of cosmic-ray runs with the detectors in their scattering configurations, shown in Fig. 2.6, were performed. This procedure allows for measurement of the cosmic-ray background, which may then be subtracted from the real scattering data.

Scattering runs

The runs in which the $^{12}C(\gamma,\gamma)^{12}C$ reaction was studied are referred to as scattering runs. In these runs, the graphite target described in Sec. 2.4 was placed directly into the collimated photon beam and the average intensity of the beam was increased to 1-4 MHz. The three NaI(Tl) photon detectors were placed at laboratory angles of 60°(CATS), 120°(BUNI) and 150°(DIANA) as shown in Fig. 2.6.

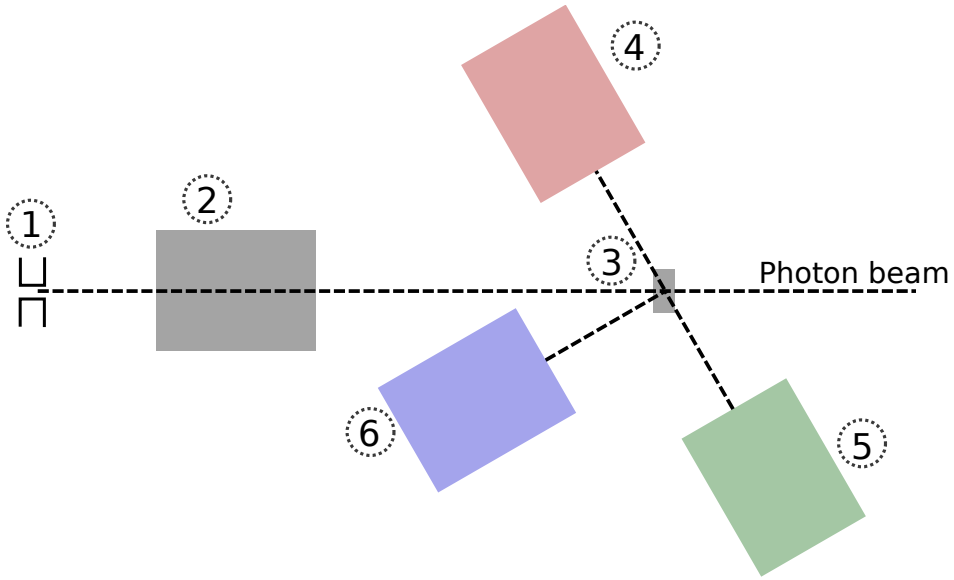

Figure 2.6: Overview of the photon-detector setup. The photon beam was collimated at (1), after which two distinct types of detector configurations were used. When performing calibration and tagging-efficiency runs, the photon detector was placed directly into the photon beam, as in (2). When performing production runs, the ^{12}C target was placed into the beam at location (3), and the three NaI(Tl) photon detectors BUNI (4), CATS (5) and DIANA (6) were placed at laboratory angles of 60°, 120° and 150° relative to the photon beam. Cosmic-ray runs were performed for both detector configurations, as explained in the text.

Table 2.1 presents an overview of how the beam time provided during the experiment was employed. The major part of the experimental time was dedicated to $^{6}Li(\gamma,\gamma)^{6}Li$ scattering runs, as this was the primary focus of the run period. These data are not part of the analysis presented here.

Run type	Hours
Calibration	3.2
Tagging efficiency	6.2
Cosmic	33.9
$^{12}C(\gamma,\gamma)^{12}C$ scattering	45.8
$^{6}Li(\gamma,\gamma)^{6}Li$ scattering	131.4

Table 2.1: A summary of the experiment.

Chapter 3

Data analysis

3.1 Overview

In Chapter 1, the connection between nuclear Compton scattering and the nucleon polarisabilities was outlined. The connection between the nuclear Compton scattering cross section and the data acquired with the experimental setup described in Chapter 2 is the data analysis presented in this chapter. The experimental differential cross section may be written

$$\frac{d\sigma}{d\Omega} = \frac{f_{\text{rate}}}{f_{\text{geometrical}}} \frac{N_{\gamma,\text{scattered}}}{N_{\gamma,\text{incident}}\,\kappa\,\Omega}. \tag{3.1}$$

The differential cross section requires the normalisation of the number of scattered photons $N_{\gamma,\text{scattered}}$ (the reaction yield), the number of photons incident on the target $N_{\gamma,\text{incident}}$, the number of target nuclei per unit area κ, and the solid angle Ω. In addition, two corrections are required: $f_{\text{geometrical}}$ is related to geometrical effects such as an extended target and an extended photon beam, and f_{rate} is related to effects that depend on the electron rate in the FP hodoscope. A thorough understanding of these correction factors is crucial for correct normalisation of the experimental data.

The analysis procedure is shown in Fig. 3.1, where the steps leading to the parameters required by Eq. 3.1 are outlined. In all steps of the data analysis, the analysis framework ROOT [47, 48] has been used.

3.2 Detector calibration

The first step of the analysis procedure was to calibrate the NaI(Tl) photon detectors both for time and for energy. The calibration was performed using the data collected during the in-beam calibration runs described in Sec. 2.6.1. Before performing the calibration, all events corresponding to cosmic rays passing through the photon detector in question were filtered. This was done by excluding those events where there was a coincidence between two opposite veto paddles. After this, two sets of data files were obtained: the cosmic-filtered files and the event-filtered files. The event-filtered files were free from straight-through cosmic-ray events, while the cosmic-filtered files contained only such events.

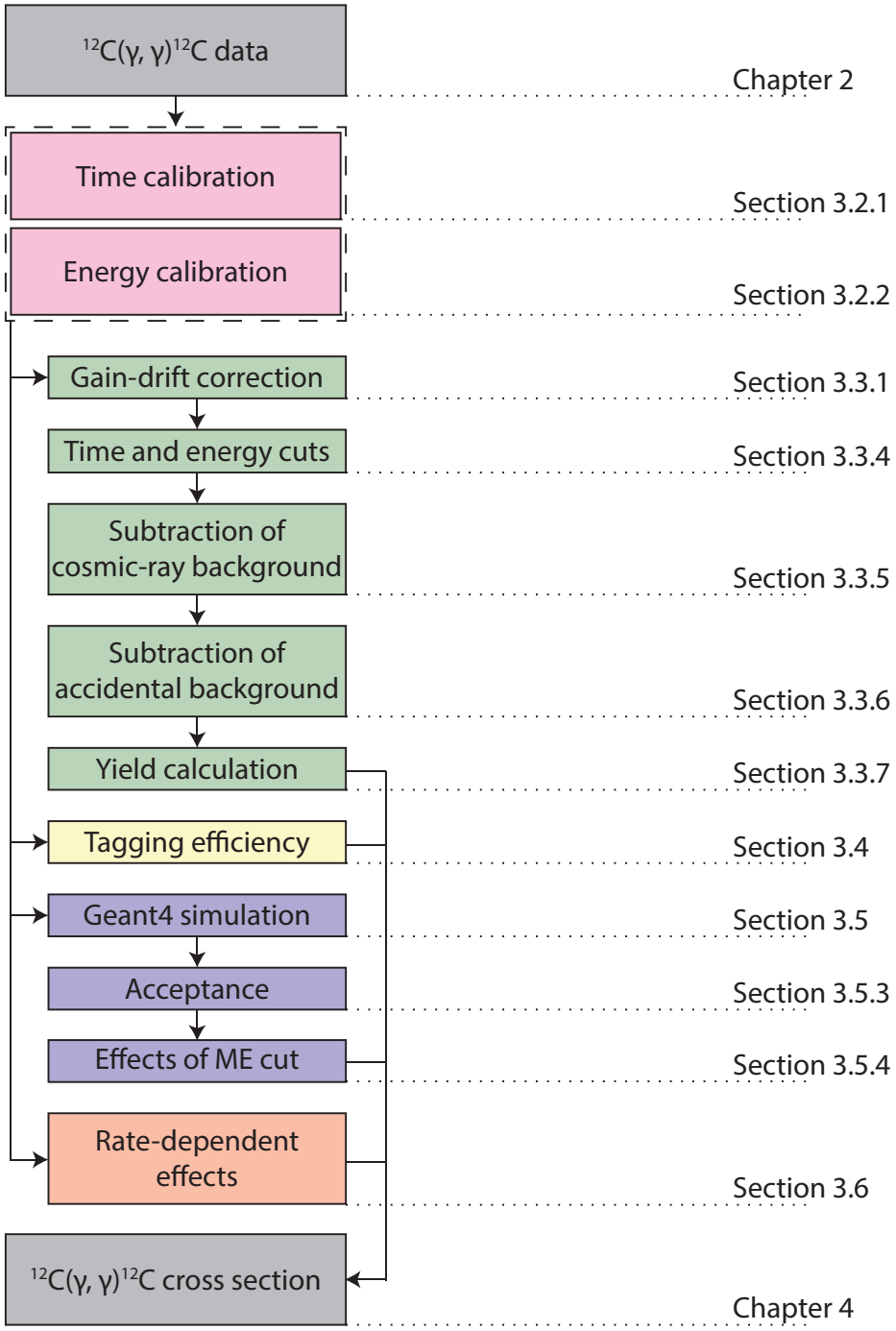

Figure 3.1: Overview of the analysis procedure.

Time calibration was needed because the lengths of the cables attached to the different FP hodoscope scintillators were all slightly different, causing a slight difference in the delays of the signals from the FP hodoscope and thus slightly different true-coincidence peak locations. Since the sharpest possible true-coincidence peak[1] (the prompt peak) was desirable, these signal delays had to be determined and corrected to optimise identification of true coincidences in the scattering data. The energy calibration was needed because the high voltages applied to the PMTs were only crudely set to match the gains. In order to compare and combine spectra obtained with the different PMTs, these gains needed first to be precisely matched.

3.2.1 Time calibration

The time calibration was performed as described in Ref. [43]. Since both single-hit and multi-hit TDCs were used simultaneously, each had to be analysed separately. For any one of the two TDC types, there were a total of 62 TDC spectra available for analysis, one for each of the 62 FP channels. As discussed in Sec. 2.6, the TDCs registered the time difference between a start and a stop signal. This time difference is referred to as the Time-of-Flight. During the calibration runs, the beam intensity was so low that there were almost no accidental events, leading to a very well-defined true-coincidence peak in each of the TDC spectra. By fitting Gaussian distributions to each of these peaks, the locations were determined, and any differences in the true-coincidence peak location between the different FP channel TDC spectra were corrected. The spectrum resulting from summing all of the individual FP channel TDC spectra before the TDC offset calibration consisted of a very broad distribution of peaks, as shown in Fig. 3.2a. After the calibration, all of the individual peaks were precisely offset in software to the same value, so that summing all 62 TDC spectra resulted in a single sharp peak, as shown in Fig. 3.2b. This true-coincidence peak Full Width at Half Maximum (FWHM) was $\sim$2 ns, consistent with expectations based upon the jitter in the FP TDC start and stop signals and previous analyses of data taken with the same detectors [39].

3.2.2 Energy calibration

The energy calibration was performed as described in Ref. [43], except for the fact that a quadratic term in the energy calibration of the ADCs used in the experiment[2] was allowed in the analysis. There is one energy spectrum for each PMT in the photon detectors for each of the 62 FP channels. The energy calibration of one photon detector included compensating for the different pedestal[3] locations of the different PMTs, matching the gains of the different PMTs so that the same photon energy corresponded to the same ADC channel for every

[1] True coincidences are events corresponding to a recoil-electron/bremsstrahlung-photon pair coming from the same bremsstrahlung process. The electron is detected in the FP while the photon is either detected directly (in-beam runs) or scattered and detected (scattering runs).

[2] The quadratic behaviour of the ADCs arose from non-linearities in both the detector gains and the responses of the ADCs.

[3] The pedestal is the energy-spectrum location of the events corresponding zero energy deposition in the detector.

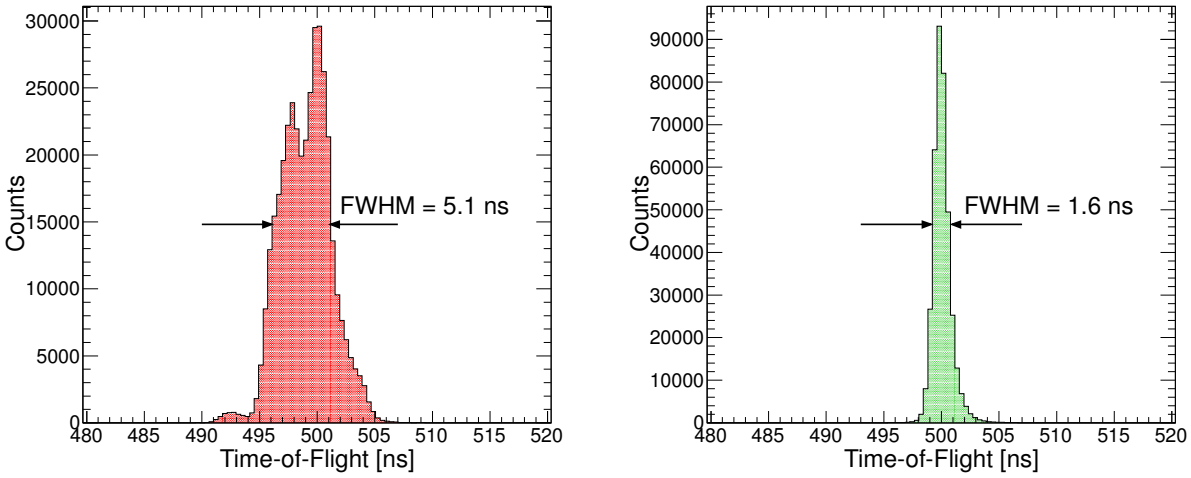

(a) (b)

Figure 3.2: Comparison between a single-hit TDC spectrum summed over all FP channels (a) before and (b) after time calibration. The calibration resulted in a sharp true-coincidence peak with a FWHM of 1.6 ns, offset to 500 ns for clarity. Similar spectra were formed with the multi-hit TDC data.

PMT in the entire detector, and adding the energy deposited in the outer segments (the leakage from the core) of the detector back to the total-energy spectrum. An example of an energy spectrum summed over all FP channels for one detector before and after the above steps were performed is shown in Fig. 3.3a. Using the information from the setup of the FP hodoscope (the photon energy to which each FP channel corresponded), the ADCs were calibrated so that the units of the energy spectrum were converted from ADC channels to MeV, as shown in Fig. 3.3b. By applying this calibration to the data, the peak shown in Fig. 3.3c was obtained, which demonstrates that the energy resolution was better than 2 MeV. This was an improvement of 10% compared to the results presented in Ref. [43], and was due to the inclusion of the quadratic term in the ADC calibration discussed above.

3.3 Scattered-photon yield

An accurate determination of the scattered photon yield from the time- and energy-calibrated spectra required the cuts and corrections detailed in this section.

3.3.1 Gain-drift correction

It has previously been shown [49] that the gains of the photon-detector PMTs change over time due to factors such as varying external EM fields and temperature. This can lead to shifts in the ADC channel corresponding to a specific photon energy. Thus, the drift of the gains of all of the PMTs has to be carefully monitored and precisely corrected.

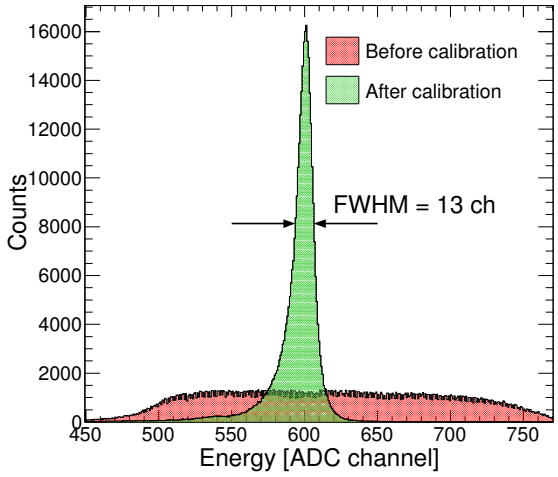

(a)

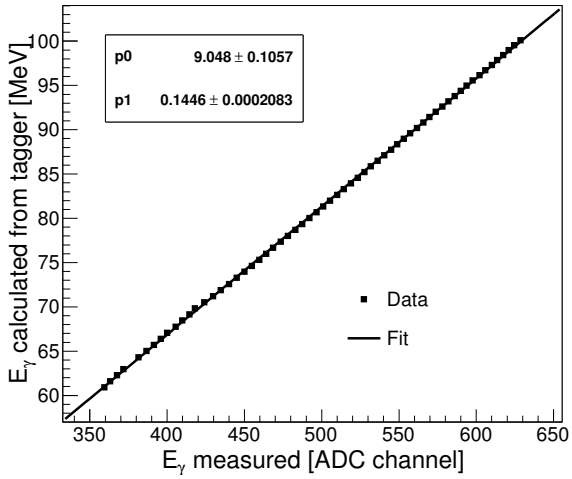

(b)

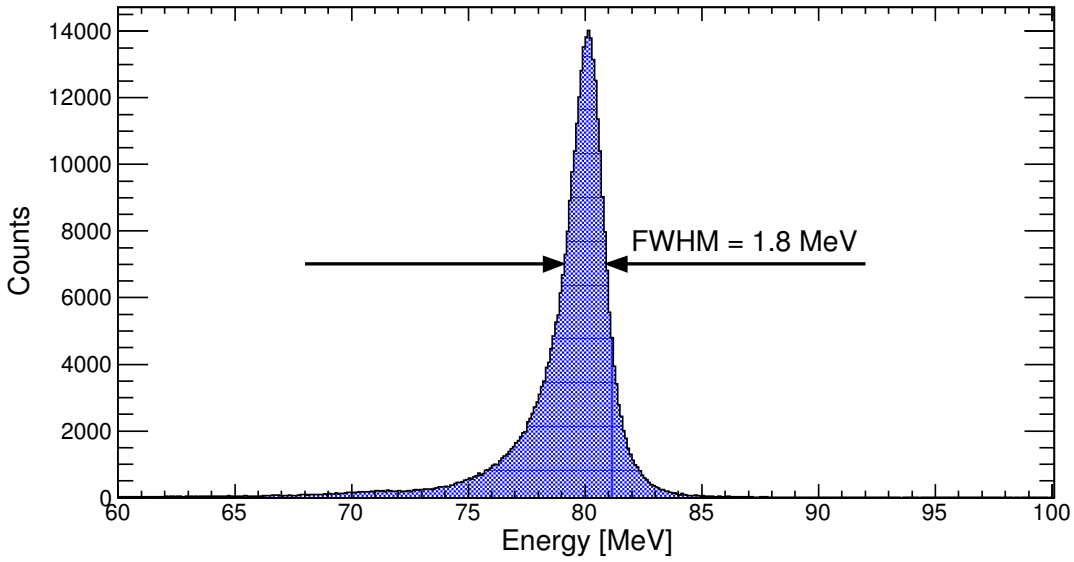

(c)

Figure 3.3: (Colour online) (a) Comparison between energy spectra from BUNI (summed over all 62 FP channels) before (red) and after (green) pedestal corrections, gain-matching and segment add-back. (b) The position of the FP hodoscope as well as the tagger setting allowed for the determination of the photon energy corresponding to each of the FP channels. By comparing this with the measured scattering-peak location in the calibrated photon-detector energy spectrum for each FP channel and fitting a first-degree polynomial, an absolute energy calibration was obtained. (c) Calibrated energy spectrum summed over all FP channels. The FWHM of 1.8 MeV is consistent with previous measurements at these energies [39].

The method developed in Ref. [39] was used to track the gain drift using cosmic-ray events. As explained in Sec. 3.2, the very large number of cosmic rays which pass through the detector were filtered from the scattering data, so that for each original data file, a cosmic-filtered file and an event-filtered file were produced. The cosmic rays are highly energetic (their energies lie far, far above the tagged-photon region) and formed a well-defined peak in the ADC spectrum for each of the detector PMTs in the cosmic-filtered data files.

It was determined that the shape of the peak due to straight-through cosmic rays could be parametrised by a modified Gaussian distribution[4] as described in detail in Ref. [39]. By fitting the modified Gaussian to the straight-through cosmic-ray peak for a specific PMT for a specific run, the location of the peak was determined. The fitting procedure was repeated for all photon-detector PMTs, as well as for all calibration and scattering runs during the run period. By comparing the location of the peak for a specific PMT for all scattering runs with the peak location for the same PMT during the calibration run, the drift of the PMT gain was determined. The drift of the gain of one PMT over 16 runs is shown in Fig. 3.4. This procedure was repeated for all PMTs in the photon detector.

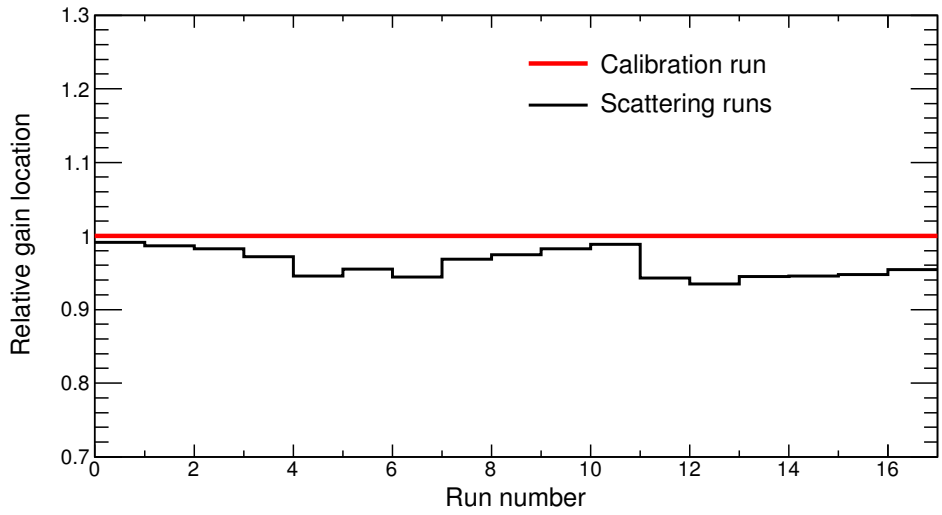

Figure 3.4: (Colour online) The gain drift of one PMT in BUNI. The red line indicates a gain relative to that measured during the calibration run; that is, a total absence of drift. The black line shows the drift of the gain during 16 scattering runs relative to the calibration gain. For the PMT shown, the gain drifted as much as 7% during the run period.

3.3.2 Scattering-mode time and energy spectra

When the drift in the PMTs had been corrected, the calibrations obtained by analysing the data from the in-beam calibration runs could be applied directly to the scattering data. When the detectors were moved into their scattering locations and the ^{12}C target was installed,

[4]Basically, a Gaussian distribution with a tail to lower energies to allow for straggling.

the electron-beam intensity was increased from 10-100 Hz to 1-4 MHz. This rate increase led to a large background consisting of events where the FP TDC started by a photon in the photon detector was stopped overwhelmingly by an electron not originating from the same bremsstrahlung process in the radiator, so-called accidental or random events. In the time spectra, the accidental events were distributed over the entire time interval covered by the TDCs. In the energy spectrum, they were distributed over the entire range of all possible photon energies. However, the detector calibrations described in Sec. 3.2 ensured that the location of the true-coincidence peak corresponding to scattered photons was well known both in time and in energy. The time calibration of the detectors ensured that the location of the true-coincidence peak was the same for all FP channels. This means that it was possible to directly sum TDC spectra for multiple FP channels. The same procedure was not possible for the photon-energy spectra. This was because the location of the scattered-photon peak in the photon-energy spectrum for a specific FP channel depended on the FP channel number, since the different FP channels corresponded to different tagged-photon energies and therefore different scattered-photon energies.

3.3.3 Missing energy

In order to sum photon-energy spectra corresponding to multiple FP channels, the concept of missing energy (ME) was introduced. It was based on the fact that the energy of a scattered photon was determined in two ways simultaneously: via the photon tagger and reaction kinematics and via the energy deposited in the precisely calibrated photon detector itself.

In practice, it was known from Eq. 1.3 how the energy of a photon corresponding to a given FP channel was shifted when it scattered elastically off a nucleus. The result was then compared to the energy deposition measured by the PMTs in the photon detector. Ideally, the difference between the two should be equal to zero, regardless of FP channel. In reality, the missing-energy peak was broadened in the same way as the energy peaks in Sec. 3.2.2 due to the resolution of the detectors. The difference between the deposited photon energy $E_\gamma|_{\mathrm{NaI}}$ and the anticipated photon energy $E_\gamma|_{\mathrm{FP}}$ from the tagging process was

$$\mathrm{ME} = E_\gamma|_{\mathrm{NaI}} - E_\gamma|_{\mathrm{FP}}.$$

If the missing energy was zero, the event was most likely a true coincidence. That said, there is also a background consisting of accidental events. Such events may also have a missing energy equal to zero. In order to produce ME spectra for each of the 62 FP channels, the ME of each event was calculated and histogrammed.

3.3.4 Time and energy cuts

The calibration procedure allowed for the summing of time spectra and ME spectra from multiple FP channels. An example TDC spectrum, summed over all FP channels, is shown in Fig. 3.5. Recall that the calibration procedure was configured so that the prompt time peak is expected at 500 ns (as seen in Fig. 3.2b). However, no peak is seen in the summed scattering-run TDC spectrum. The true-coincidence peak is simply overwhelmed by the background. It is clear from Fig. 3.5 that the majority of all events registered during the

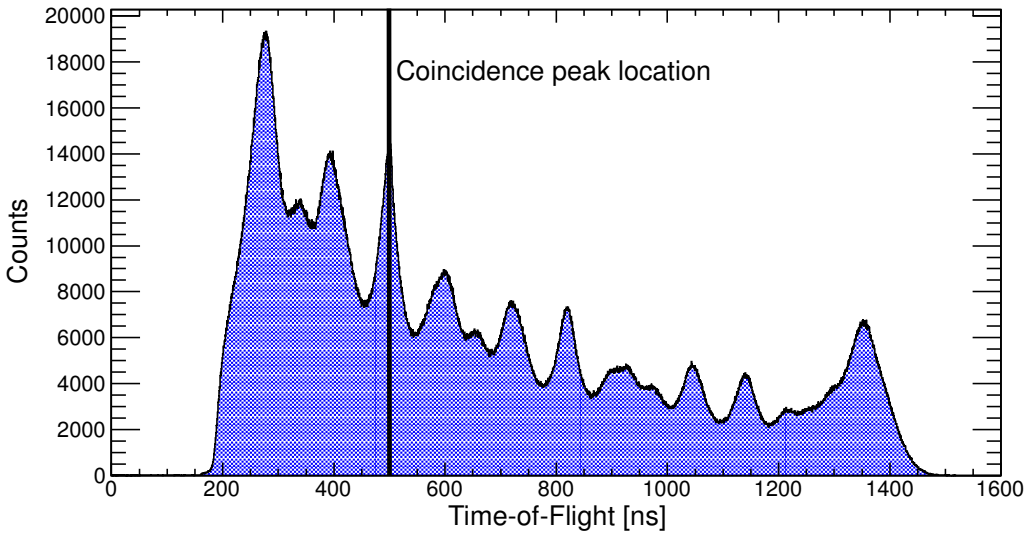

Figure 3.5: Scattering-run TDC spectrum summed over all FP channels. The coincidence timing peak is located at 500 ns. The large background prevents the prompt peak from being visible.

scattering runs were background events. In order to reduce this background, cuts were applied on both the ME and time spectra. These cuts were based on the facts that:

- The coincidence timing peak is located at 500 ns.
- The scattering energy peak in the ME spectra is located at 0 MeV.

Since an entry in the time spectrum corresponds to an entry in the ME spectrum and vice versa, an ME spectrum which is filled only with events in the time range $500 \pm \Delta T$ ns contains substantially less background than a full ME spectrum does. The same is true for the time spectrum, which may be filled only with events in the ME range $0 \pm \Delta E$ MeV.

The widths ΔT and ΔE of the time and ME cut windows are not arbitrary. If a cut window is too wide, too much background will be accepted and obscure the peak. If the window is too narrow, not all events that form the peak will be included. Since the yield is extracted from the ME spectrum (see below), the width of the time-cut window has to be chosen wisely. All scattering events must be contained within it without including unnecessarily large amounts of background events.

Optimisation of prompt time window

In order to optimise the width of the prompt-cut time window, a prompt ME window between -4.0 MeV and +2.5 MeV was defined[5]. A time spectrum containing the events having an

[5]The limits of the prompt ME window were defined so that any contribution from the inelastic scattering peak at -4.44 MeV was avoided, and so that the scattering events lying above 0 MeV due to the broadening of the scattering peak were included.

ME in this range was created. The result is shown in Fig. 3.6, where the coincidence peak is clearly visible at ∼500 ns. After the prompt ME cut had been optimised such that the

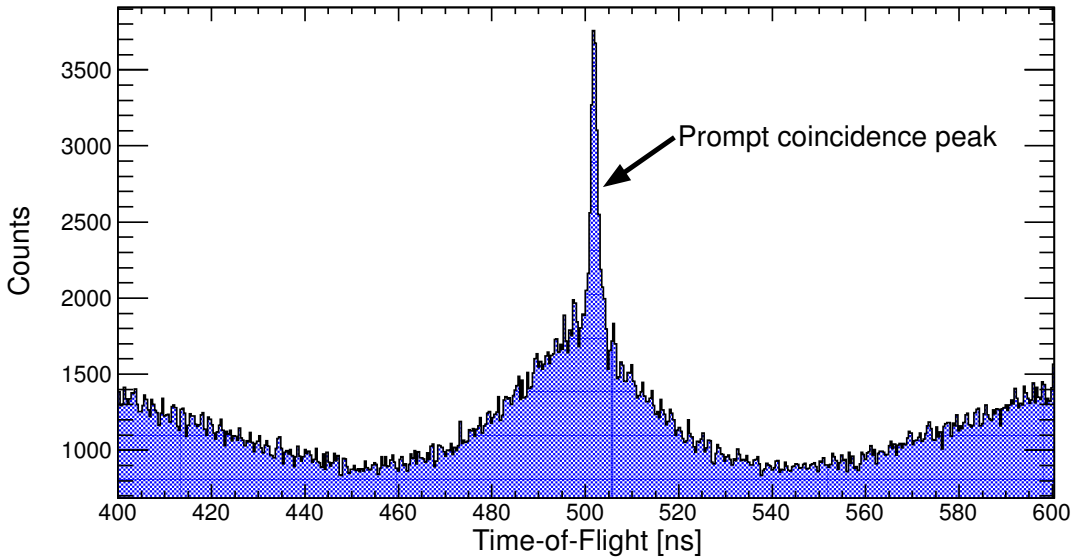

Figure 3.6: ME-cut scattering-run TDC spectrum summed over all FP channels. The coincidence peak is clearly visible at 500 ns. The ME cut from -4.0 MeV to +2.5 MeV was very effective at bringing the signal forward.

coincidence peak was as distinct from the background events as possible, the width of the prompt time window was optimised. This was done by noting that the background portion of the time spectrum seen in Fig. 3.6 may be approximated with a second-degree polynomial in the close vicinity of the prompt peak. The spectrum in this region was fitted with the sum of a Gaussian distribution and a second-degree polynomial, as seen in Fig. 3.7. The left side of the cut was set 4σ[6] to the left of the mean of the Gaussian. This point, marked in Fig. 3.7, agrees well with what is determined "by eye".

A relationship between the yield and the window width was obtained by subtracting the fitted background and integrating the bin contents to the right of the start of the prompt window. These results are shown in Fig. 3.8, together with the corresponding results from the integration of the calibration-run TDC peaks where the peak is clean and there is essentially no background. The prompt window width was determined by locating the point at which the integral was maximised, as all events in the prompt peak were then located within the prompt window. In the case shown in Fig. 3.8, a cut window width of 7 ns was determined.

[6] 4σ should miss only 0.006% of the events.

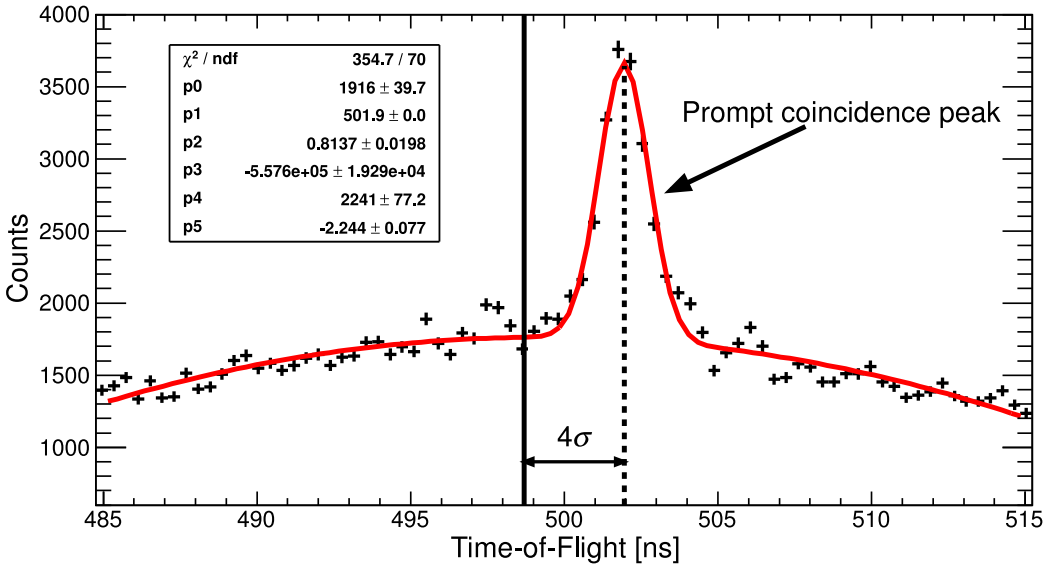

Figure 3.7: (Colour online) Example of fitting a Gaussian superimposed on a quadratic background (red line) to the coincidence timing peak (black points). The vertical solid line at 498.8 ns indicates the left side of the timing cut window, which was located 4σ to the left of the mean of the Gaussian.

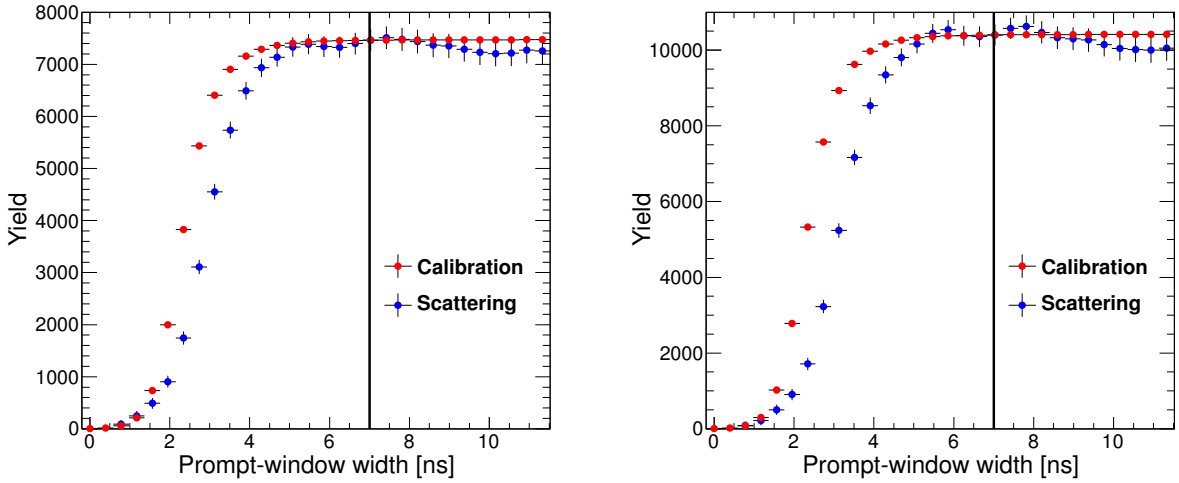

(a) (b)

Figure 3.8: (Colour online) Integrals of the (a) single-hit and (b) multi-hit TDC prompt peaks as a function of the prompt-window width. The left side of the timing cut window was located at 498.8 ns. The width of the window was varied. The vertical lines are located at 7 ns, the optimal prompt-window width determined with this analysis.

Prompt and accidental time cuts

The optimised prompt time cut defined in the previous section was applied to each of the FP channel time spectra, so that a set of 2×62 prompt ME spectra was obtained (62 single-hit and 62 multi-hit TDC prompt spectra). Because the prompt time window also contained background events represented by the polynomial fit in Fig. 3.7, an additional subtraction of background events was needed. The first step in this process was to generate ME spectra containing only accidental events for each FP channel. In order to construct such spectra, accidental-event time windows were defined such that events within the prompt-time window were excluded. It has been shown in Ref. [39] that as long as the accidental-event window is defined outside of the prompt window, its width may be chosen such that statistics are maximised; that is, the wider the better.

The procedure for defining the accidental time windows was slightly different for the single-hit and the multi-hit TDC spectra. Due to the presence of the large and important rate-dependent effects in the FP hodoscope data discussed in Sec. 3.6, the region to the left of the prompt-time peak in the single-hit TDC spectra contained both accidental events and true events[7]. This meant that a truly accidental ME spectrum had to sample events only to the right of the prompt peak. The multi-hit TDC spectra did not contain any stolen coincidences, and thus the accidental-event time window locations could be chosen freely, as long as the prompt window was excluded.

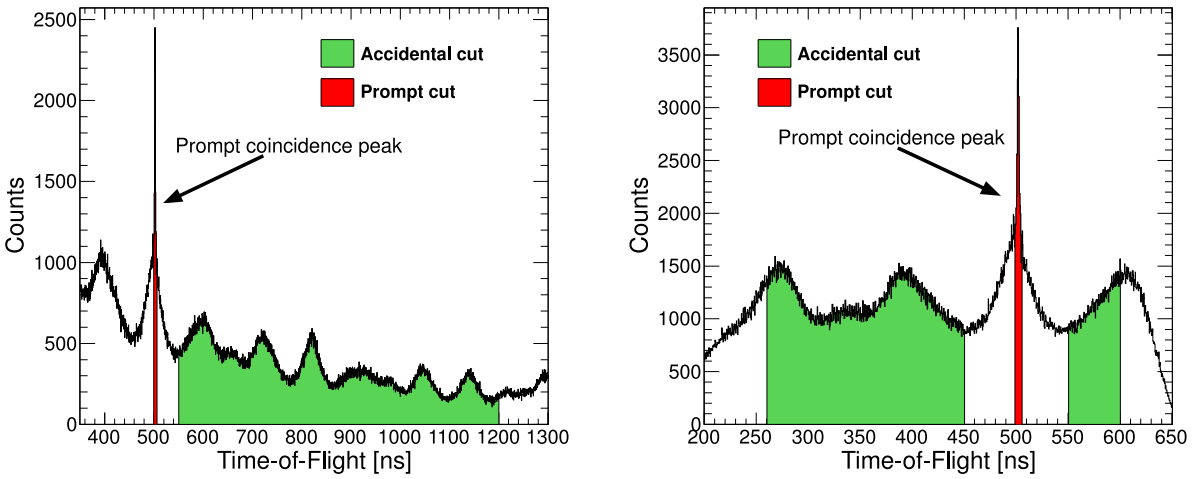

(a) (b)

Figure 3.9: (Colour online) The two timing cuts applied to the (a) single-hit and (b) multi-hit TDC spectra for the scattering-run data. The total widths of the single-hit and multi-hit TDC accidental-timing cuts are 650 ns and 240 ns, respectively.

By applying these accidental-event time cuts to the scattering data, 2×62 ME spectra

[7]The true events that are located to the left of the prompt time peak are known as stolen coincidences and correspond to the situation where the single-hit TDC was started by a scattered photon but stopped by an accidental electron.

containing only accidental events were generated. A comparison between the prompt and accidental ME spectra summed over the entire FP hodoscope is shown in Fig. 3.10.

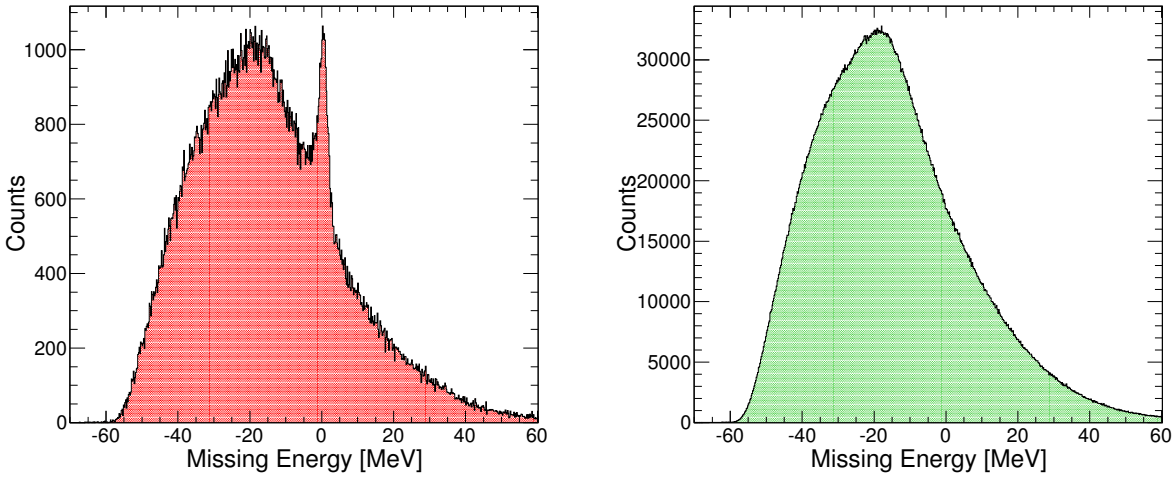

(a) (b)

Figure 3.10: The FP-summed ME spectra resulting from applying the (a) prompt and (b) accidental timing cuts to the single-hit TDC data. Note the vastly different scales on the two spectra. The number of events in the accidental spectrum is much larger due to the accidental cut being much wider than the prompt cut. The scattering peak is clearly visible at ME = 0 MeV in the prompt spectrum.

3.3.5 Subtraction of cosmic-ray background

Apart from accidental recoil-electron/scattered-photon coincidences, the background seen in Fig. 3.10 also consisted of cosmic-ray events. As discussed in Sec. 2.6.1, these remained due to the fact that the veto cuts were not 100% efficient. Thus, both the prompt and the accidental ME spectra contained a small fraction of such events. These events were removed in order to obtain ME spectra which contained only beam-related events.

The energy spectrum of the cosmic events was determined from the dedicated cosmic runs during which the electron beam was turned off. After applying the same veto cut as for the scattering data, energy spectra containing cosmic events which were not eliminated by the veto were obtained. Because of the high efficiency of the veto paddles, the number of events not eliminated was very low. Before being able to compare the cosmic-run energy spectrum with the scattering-run energy spectra, the fact that the dead-time of the DAQ system is much higher during a scattering run than during a cosmic run had to be taken into account. This is due to the much larger number of events being processed when the electron beam is on. This was done by normalising the purely cosmic energy spectrum by the ratio of the cosmic-run live-time to the scattering-run live-time. Since the beam was turned off during the purely cosmic runs, there are no events from the cosmic runs that are associated with specific FP channels. A purely cosmic ME spectrum for a specific FP channel was

generated by shifting the total cosmic energy spectrum by an energy equal to the photon energy corresponding to that FP channel, as detailed in Sec. 3.3.3.

Although the major portion of the events in the prompt and accidental energy spectra were beam-related, there were definitely no beam-related events having an energy higher than that of the electron beam since that energy corresponded to the maximum bremsstrahlung-photon energy. In order to determine the energy over which the prompt and accidental ME spectra were purely cosmic in nature, the ME corresponding to the electron-beam energy was calculated for each of the FP channels[8]. Since the cosmic ME spectrum was normalised to the scattering-run live-time, the cosmic ME spectrum in the range above the ME corresponding to the electron-beam energy could be directly compared to the prompt and accidental ME spectra in the same region. By integrating the prompt, accidental and cosmic spectra in this region, the purely cosmic ME spectrum for each of the FP channels was normalised to the accidental ME spectrum for the same FP channel in the region above the electron-beam ME, as shown in Fig. 3.11. The normalisation of the purely cosmic ME spectrum to the prompt ME spectrum was also examined, and was found to show a negligible amount of cosmic background in the prompt window.

3.3.6 Subtraction of accidental background

The cosmic-subtracted 2×62 accidental ME spectra are beam-related. As shown in Ref. [39], the shape of the accidental ME spectrum was independent of the width of the accidental-time cut. This implies that the background part of the cosmic-subtracted prompt ME spectrum for a given FP channel should have the same shape as the cosmic-subtracted accidental ME spectrum for the same FP channel.

Because the accidental window is much wider than the prompt window (Sec. 3.3.4), the accidental ME spectrum must be normalised to the prompt ME spectrum. In order to exclude both elastic- and inelastic-scattering events from the normalisation procedure, the lower limit of the normalisation range was set to +3.0 MeV. This is located well above the elastic scattering peak to guarantee that the normalisation range contains only accidental events in both the prompt and accidental ME spectra. As all beam-related events have energies below the electron-beam energy, the upper limit of the normalisation range was set to the ME corresponding to the electron-beam energy. The normalisation range is shown in Fig. 3.12a.

The prompt and accidental ME spectra were integrated over the ME normalisation range. The ratio of the two integrals was the normalisation factor for the specific pair of spectra. After scaling the accidental ME spectrum by this factor, the resulting spectrum was subtracted from the prompt ME spectrum, yielding a background-free prompt ME spectrum for each FP channel. The normalisation procedure is shown in Fig. 3.12.

3.3.7 Yield calculation

The FP channels were grouped into four FP bins, as shown in Table 3.1. The central photon energy was determined for each of the FP bins. The background-free prompt ME spectra

[8]Example for FP channel 1: $\mathrm{ME}_{\mathrm{beam}} = E_0 - E_\gamma|_{\mathrm{FP\ channel\ 1}} = 164.8 - 100.1\ \mathrm{MeV} = 64.7\ \mathrm{MeV}$

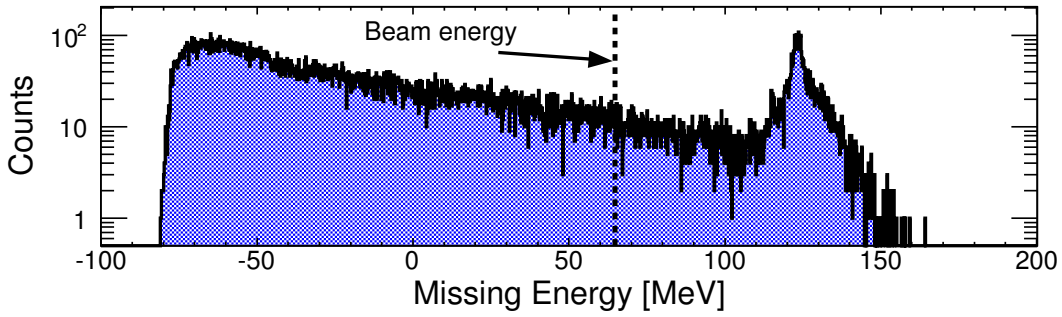

(a)

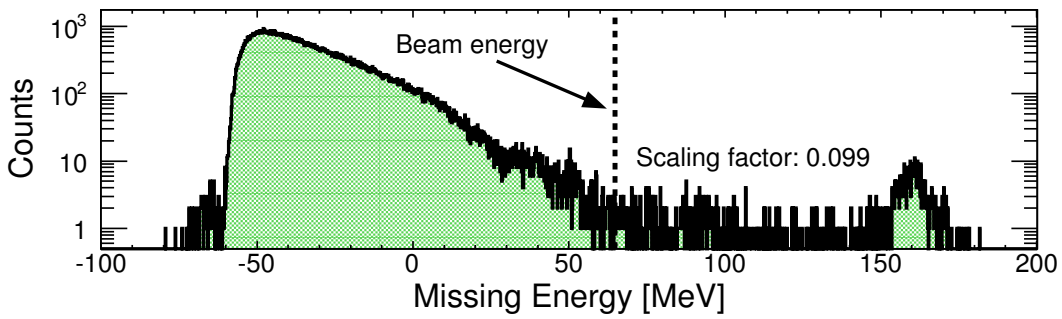

(b)

Figure 3.11: The process of cosmic scaling. (a) Cosmic and (b) accidental ME spectra for focal-plane channel 1. The missing energy corresponding to the electron-beam energy is indicated with the vertical dashed line. The region above this line is integrated for each of the two spectra. The scaling factor is equal to the ratio of the number of events in this region in the accidental spectrum to the number of events in the same region in the cosmic spectrum. The reason for the change in the overflow peak location from ∼125 MeV in the cosmic spectrum to ∼160 MeV in the accidental spectrum is that the overflow bin on the ADCs was modified between runs.

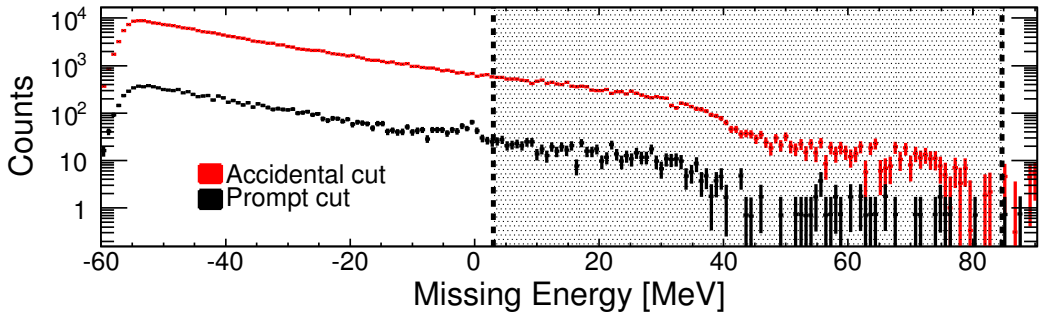

(a)

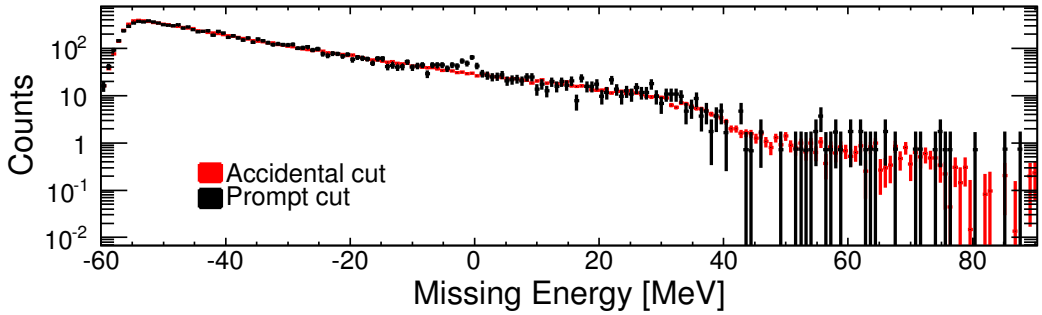

(b)

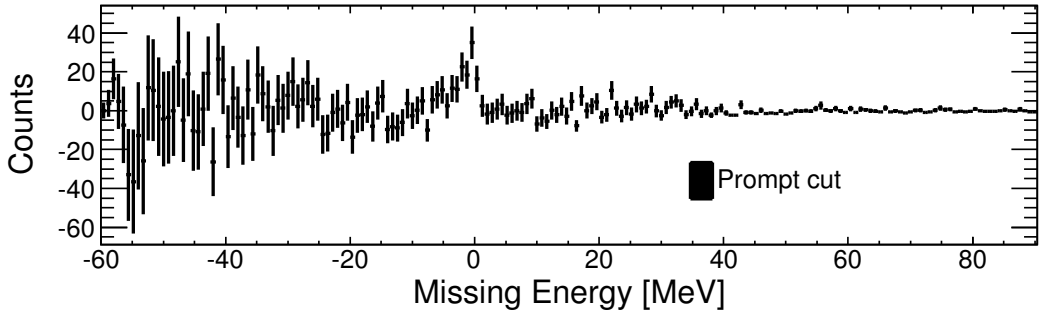

(c)

Figure 3.12: (Colour online) Normalisation and subtraction of accidental background events for FP channel 33. Note the logarithmic scale in (a) and (b). (a) Before normalisation, the number of events was much larger in the accidental ME spectrum than in the prompt ME spectrum. The two spectra were normalised over the shadowed region ranging from ME = 3 MeV to the ME-equivalent of the electron-beam energy which was 84.74 MeV for FP channel 33. (b) After normalisation, the accidental ME spectrum nicely reproduced the background contribution to the prompt ME spectrum. (c) The background-free prompt ME spectrum spectrum was obtained by subtracting the scaled accidental ME spectrum from the prompt ME spectrum. After subtraction, the elastic scattering peak is clearly visible at 0 MeV.

FP bin	FP channels	Photon energy range [MeV]	Central photon energy [MeV]
1	1-16	91.4-100.1	95.9
2	17-32	81.3-90.8	86.2
3	33-48	70.5-80.7	75.7
4	49-62	60.9-69.8	65.5

Table 3.1: Definition of the four FP photon energy bins.

for each of the FP channels inside a specific FP bin were summed, yielding one prompt ME spectrum for each of the FP bins. The result of this procedure for one of the FP bins is shown in Fig. 3.13 for both the single-hit and multi-hit TDC analyses.

In order to obtain the scattered-photon yield, a Region Of Integration (ROI) was defined from -4 MeV to +2.5 MeV in the ME spectrum. The choice of this range was made such that the majority of the scattering peak was included, but any inelastic contributions (the lowest of which lies at -4.44 MeV for ^{12}C) to the yield were excluded.

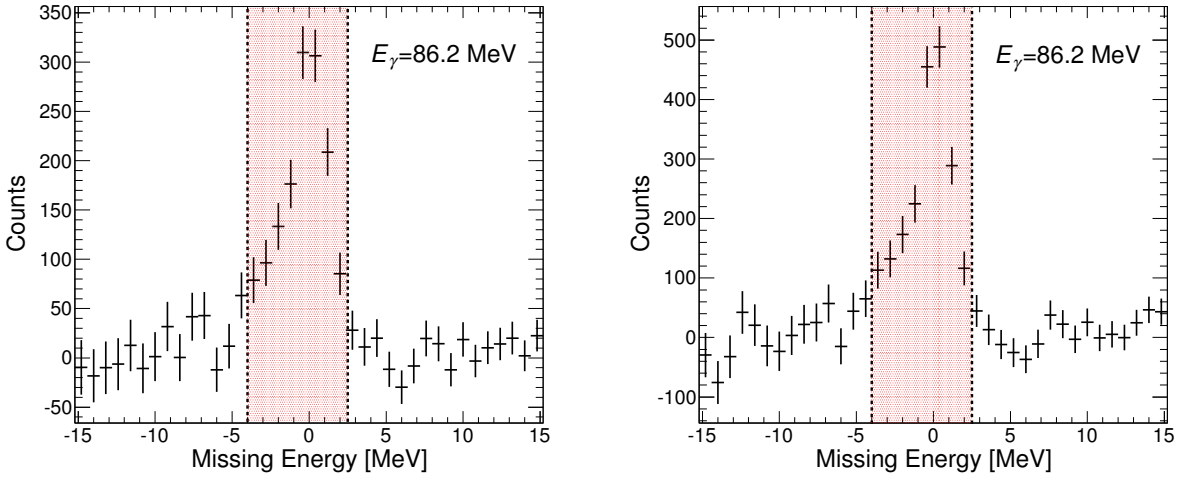

(a) (b)

Figure 3.13: The background-free prompt ME spectrum at $E_\gamma = 86.2$ MeV resulting from the (a) single-hit TDC and (b) multi-hit TDC analysis. The shadowed region is the ROI over which the scattering peak was integrated to obtain the yield. The multi-hit TDC yield is substantially larger than the single-hit TDC yield due to the lack of stolen coincidences in the multi-hit TDC data (see Sec. 3.6).

Integrating the background-free ME spectra resulted in 2×4 yields because of the four bins for each of the two TDC types.

3.4 Tagging efficiency

The photon-scattering cross section is fundamentally related to the number of beam photons incident on the ^{12}C target. The number of photons produced at the radiator was equal to the number of post-bremsstrahlung electrons striking the 100% efficient FP hodoscope. However, the tagged-photon beam was collimated so that all tagged photons struck the target (recall Sec. 2.3.3). This meant that a fraction of the electrons detected by the FP hodoscope corresponded to tagged photons that were collimated. The ratio of the number of tagged photons passing through the collimator to the number of electrons detected at the FP hodoscope was defined as the tagging efficiency ϵ_{tag}.

The method used to determine the tagging efficiency [50, 38] required dedicated tagging-efficiency runs with the 100% efficient Pb-glass detector in the reduced intensity photon beam. A total of 13 tagging-efficiency runs were performed, spread out evenly over the run period. For each FP channel, a histogram of the 13 measurements was produced. A Gaussian was fitted to each of the peaks, which resulted in the average tagging efficiency for the FP channel in question, as shown in Fig. 3.14. The average tagging efficiency over all FP channels was ∼44%.

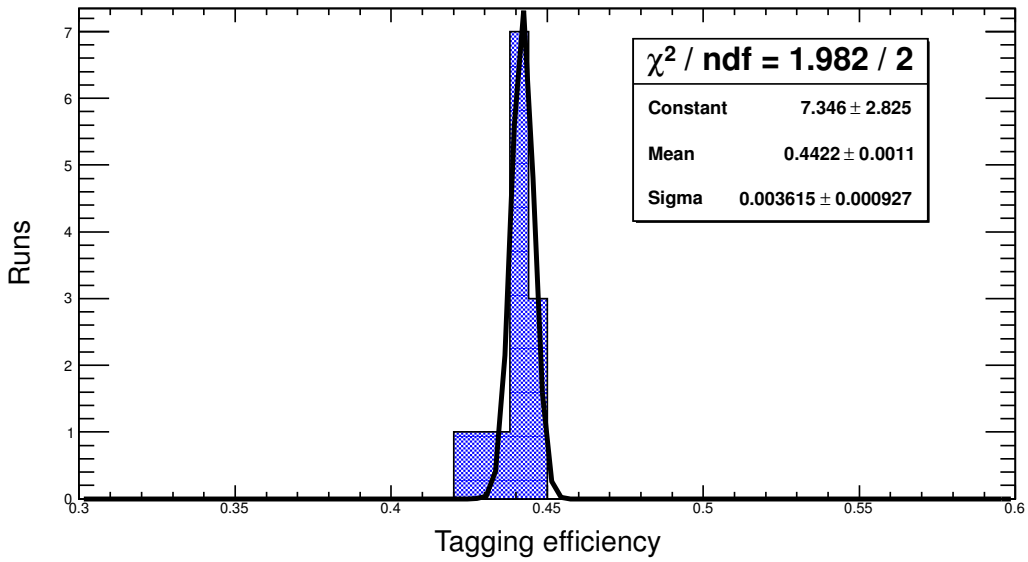

Figure 3.14: Tagging efficiency for FP channel 1. The measurements from the 13 tagging-efficiency runs were histogrammed and a Gaussian fit was used to determine the average tagging efficiency, in this case $\epsilon_{\text{tag}} = 44.2 \pm 0.36\%$.

3.5 Geant4 simulation

GEANT4 [51, 52] is a software package developed at CERN which uses C++ object-oriented programming to simulate the passage of particles through matter. Thus, a program may

be written in which the geometry, materials, dimensions and locations of the components of an experiment are embedded. A GEANT4 simulation of the experimental setup [39] was developed to allow for the determination of both the effective acceptances of the photon detectors and how the placed cuts on the data affected the results.

3.5.1 Overview

The details of the extended photon beam/target interaction were determined as follows:

- The trajectory of a collimated photon and the target geometry resulted in the target illumination.
- For each illuminated trajectory, the beam photon was allowed to interact with the target.
- If the photon scattered along this trajectory in the target, a scattered trajectory was simulated.
- If the scattered-photon trajectory passed through the photon-detector aperture, the event was detected and the energy deposition in the detector determined.

The simulation was run for a very large number of events. In the end, only events where the photon reached the NaI(Tl) crystal and deposited energy were fully processed. The simulation was run for both the in-beam situation for all photon detectors as well as for the scattering situation, where the photon detectors were placed at locations 4-6 in Fig. 2.6. Since the interaction between a photon and different materials depends on the photon energy, the scattering simulation was run for the four different FP-hodoscope energy bins defined in Sec. 3.3.7. This meant that there were a total of eight simulations for each detector — four for each calibration position, and four for each scattering position.

3.5.2 Lineshapes

As GEANT4 allowed for the simulation of the energy deposited in the photon detectors from a large number of photons, a simulated energy spectrum was obtained. This spectrum corresponded to the ideal lineshape of the elastic-scattering peak. The simulated ideal lineshape did not take fluctuations in the light collection of the individual PMTs in the photon detector into account. Such fluctuations led to a broadening of the ideal lineshape. A detector response function was determined by convoluting the ideal lineshape with a Gaussian distribution, as described in Ref. [39].

The first simulated ideal lineshape to be compared with data was the in-beam calibration lineshape. For each of the in-beam spectra, all parameters were freely varied such that χ^2 between the simulated detector response function and the experimental energy spectrum was minimised. In this manner, the width of the convolution Gaussian was determined. The width of this Gaussian is taken to be intrinsically related to the sum of the fluctuations in the PMTs.

The same convolution procedure was then performed with the scattering lineshapes holding the widths determined during the in-beam simulations fixed. This procedure allowed for the GEANT4 simulations to be related to the scattering lineshapes via the in-beam measurements and a phenomenologically determined width parameter.

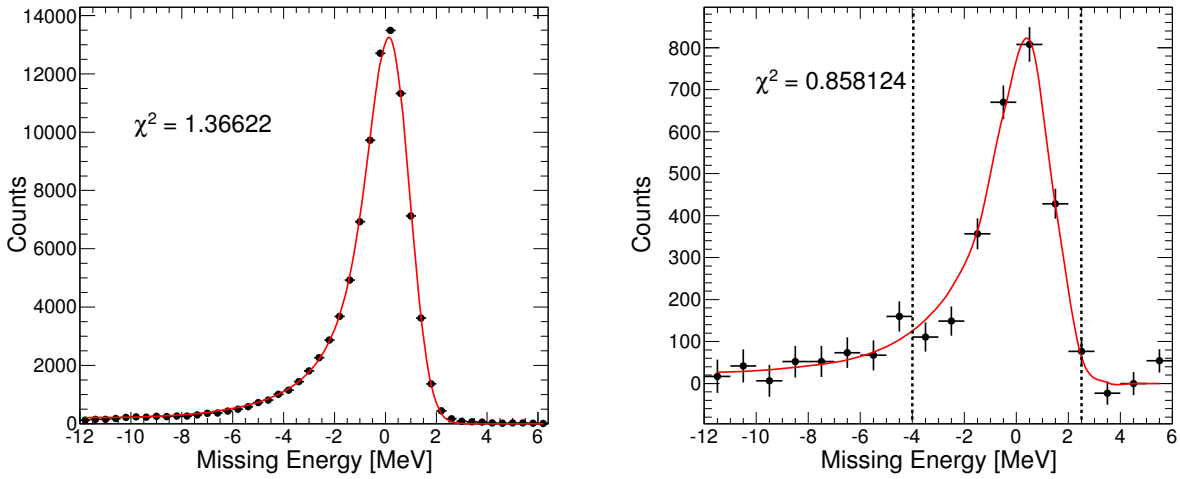

(a) (b)

Figure 3.15: (Colour online) Example fits of the GEANT4 simulation lineshape (red) to the (a) in-beam and (b) scattering data (black). The dashed lines in (b) indicate the limits of the ROI, which is used both to calculate the yield and to obtain corrections needed due to for example the extended photon beam and the extended target. By analysing the simulation results using the same cuts applied in the data analysis, the effects of the cuts on the extracted results could be studied systematically.

3.5.3 Acceptance

As described in the previous section, the simulation generated a large number of scattered-photon rays produced volumetrically at the target. The solid angle subtended by a photon detector is related to the number of photons scattered at the target and the number of photons entering the photon detector. Although there exist analytical methods to calculate the solid angle, a simulation is needed to account for complex effects such as an extended photon beam, an extended target, and photon-detector aperture effects.

Point target and beam

For a point target and beam and a circular photon-detector aperture, the solid angle may be written [53]

$$\Delta\Omega_{\text{point}} = 2\pi\left(1 - \frac{d}{\sqrt{d^2 + r^2}}\right), \tag{3.2}$$

where r is the radius of the photon-detector aperture and d is the distance between the point source and the photon-detector aperture. This is clearly an oversimplification of the experimental situation. For BUNI, $\Delta\Omega_{\text{point}} \sim 67$ msr.

Extended target and beam

In reality, both the target and the photon beam had finite sizes. This meant that there were a large number of scattering locations within the target and resulting scattered-photon trajectories. It is very difficult to determine the magnitudes of these finite-geometry effects with any precision analytically. Instead, they were taken into account using the GEANT4 simulation. The acceptance of a photon detector was calculated using

$$\Delta\Omega_{\text{extended}} = 4\pi \frac{N_{\text{scattered, total}}}{N_{\text{simulated, total}}}*, \tag{3.3}$$

where $N_{\text{scattered, total}}$ was the total number of events striking the detector aperture and lying within the convoluted simulated scattering peak for the photon detector, and $N_{\text{simulated, total}}$ was the total number of simulated events generated at the target. For BUNI, $\Delta\Omega_{\text{extended}} \sim 74$ msr.

3.5.4 Effects of ME cut

As discussed in Sec. 3.3.7, due to inelastic excitations in the target, the entire scattering peak was not integrated to obtain the scattered-photon yield. Instead, a ROI (see Sec. 3.3.7) was defined from -4 MeV to +2.5 MeV in the ME spectrum. The peak was integrated over this region to obtain the yield. By constraining the ROI in this fashion, a number of true events were excluded from the calculation of the yield by design. The fraction of excluded events relative to the total number of scattered events was obtained from the GEANT4 scattering lineshape using

$$R_{\text{ROI}} = \frac{N_{\text{scattered, ROI}}}{N_{\text{scattered, total}}}*, \tag{3.4}$$

where $N_{\text{scattered, ROI}}$ was the number of events inside the ROI in the simulated peak and $N_{\text{scattered, total}}$ was the total number of events in the simulated peak. A typical value for R_{ROI} (the correction for events lying outside the ROI) was ∼50%. The events which were not included in the ROI were located in the tail of the scattering peak.

3.6 Rate-dependent effects

Because of the intensity variations in the extracted electron beam discussed in Sec. 2.2, the instantaneous rate in a FP channel could be as high as 4 MHz. These high instantaneous beam rates caused significant losses in the number of tagged events registered by the experimental setup due to three rate-dependent effects[9]:

*In practice, a single simulation was performed. In order to compare the simulated lineshapes with millions of events in the peak to measured lineshapes with a few thousand events in the peak, a scaling factor related to the Gaussian convolution was introduced.

[9]The rate-dependent effects are discussed in detail in Refs. [37, 54].

- **Ghost events** In order for the TDCs to be stopped, a coincidence between a front-row and a back-row scintillator in the FP hodoscope was needed. When the electron beam rate is high, two random electrons may strike the FP hodoscope almost simultaneously. This is the situation shown in Fig. 3.16, where one random electron causes a coincidence between scintillators F1 and B1 and the other causes a coincidence between F2 and B2. The timing between these two random electrons may be such that it appeared as a single true electron hit the FP hodoscope causing a coincidence between F2 and B1. Such events are called ghost events.

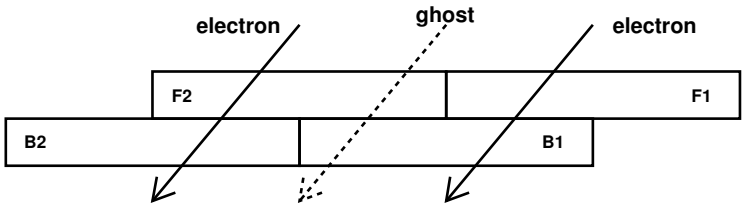

Figure 3.16: Creation of a ghost event. When two random electrons strike two next-to-neighbouring FP channels (formed by scintillators F1·B1 and F2·B2) almost simultaneously, it gives the illusion that a true event occurred which belongs to the FP channel between the two; that is, the channel formed by scintillators F2·B1. Figure from Ref. [37].

- **Missed stops** Missed stops originate in the fact that the very fast FP scalers may register a post-bremsstrahlung electron while the slower FP TDCs miss it. This effect is primarily due to the different pulse-width registration thresholds for the FP scalers ($\sim$3 ns) and the FP TDCs ($\sim$11 ns). The FP scalers could thus register FP coincidence signals that the FP TDCs could not, a serious high-rate asymmetry in the instrumentation electronics that required substantial effort to quantify.

- **Stolen coincidences** When the single-hit FP TDCs are used, an electron striking the FP hodoscope stops the TDC and prevents further collection of data. When the beam rate is high, there is a significant possibility that the electron stopping the FP TDCs is not the true electron corresponding to the tagged photon that started the TDCs, but instead a random or accidental electron. This well-known phenomenon [55] is called a stolen coincidence. As mentioned in Sec. 2.6, multi-hit TDCs were also used to instrument the FP. Multi-hit TDCs eliminate the need to correct the data for stolen coincidences since they accept multiple stop signals from the FP hodoscope.

Well-known analytical methods [55, 56] exist that allow for the stolen-coincidence correction to be performed. Ghost event and missed-stop corrections cannot be addressed analytically. To determine these correction factors, as well as the stolen-coincidence factor, a Monte Carlo simulation of the tagger electronics [37] was employed. The complex time structure of the beam motivated the use of the Monte Carlo simulation. The simulation modelled the electronics and the detection of electrons in the FP in steps of 1 ns. The simulation input parameters were taken both from the electronics setup (pulse widths) and from

the data (electron beam rates and time structure). Typical correction values obtained with the tagger simulation are shown in Table 3.2. The use of multi-hit TDCs instead of single-hit

Correction	Single-hit TDCs (%)	Multi-hit TDCs (%)
Ghost events	1	1
Missed stops	3	3
Stolen coincidences	40	N/A

Table 3.2: Typical values of the three corrections that are needed for the absolute normalisation of experimental data. Note that the stolen-coincidences correction is not needed when multi-hit TDCs are used. See text for details.

TDCs to instrument the FP hodoscope provides a clear improvement in precision, since the need for the stolen-coincidences correction is eliminated. The validity of the simulation and all of the corrections it provides has been shown in Ref. [54].

3.7 Systematic uncertainties

The systematic uncertainties were divided into three categories, as summarised in Table 3.3. Scale systematic uncertainties affected the data obtained at all angles and energies equally. The systematic uncertainty due to the stolen-trues correction varied with both energy and angle and vanished when multi-hit TDCs were employed. There was also a systematic uncertainty associated with the acceptance of the individual NaI(Tl) detectors. This uncertainty varied only with angle but not with energy, and had two origins:

- The distance and aperture size of the detector in its scattering location.
- The effect of placing cuts on the data during analysis.

The systematic uncertainties were combined in quadrature to obtain the overall systematic uncertainty, estimated to be $\sim$7%.

Type	Variable	Value
Scale	Tagging efficiency	∼1%
	Target thickness	∼1%
	Ghost events	∼2%
	Missed stops	∼1%
Angular	Detector acceptance	∼3-4%
Point-to-point	Stolen Trues[1]	∼2-4%
Total		∼5-7%

[1] Only present in the single-hit TDC data.

Table 3.3: Systematic uncertainties.

Chapter 4

Results and conclusion

In Chapter 3, the parameters needed to calculate the differential cross section were introduced. While Eq. 3.1 is the most general expression for the differential cross section based on the experimental parameters, it may be rewritten so that all of the parameters introduced in Chapter 3 are included

$$\frac{d\sigma}{d\Omega} = f_{\text{stolen}}\, f_{\text{missed}}\, f_{\text{ghost}} \frac{N_{\gamma,\text{scattered}}}{\epsilon_{\text{tag}}\, N_e\, \kappa\, (1-\alpha)\, R_{\text{ROI}}\, \Delta\Omega_{\text{extended}}}. \tag{4.1}$$

By combining the various parameters detailed in the previous Chapter in this manner, the absolute differential cross section for $^{12}\text{C}(\gamma,\gamma)^{12}\text{C}$ may be determined.

4.1 Results

The differential cross sections for $^{12}\text{C}(\gamma,\gamma)^{12}\text{C}$ measured in this experiment are shown in Table 4.1.

E_γ	$\frac{d\sigma}{d\Omega}$ (60°) [nb/sr]	$\frac{d\sigma}{d\Omega}$ (120°) [nb/sr]
Single-hit TDC		
65.5	562 ± 42 (7.5%) ± 35 (6.2%)	570 ± 22 (3.9%) ± 29 (5.1%)
75.7	470 ± 28 (6.0%) ± 29 (6.2%)	519 ± 17 (3.3%) ± 25 (4.8%)
86.2	392 ± 27 (6.9%) ± 22 (5.6%)	398 ± 16 (4.0%) ± 18 (4.5%)
95.9	281 ± 23 (8.2%) ± 14 (5.0%)	294 ± 15 (5.1%) ± 13 (4.4%)
Multi-hit TDC		
65.5	517 ± 34 (6.6%) ± 22 (4.3%)	546 ± 19 (3.5%) ± 24 (4.4%)
75.7	432 ± 23 (5.3%) ± 18 (4.2%)	489 ± 15 (3.1%) ± 20 (4.1%)
86.2	368 ± 22 (6.0%) ± 16 (4.3%)	372 ± 14 (3.8%) ± 15 (4.0%)
95.9	250 ± 20 (8.0%) ± 10 (4.0%)	300 ± 14 (4.7%) ± 12 (4.0%)

Table 4.1: Measured cross sections. The first uncertainty is statistical and the second uncertainty is systematic. The data were binned to balance the uncertainties.

4.2 Discussion of results

There were two goals for this experiment:

- procedural: verify the normalisation procedure used in the analysis of Compton scattering data attained during an almost decade-long measurement program at the MAX IV Laboratory.
- scientific: determine whether the polarisabilities of a bound nucleon differ from those of a free nucleon.

4.2.1 Normalisation

Validation of the normalisation procedure is possible via the comparison of results obtained for the $^{12}\mathrm{C}(\gamma,\gamma)^{12}\mathrm{C}$ cross section from this measurement with results from previous measurements. In addition to the measurements presented in Table 1.3, parallel analyses of data from other run periods have recently been completed by Myers *et al.* [57] Fig. 4.1 shows the results of the present work together with previous measurements in the same photon-energy range.

Schelhaas *et al.*

The results from the first measurement of the $^{12}\mathrm{C}(\gamma,\gamma)^{12}\mathrm{C}$ reaction in this energy region were published in 1990 [23]. The experiment was performed at MAMI A in Mainz, Germany using tagged photons in the energy range 15 to 140 MeV. The cross section was determined at scattering angles of 60°, 90°, 120°, and 150°. Four relatively small 25.4 cm-diameter NaI(Tl) photon detectors were used to detect the scattered photons. Thus, a relatively large portion of the EM shower from the scattered photon potentially leaked out of the core of the NaI(Tl) detectors, and extensive modelling would have been necessary to account for this. As seen in Fig. 4.1, the statistical uncertainty in the results is much larger than in complimentary measurements, including this one. The systematic uncertainties of this measurement are not given by Ref. [23], but are estimated to be on the same order as the statistical uncertainties. The agreement with the results of this work is good at 120°, but not at 60°.

Häger *et al.*

Häger *et al.* [25] published the results of an experiment performed at MAX-lab in 1995. In this experiment, tagged photons with energies of 58 MeV and 75 MeV were used. The cross section was determined at scattering angles of 45°, 60°, 90°, 120°, and 135°. Four 25.4 cm-diameter NaI photon detectors were again used to detect the scattered photons. Once again, a relatively large portion of the EM shower from the scattered photon potentially leaked out of the core of the NaI(Tl) detectors, and extensive modelling would have been necessary to account for this. The statistical uncertainties in these data are significantly better, comparable with those obtained in this work. The systematic uncertainties were ∼4%. The agreement with the results of this work is good at 60°, but not at 120°.

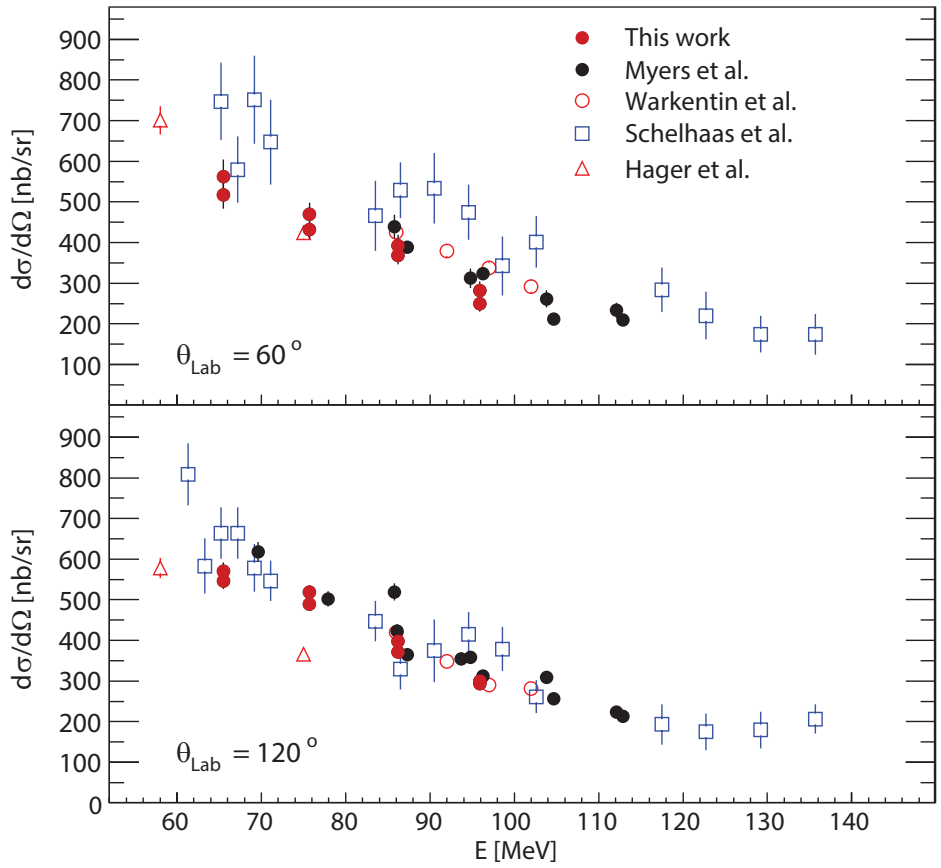

Figure 4.1: (Colour online) Measurement of the $^{12}C(\gamma,\gamma)^{12}C$ cross section at laboratory angles of 60° and 120° from the present work compared with previous measurements. Statistical uncertainties are shown. Agreement with the results of Warkentin *et al.* is very good. See text for details.

Warkentin *et al.*

Warkentin *et al.* [26] published the results of an experiment performed at SAL in Saskatoon, Canada in 2001. In this experiment, tagged photons in the energy range 84 to 105 MeV were used. The cross section was determined at scattering angles of 35°, 60°, 90°, 120°, and 150°. The scattered photons were detected with BUNI (see Sec. 2.5.1). By employing the large NaI(Tl) detector, corrections for the leakage of the EM shower from the core were avoided, dramatically improving the precision of the measurement. The statistical uncertainties obtained are comparable with those obtained in this measurement. The systematic uncertainties were ∼4%. The agreement with the results of this work is excellent at both 60° and 120°. These results also agree very well with the results of Myers *et al.*

The excellent agreement with the previous results of Warkentin *et al.* demonstrates a thorough understanding of the normalisation procedure used in the extraction of the cross section. **As the normalisation procedure for carbon is the same as that for deuterium, it is concluded that the normalisation of the soon-to-be released deuterium results is sound**[1]**.**

4.2.2 Bound-nucleon polarisabilities

As shown in Fig. 1.3 and discussed in Sec. 1.3.3, the differential cross section for Compton scattering off a nucleus at a specific angle and a specific energy in this energy range should be proportional to Z^2, where Z is the number of protons in the target nucleus. Fig. 4.2 demonstrates good agreement between the results of the present work at 120° and the cross section based on the coherent-scattering prediction. Clearly, the fundamental picture is sound. A comparison between data obtained at 60° and at higher photon energies is not possible due to the lack of previous results for other nuclei at this scattering angle. This is a fact which is likely to change, since Compton scattering experiments on ^{2}H [13], ^{3}He [58], and ^{6}Li [21, 58] are either planned or are currently being analysed.

In order to draw conclusions about whether the nucleon polarisabilities are affected when the nucleon is bound inside a nucleus, a phenomenological model of nuclear Compton scattering may be applied [22, 57]. The results obtained in this thesis have been compared to this model, which potentially allows for the determination of the magnitude of any bound-nucleon changes in the polarisabilities [57]. **The comparison indicates that there is a difference between the free-nucleon polarisabilities and the bound-nucleon polarisabilities.** However, the precision of the current ^{12}C$(\gamma,\gamma)^{12}$C world data set does not allow for determination of the source of this difference. While the details of the phenomenological analysis of these data are beyond the scope of this thesis, the interested reader is directed towards Ref. [57] for a thorough discussion.

4.3 Conclusion

The activities presented in this thesis were performed in order to extract the absolute differential cross section for the ^{12}C$(\gamma,\gamma)^{12}$C reaction in the photon-energy range 65-95 MeV.

[1] Analysis of scattering data from ^{6}Li and ^{16}O is also underway.

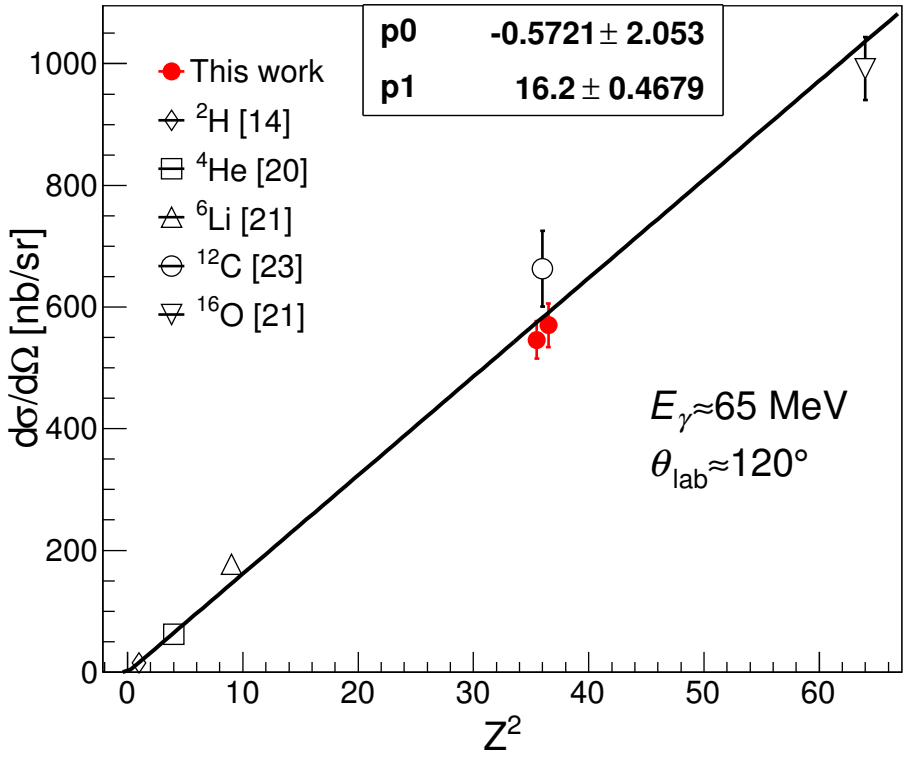

Figure 4.2: (Colour online) ^{12}C$(\gamma,\gamma)^{12}$C cross section at $E_\gamma = 65.5$ MeV and $\theta_{\rm lab} = 120°$ from the present work compared with previous measurements. Statistical uncertainties are shown.

The goals of the experiment were:

- Validate the procedure used for the normalisation of Compton-scattering data acquired during an almost decade-long measurement program at the MAX IV Laboratory.
- Determine whether the free-nucleon polarisabilities change when the nucleon is bound.

Based upon the agreement between the results presented here and previous data, it is concluded that the normalisation procedure we have developed is valid. Indications are that the bound-nucleon polarisabilities differ from the free-nucleon values; however, our results do not have the required precision to indicate the source of these effects.

Bibliography

[1] H. Yukawa *Proc. Phys. Math. Soc. Japan*, vol. 17, no. 48, 1935.

[2] C. M. G. Lattes, H. Muirhead, G. P. S. Occhialini, *et al. Nature*, vol. 159, no. 4047, p. 694, 1947.

[3] M. Gell-Mann *Phys. Lett.*, vol. 8, no. 3, p. 214, 1964.

[4] G. Zweig *CERN Report No.8182/TH.401.*, 1964.

[5] R. Machleidt and D. R. Entem *Phys. Rep.*, vol. 503, p. 1, 2011.

[6] J. D. Jackson, *Classical Electrodynamics*. Wiley, 3 ed., 1998.

[7] A. H. Compton *Phys. Rev.*, vol. 21, no. 5, p. 483, 1923.

[8] J. L. Powell *Phys. Rev.*, vol. 75, no. 1, p. 32, 1949.

[9] F. Wissmann, *Compton Scattering: Investigating the Structure of the Nucleon with Real Photons*. Springer, 2003.

[10] V. A. Petrun'kin *Sov. J. Part. Nucl.*, vol. 12, p. 278, 1981.

[11] D. Babusci, G. Giordano, A. I. L'vov, *et al. Phys. Rev. C*, vol. 58, no. 2, p. 1013, 1998.

[12] A. M. Baldin *Nucl. Phys.*, vol. 18, p. 310, 1960.

[13] H. W. Grießhammer, J. A. McGovern, D. R. Phillips, *et al. Prog. Part. Nucl. Phys.*, vol. 67, p. 841, 2012.

[14] M. Lundin, J.-O. Adler, M. Boland, *et al. Phys. Rev. Lett.*, vol. 90, p. 192501, 2003.

[15] J. Beringer, J.-F. Arguin, R. M. Barnett, *et al. Phys. Rev. D*, vol. 86, p. 010001, 2003.

[16] M. A. Lucas, *Compton scattering from the deuteron at intermediate energies*. PhD thesis, University of Illinois at Urbana-Champaign, 1994.

[17] D. L. Hornidge, B. J. Warkentin, R. Igarashi, *et al. Phys. Rev. Lett.*, vol. 84, p. 2334, 2000.

[18] D. P. Wells, *Elastic photon scattering from 4He between 23 and 73 MeV*. PhD thesis, University of Illinois at Urbana-Champaign, 1990.

[19] K. Fuhrberg, D. Häger, T. Glebe, *et al. Nucl. Phys. A*, vol. 591, p. 1, 1995.

[20] S. Proff, C. Pöch, T. Glebe, *et al. Nucl. Phys. A*, vol. 646, p. 67, 1999.

[21] L. S. Myers, M. W. Ahmed, G. Feldman, *et al. Phys. Rev. C*, vol. 86, p. 044614, 2012.

[22] D. H. Wright, P. T. Debevec, L. J. Morford, *et al. Phys. Rev. C*, vol. 32, no. 4, p. 1174, 1985.

[23] K. P. Schelhaas, J. M. Henneberg, N. Wieloch-Laufenberg, *et al. Nucl. Phys. A*, vol. 506, p. 307, 1990.

[24] M. Ludwig, B.-E. Andersson, A. Baumann, *et al. Phys. Lett. B*, vol. 274, p. 275, 1992.

[25] D. Häger, K. Fuhrberg, T. Glebe, *et al. Nucl. Phys. A*, vol. 595, p. 287, 1995.

[26] B. J. Warkentin, D. L. Hornidge, R. Igarashi, *et al. Phys. Rev. C*, vol. 64, p. 014603, 2001.

[27] K. E. Mellendorf, *Photon scattering from 16O above the giant dipole resonance.* PhD thesis, University of Illinois at Urbana-Champaign, 1993.

[28] G. Feldman, K. E. Mellendorf, R. A. Eisenstein, *et al. Phys. Rev. C*, vol. 54, p. R2124, 1996.

[29] G. Bampa, W. Leidemann, and H. Arenhövel *Phys. Rev. C*, vol. 84, p. 034005, 2011.

[30] J.-O. Adler, M. Boland, J. Brudvik, *et al. Nucl. Instrum. Methods Phys. Res. Sect. A*, vol. 715, p. 1, 2013.

[31] B. Schröder, "The MAX-lab Facility and COMPTON@MAX-lab," in *Workshop on Soft Photons and Light Nuclei, Seattle, Washington*, 2008.

[32] Å. Andersson, M. Eriksson, S. Werin, *et al. Nucl. Instrum. Methods Phys. Res. Sect. A*, vol. 445, p. 413, 2000.

[33] L.-J. Lindgren *Nucl. Instrum. Methods Phys. Res. Sect. A*, vol. 492, p. 299, 2002.

[34] R. A. Jebali, *Measurement of the γ + ^{4}He Total Photoabsorption Cross-Section using a Gas-Scintillator Active Target.* PhD thesis, University of Glasgow, 2013.

[35] K. G. Fissum, *Inclusive photoproduction of positive pions.* PhD thesis, University of Saskatchewan, 1993.

[36] L. I. Schiff *Phys. Rev.*, vol. 83, no. 2, p. 252, 1951.

[37] L. S. Myers, G. Feldman, K. G. Fissum, *et al. Nucl. Instrum. Methods Phys. Res. Sect. A*, vol. 729, p. 707, 2013.

[38] M. Meshkian, *Photon-Tagging Measurements at MAX-lab.* BSc thesis, Lund University, 2012.

[39] L. S. Myers, *Deuteron Compton scattering below pion threshold.* PhD thesis, University of Illinois at Urbana-Champaign, 2010.

[40] J. H. Hubbell *Natl. Stand. Ref. Data Ser.*, vol. 29, 1969.

[41] NIST XCOM: Photon Cross Sections Database. Available on March 20, 2014 at `http://physics.nist.gov/PhysRefData/Xcom/html/xcom1.html`.

[42] B. R. Martin and G. Shaw, *Particle Physics.* John Wiley & Sons, 3 ed., 2008.

[43] M. Preston, *Time and energy calibration of large-volume segmented sodium-iodide detectors.* BSc thesis, Lund University, 2012.

[44] J. P. Miller, E. J. Austin, E. C. Booth, *et al. Nucl. Instrum. Methods Phys. Res. Sect. A*, vol. 270, p. 431, 1988.

[45] F. Wissmann, J. Peise, M. Schmitz, *et al. Phys. Lett. B*, vol. 335, no. 2, p. 119, 1994.

[46] P. A. Čerenkov, "Radiation of particles moving at a velocity exceeding that of light, and some of the possibilities for their use in experimental physics," in *Nobel Lecture*, 1958.

[47] R. Brun and F. Rademakers *Nucl. Instrum. Methods Phys. Res. Sect. A*, vol. 389, p. 81, 1997.

[48] I. Antcheva, M. Ballintijn, B. Bellenot, *et al. Comput. Phys. Commun.*, vol. 180, p. 2499, 2009.

[49] M. Lundin, *Compton Scattering from the Deuteron at Low Energies.* PhD thesis, Lund University, 2002.

[50] M. Litwack, *MAX-lab May09 Tagging-Efficiency Measurement.* BSc thesis, Lund University, 2010.

[51] S. Agostinelli, J. Allison, K. Amako, *et al. Nucl. Instrum. Methods Phys. Res. Sect. A*, vol. 506, p. 250, 2003.

[52] J. Allison, K. Amako, J. Apostolakis, *et al. IEEE T. Nucl. Sci.*, vol. 53, p. 270, 2006.

[53] G. K. Knoll, *Radiation detection and measurement.* John Wiley & Sons, 2 ed., 1989.

[54] M. F. Preston, L. S. Myers, J. R. M. Annand, *et al. Nucl. Instrum. Methods Phys. Res. Sect. A*, vol. 744, p. 17, 2014.

[55] R. O. Owens *Nucl. Instrum. Methods Phys. Res. Sect. A*, vol. 288, p. 574, 1990.

[56] L. V. Hoorebeke *Nucl. Instrum. Methods Phys. Res. Sect. A*, vol. 288, p. 574, 1990.

[57] L. S. Myers, K. Shoniyozov, M. F. Preston, *et al. Phys. Rev. C*, vol. 89, p. 035202, 2014.

[58] J. R. M. Annand, "Compton Scattering on He Isotopes Active Target Experiments," in *Compton scattering off Protons and Light Nuclei: pinning down the nucleon polarizabilities, Trento, Italy*, 2013.

Appendix A

Tagged photon energies

FP bin 1			FP bin 2			FP bin 3			FP bin 4		
FP channel	E' [MeV]	E_γ [MeV]	FP channel	E' [MeV]	E_γ [MeV]	FP channel	E' [MeV]	E_γ [MeV]	FP channel	E' [MeV]	E_γ [MeV]
1	64.6	100.1	17	73.9	90.8	33	84.1	80.7	49	94.9	69.8
2	65.2	99.6	18	74.6	90.2	34	84.7	80.0	50	95.6	69.2
3	65.8	99.0	19	75.2	89.6	35	85.4	79.4	51	96.3	68.5
4	66.3	98.4	20	75.8	89.0	36	86.1	78.7	52	97.0	67.8
5	66.9	97.9	21	76.4	88.4	37	86.7	78.0	53	97.7	67.1
6	67.4	97.3	22	77.0	87.7	38	87.4	77.4	54	98.4	66.4
7	68.0	96.7	23	77.6	87.1	39	88.1	76.7	55	99.1	65.7
8	68.6	96.2	24	78.3	86.5	40	88.8	76.0	56	99.8	65.0
9	69.2	95.6	25	78.9	85.9	41	89.4	75.3	57	100.4	64.3
10	69.8	95.0	26	79.5	85.2	42	90.1	74.6	58	101.1	63.6
11	70.4	94.4	27	80.2	84.6	43	90.8	74.0	59	101.8	63.0
12	71.0	93.8	28	80.8	83.9	44	91.5	73.3	60	102.5	62.3
13	71.5	93.2	29	81.5	83.3	45	92.2	72.6	61	103.2	61.6
14	72.1	92.6	30	82.1	82.7	46	92.9	71.9	62	103.8	61.0
15	72.7	92.0	31	82.8	82.0	47	93.6	71.2			
16	73.3	91.4	32	83.4	81.3	48	94.2	70.5			

Table A.1: Tagged photon energies employed in the experiment. The electron-beam energy was 164.8 MeV.

Appendix B

Publications

This thesis is based on the results presented in the following publications:

- **Tests of the Monte Carlo simulation of the photon-tagger focal-plane electronics at the MAX IV Laboratory**
  Nucl. Instrum. Methods Phys. Res. Sect. A **744**, 17 (2014)
  arXiv: 1311.5692 [physics.ins-det]
  http://dx.doi.org/10.1016/j.nima.2014.01.040
  M. F. Preston, L. S. Myers, J. R. M. Annand, K. G. Fissum, K. Hansen, L. Isaksson, R. Jebali, and M. Lundin

- **Compton scattering from ^{12}C using tagged photons in the energy range 65-115 MeV**
  Phys. Rev. C **89**, 035202 (2014)
  arXiv: 1401.4028 [nucl-ex]
  http://dx.doi.org/10.1103/PhysRevC.89.035202
  L. S. Myers, K. Shoniyozov, M. F. Preston, M. D. Anderson, J. R. M. Annand, M. Boselli, W. J. Briscoe, J. Brudvik, J. I. Capone, G. Feldman, K. G. Fissum, K. Hansen, S. S. Henshaw, L. Isaksson, R. Jebali, M. A. Kovash, K. Lewis, M. Lundin, I. J. D. MacGregor, D. G. Middleton, D. E. Mittelberger, M. Murray, A. M. Nathan, S. Nutbeam, G. V. O'Rielly, B. Schröder, B. Seitz, S. C. Stave, and H. R. Weller

Nuclear Instruments and Methods in Physics Research A 744 (2014) 17–20

Contents lists available at ScienceDirect

Nuclear Instruments and Methods in Physics Research A

journal homepage: www.elsevier.com/locate/nima

Tests of the Monte Carlo simulation of the photon-tagger focal-plane electronics at the MAX IV Laboratory

M.F. Preston [a], L.S. Myers [b,1], J.R.M. Annand [c], K.G. Fissum [a,*], K. Hansen [e], L. Isaksson [e], R. Jebali [d,2], M. Lundin [e]

[a] Lund University, SE-221 00 Lund, Sweden
[b] Duke University, Durham, NC 27708, USA
[c] University of Glasgow, Glasgow G12 8QQ, Scotland, UK
[d] Arktis Radiation Detectors Limited, 8045 Zürich, Switzerland
[e] MAX IV Laboratory, Lund University, SE-221 00 Lund, Sweden

ARTICLE INFO

Article history:
Received 17 December 2013
Accepted 15 January 2014
Available online 29 January 2014

Keywords:
Tagger hodoscope
Rate dependencies
Multi-hit time-to-digital converters

ABSTRACT

Rate-dependent effects in the electronics used to instrument the tagger focal plane at the MAX IV Laboratory were recently investigated using the novel approach of Monte Carlo simulation to allow for normalization of high-rate experimental data acquired with single-hit time-to-digital converters (TDCs). The instrumentation of the tagger focal plane has now been expanded to include multi-hit TDCs. The agreement between results obtained from data taken using single-hit and multi-hit TDCs demonstrate a thorough understanding of the behavior of the detector system.

1. Introduction

The Tagged-Photon Facility (TPF) [1,2] at the MAX IV Laboratory [3] in Lund, Sweden has been used to measure photonuclear cross-sections in many experiments. Rate-dependent deadtime and other effects in the electronics used to instrument the tagger focal plane (FP) must be correctly addressed in order to properly normalize the experimental data. These effects are particularly important because of the intermittently high instantaneous photon-beam flux caused by the non-uniform time structure of the photon beam. Limitations in the FP instrumentation electronics were also problematic. An in-depth investigation of the rate-dependent effects at the TPF was recently reported [4] in which the novel approach of Monte Carlo simulation was employed. The behavior of the FP instrumentation electronics was successfully modeled for each detected electron in 1 ns steps. Input parameters were taken directly from the electronics setup (such as pulse widths) or from the data itself (such as electron rates and time structure of the electron beam).

The major limitation in the original electronic instrumentation system for the FP which led to large corrections at high rates was the use of single-hit time-to-digital converters (TDCs). These TDCs were used to measure the elapsed time between a photon-induced reaction product and a post-bremsstrahlung electron corresponding to the photon in question. Understanding the behavior of the single-hit TDCs at high rates has enabled the absolute normalization of data [5]. Recently, the instrumentation of the tagger FP has been upgraded to include multi-hit TDCs, that is, TDCs which are sensitive to more than one stop signal they receive when triggered. Such TDCs are superior to their single-hit predecessors as the data they provide eliminate the need for a large rate-dependent correction to the absolute experiment normalization (see below). This in turn simplifies the data analysis.

In this paper, we present a detailed analysis of the behavior of the tagger FP instrumented with multi-hit TDCs. We compare this behavior to that of the tagger FP instrumented with single-hit TDCs and demonstrate good agreement. Finally, we present absolute cross-section data obtained using both devices and compare it to existing data to demonstrate a thorough understanding of the behavior of the detector system.

2. Facility overview

At the TPF, photon taggers [6–8] and the well-known photon-tagging technique [1,9,10] (see Fig. 1) are used to perform photonuclear investigations. A pulse-stretched electron beam [11] with an energy of up to 200 MeV is used to produce bremsstrahlung as it passes through a ~100 μm Al radiator. The resulting bremsstrahlung

* Corresponding author. Tel.: +46 46 222 9677; fax: +46 46 222 4709.
E-mail address: kevin.fissum@nuclear.lu.se (K.G. Fissum).
[1] Present address: Thomas Jefferson National Accelerator Facility, Newport News, VA 23606, USA.
[2] Present address: University of Glasgow, Glasgow G12 8QQ, Scotland, UK.

0168-9002/$ - see front matter © 2014 Elsevier B.V. All rights reserved.
http://dx.doi.org/10.1016/j.nima.2014.01.040

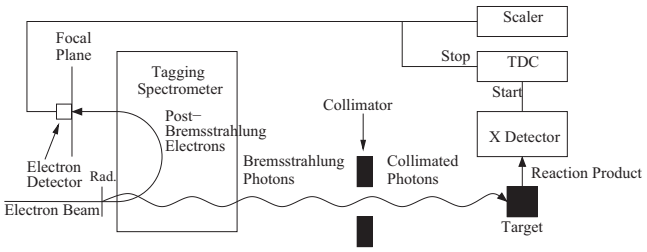

Fig. 1. The photon-tagging technique. Beam electrons may radiate bremsstrahlung photons. Post-bremsstrahlung electrons are momentum analyzed using a photon tagger. Bremsstrahlung photons which pass through the collimator to strike the target may induce photonuclear reactions. The coincidence between a reaction product and a post-bremsstrahlung electron is a tagged-photon event. Figure from Ref. [4].

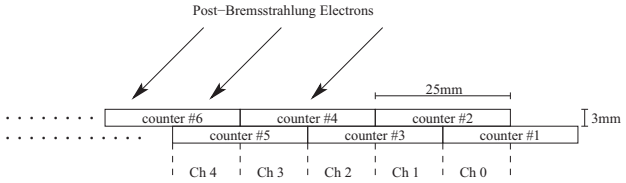

Fig. 2. The FP hodoscope in 50%-overlap configuration. A coincidence between a detector in the front plane and a detector in the back plane defines a tagger channel. There are a total of 63 detectors and thus 62 channels in the FP. Figure from Ref. [4].

photon beam is collimated prior to striking the experimental target. Post-bremsstrahlung electrons are momentum-analyzed in the tagging spectrometer equipped with a 63-detector plastic-scintillator array positioned at the focal plane. A prompt coincidence between a photonuclear reaction product and a post-bremsstrahlung electron in the scintillator array indicates a tagged-photon event.

The energy of the tagged photon is determined from the difference between the energy of the incident electron beam and the energy of the post-bremsstrahlung electron detected in the scintillator focal plane (FP). The measured cross-section is given by

$$\frac{d\sigma}{d\Omega} = \frac{Y_{\text{coincidence}}/\varepsilon_{\text{detector}}}{N_{\text{target}} \cdot N_{\text{electrons}} \cdot \varepsilon_{\text{tagg}} \cdot \Delta\Omega} \quad (1)$$

where $Y_{\text{coincidence}}$ is the number of true, prompt coincidences between the reaction-product detector and the FP, $\varepsilon_{\text{detector}}$ is the reaction-product detector efficiency, N_{target} is the number of target nuclei per unit area, $N_{\text{electrons}}$ is the number of electrons detected in the FP array and counted in the FP scalers, $\varepsilon_{\text{tagg}}$ is the probability that a taggable bremsstrahlung photon passes through the beam-defining collimator and hits the target [1], and $\Delta\Omega$ is the solid angle subtended by the reaction-product detector. Both $Y_{\text{coincidence}}$ and $N_{\text{electrons}}$ must be corrected for the effects of deadtime in the instrumentation electronics, and the size of the corrections depends on the count rate. This is complicated by the fact that the electron beam delivered by the accelerator has a periodic structure of varying intensity. As a result, the instantaneous FP rate can be almost a factor of 4 higher than the average FP rate (typically 3 MHz/MeV) at 20 nA, a typical average operating current.

The FP hodoscope consists of two parallel rows of NE110 scintillators. The front row nearest the exit window of the tagger magnet has 31 elements, while the back row has 32 elements (see Fig. 2). The signals from the detectors are passed to LRS 4413 leading-edge discriminators operated in burst-guard mode. The resulting logic signals are typically set to 25 or 50 ns. Overlap coincidence modules designed and built at the Saskatchewan Accelerator Laboratory (SAL) are used to identify coincidences between two physically overlapping detectors in the front and back rows. An output pulse is generated whenever the two input pulses overlap and is ended whenever one or both inputs are reset. An overlap of at least 3 ns is necessary to produce an output pulse. These coincidences define FP channels and are used to stop TDCs and increment scalers. When a post-bremsstrahlung electron event occurs in coincidence with a trigger from the experiment detectors, a tagged-photon event may have occurred.

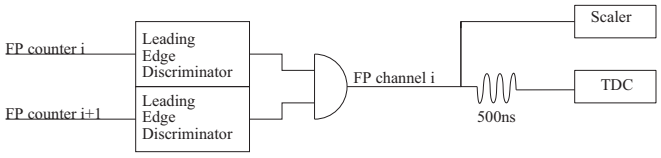

Fig. 3. The FP electronics. A coincidence between an electron-detector signal in the front plane of the FP and an electron-detector signal in the back plane of the FP defines a tagger channel. The coincidence module looking for these overlaps was from SAL. This signal was counted and used to stop a TDC started by the photonuclear reaction-product detector.

The device labeled TDC in Figs. 1 and 3 represents both single-hit and multi-hit TDCs – that is, both devices are used in parallel – started by the same start signal and stopped by the same stop signal (s). The single-hit TDC used to instrument the FP array is the CAEN V775. The V775 is a 32 channel device with 12 bit resolution. It is operated in common-start mode. The stop comes from the first signal presented by a FP channel. It was experimentally determined that to be registered by the TDC, the stop signals corresponding to a FP channel had to correspond to a timing overlap of at least $\sim$11 ns between the front row and back row signals. The multi-hit TDC used to instrument the FP array is the CAEN V1190B. The V1190B is a 64 channel device with 19 bit resolution. Once triggered, it uses one of the FP channel signals as the timing reference signal.[3] The module was programmed to accept up to 4 stop signals per channel for each trigger.[4] It was experimentally determined that these stop signals also had to be at least $\sim$11 ns in width. The device labeled scaler in Figs. 1 and 3 is a CAEN V830 scaler. The V830 is a 32 channel latching device with a 250 MHz counting capability. It was experimentally determined to register pulses as short as $\sim$3 ns in width, the limit of our FP-trigger setup.

Two advantages of requiring a coincidence between the front and back rows of electron detectors in the FP array are that registration of the background in the experimental hall is greatly suppressed, and that the photon-energy resolution may be easily increased simply by offsetting the two scintillator planes.

3. Rate-dependent effects

As the electron beam has a varying periodic intensity, high instantaneous post-bremsstrahlung electron event rates can occur. The resulting rate-dependent effects may result in significant losses in the number of events registered by the FP array instrumentation. Unless taken carefully into consideration, these rate-dependent effects prevent the absolute normalization of the experimental data. Rate-dependent effects include ghost events, missed stops, and stolen coincidences (see below). Table 1 summarizes typical values for rate-dependent corrections to the number of post-bremsstrahlung electrons detected by the FP array for both the single-hit and multi-hit TDCs.

[3] See http://www.caen.it/csite/CaenProd.jsp?idmod=787&parent=11 for details.

[4] In order to address the rate-dependent stolen-coincidence effect (see Section 3.3), a record of the first 2 signals presented by a FP channel is sufficient. We record the first 4 signals in order to be able to better confirm that our instrumentation electronics are behaving as expected.

Table 1
A summary of corrections to the number of tagged events registered by the FP array required for the absolute normalization of experimental data. Note that the stolen-coincidences correction is unnecessary when multi-hit TDCs are used, a distinct advantage. See text for details.

Correction	Single-hit TDCs (%)	Multi-hit TDCs (%)
Ghost events	1	1
Missed stops	3	3
Stolen coincidences	40	N/A

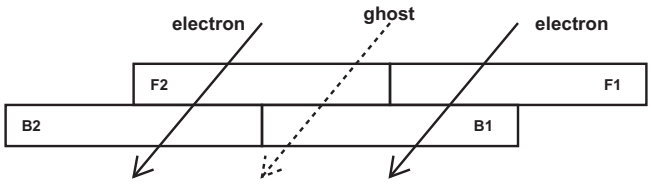

Fig. 4. Creation of a ghost event. Real post-bremsstrahlung electrons (solid arrows) in next-to-neighboring FP channels arrive at almost the same time. This creates the illusion – or ghost – of an electron (dashed arrows) in the counters that constitute the intermediate FP channel. Figure from Ref. [4].

3.1. Ghost events

A major disadvantage of requiring a coincidence between the front and back rows of electron detectors in the FP array is the creation of ghost events at high rates. The ghost events result from the instrumentation of the FP array. The scenario leading to a ghost event is illustrated in Fig. 4. Two different post-bremsstrahlung electrons strike next-to-neighboring channels (counters F1 · B1 and F2 · B2) at nearly the same time which creates the illusion of an electron in the channel in between (counters F1 · B2) – the ghost event. The rate of the accidental coincidences that result in ghost events depends on the post-bremsstrahlung electron rate, the widths of the FP discriminator output pulses, and the resolving time of the overlap coincidence modules. Because these ghosts are formed in the FP electronics, they are registered as coincidences in both the FP scalers and the FP TDC modules, resulting in a partial but not complete cancellation of the effect. As the rate of ghost events is purely a function of post-bremsstrahlung electron rate and FP geometry, they affect both single-hit and multi-hit TDC data equally. They are best addressed using the simulation approach detailed in Ref. [4].

3.2. Missed stops

A missed stop occurs when the FP scalers register a recoil-electron event while the FP TDCs miss it. The primary origin of missed stops lies in the different minimum pulse width for registration in the FP scalers (~ 3 ns) and TDCs (~ 11 ns). This deadtime effect is best addressed using the simulation approach detailed in Ref. [4].

3.3. Stolen coincidences

When single-hit TDCs are employed, due to the fact that the TDC only registers the first signal presented to it subsequent to the start, an accidental post-bremsstrahlung electron may be detected in the FP channel before the actual post-bremsstrahlung electron that corresponds to the tagged photon. The result is that the single-hit TDC is stopped too early, leading to a well-studied phenomenon known as stolen coincidences – see Fig. 5. Well-known methods [12,13] exist for determining the stolen-coincidence correction. It may also be efficiently addressed using the simulation approach detailed in Ref. [4] or greatly reduced by implementing multi-hit TDCs.

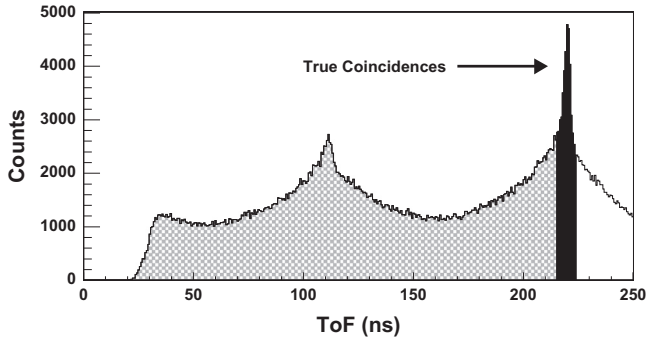

Fig. 5. The stolen-coincidence effect in a single-hit TDC spectrum acquired at a high post-bremsstrahlung electron rate. The black peak at channel 225 represents true coincidences between the reaction-product detector and the FP array, and is the earliest possible time that a true coincidence may be registered. Events in the lightly shaded region correspond to accidental post-bremsstrahlung electrons that stop the FP TDCs before this earliest possible point in time. The coincidence is thus mis-timed and the true coincidence event is stolen when a single-hit TDC is used. Note that the "peak" at channel 110 is an artifact of the extracted electron beam. Figure from Ref. [4].

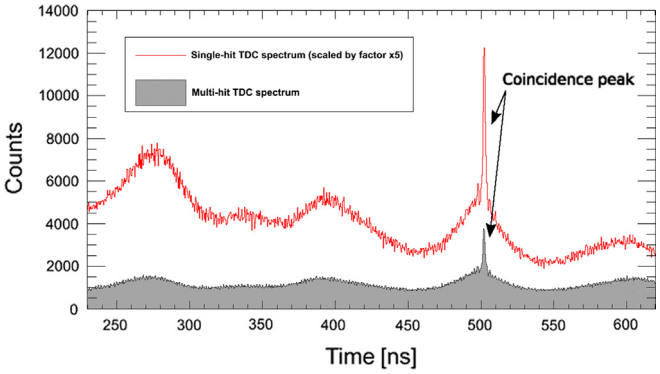

Fig. 6. A comparison between single-hit (red, unshaded) and multi-hit (gray, shaded) FP TDC spectra obtained simultaneously. Note the 5 × scaling of the single-hit TDC spectrum. The time structure in the spectra is due to the method by which the beam is generated. The peak representing coincidences between the FP and the reaction-product detector is clearly evident at ~ 500 ns. The slope of the background in the unshaded single-hit TDC spectrum is proportional to the post-bremsstrahlung electron rate and also to the magnitude of the stolen-coincidence correction. As expected, no slope is evident in the background in the shaded multi-hit TDC spectrum as coincidences may not be stolen. (For interpretation of the references to color in this figure caption, the reader is referred to the web version of this article.)

As previously mentioned, the multi-hit TDC with which the FP has been upgraded has been programmed to accept the first 4 stop signals presented to it in conjunction with the trigger and the programmable acceptance window. In this manner, the stolen-coincidence effect is greatly reduced as up to 3 accidental post-bremsstrahlung electrons can be registered in the multi-hit TDC before the prompt electron without stealing it. Thus, a large correction to the number of tagged events registered by the FP array is avoided, increasing the precision of the overall normalization (Fig. 6).

The causes of ghost events, missed stops, stolen coincidences, and deadtime in the FP scalers and TDCs are all included in the FP simulation [4] which can therefore be used to determine suitable correction factors.

4. Results

Fig. 7 presents a comparison between the absolute differential cross-sections for elastic photon scattering from ^{12}C at a lab angle

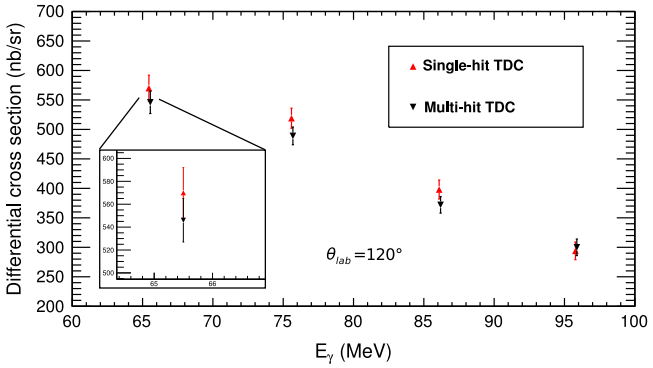

Fig. 7. Absolute differential cross-section data for elastic photon scattering from ^{12}C at a lab angle of 120° obtained simultaneously using both single-hit (upright red triangles) and multi-hit (inverted black triangles) TDCs. The single-hit TDC data have been corrected according to Ref. [4]. Statistical uncertainties only are shown. See text for details. (For interpretation of the references to color in this figure caption, the reader is referred to the web version of this paper.)

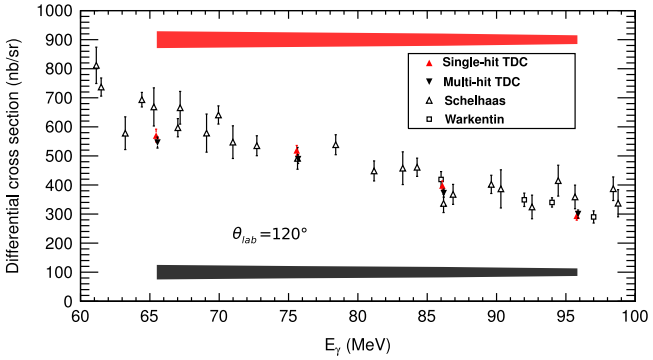

Fig. 8. Absolute differential cross-section data for elastic photon scattering from ^{12}C at a lab angle of 120° obtained simultaneously using both single-hit (upright red triangles) and multi-hit (inverted black triangles) TDCs compared to published data. The single-hit TDC data have been corrected according to Ref. [4]. Statistical uncertainties only are shown. Systematic uncertainty bands for the present measurement are presented at the top (corrected single-hit TDC data) and bottom (multi-hit TDC data) of the figure. See text for details. (For interpretation of the references to color in this figure caption, the reader is referred to the web version of this paper.)

of 120° recently obtained at the TPF at the MAX IV Laboratory using both single-hit (upright red triangles) and multi-hit TDCs (inverted black triangles) simultaneously. The single-hit TDC data have been corrected for stolen coincidences according to Ref. [4]. Error bars reflect statistical uncertainties only. The agreement between the two data sets is satisfactory, thereby confirming our understanding of the stolen-coincidence correction to the data.

Fig. 8 presents a comparison between the absolute differential cross-section data for elastic photon scattering from ^{12}C at a lab angle of 120° recently obtained at the TPF at the MAX IV Laboratory and the existing data published by Schelhaas et al. [14] (open upright triangles) and Warkentin et al. [15] (open squares). Error bars reflect statistical uncertainties only. Systematic uncertainty bands for the present measurement are presented at the top (red, single-hit TDC data) and bottom (gray, multi-hit TDC data) of the figure. The agreement between the data sets is very good thereby confirming our understanding of the absolute normalization.

5. Summary

In this paper, the Monte Carlo simulation [4] of the MAX IV tagger focal-plane electronics has been tested by comparing results obtained using both single- and multi-hit TDCs. Good agreement between these data sets has been demonstrated, and the measured absolute cross-sections also agree with previous experiments. We conclude that the behavior of the detector system is thoroughly understood and that the Monte Carlo simulation incorporates it correctly.

Acknowledgments

This project was supported by the US National Science Foundation Grant no. 0855569, the UK Science and Technology Facilities Council, as well as The Swedish Research Council, the Crafoord Foundation, and the Royal Physiographic Society in Lund. The authors gratefully acknowledge the Data Management and Software Centre, a Danish Contribution to the European Spallation Source ESS AB, for generously providing access to their computations cluster. We also thank J.C. McGeorge for useful discussions.

References

[1] J.-O. Adler, M. Boland, J. Brudvik, K. Fissum, K. Hansen, L. Isaksson, P. Lilja, L.-J. Lindgren, M. Lundin, B. Nilsson, D. Pugachov, A. Sandell, B. Schröder, V. Avdeichikov, P. Golubev, B. Jakobsson, J.R.M. Annand, K. Livingston, R. Igarashi, L. Myers, A. Nathan, W.J. Briscoe, G. Feldman, M. Kovash, D. Branford, K. Föhl, P. Grabmayr, V. Takau, G. O'Rielly, D. Burdeynyi, V. Ganenko, V. Morochovskyi, G. Vashchenko, Nuclear Instruments and Methods in Physics Research Section A 715 (2013) 1.
[2] ⟨https://www.maxlab.lu.se/node/1090⟩.
[3] ⟨https://www.maxlab.lu.se⟩.
[4] L.S. Myers, G. Feldman, K.G. Fissum, L. Isaksson, M.A. Kovash, A.M. Nathan, R. E. Pywell, B. Schröder, Nuclear Instruments and Methods in Physics Research Section A 729 (2013) 707.
[5] L.S. Myers et al., Physical Review C [nucl-ex], (2014) arXiv:1401.4028.
[6] J.M. Vogt, R.E. Pywell, D.M. Skopik, E.L. Hallin, J.C. Bergstrom, H.S. Caplan, K. I. Blomqvist, W. Del Bianco, J.W. Jury, Nuclear Instruments and Methods in Physics Research Section A 324 (1993) 198.
[7] Annual Report 1994, Saskatchewan Accelerator Laboratory, pp. 21–23.
[8] Annual Report 1995, Saskatchewan Accelerator Laboratory, pp. 27–29.
[9] See for example, J.-O. Adler, B.-E. Andersson, K.I. Blomqvist, B. Forkman, K. Hansen, L. Isaksson, K. Lindgren, D. Nilsson, A. Sandell, B. Schröder, K. Ziakas, Nuclear Instruments and Methods in Physics Research Section A 294 (1990) 15.
[10] See for example, J.-O. Adler, B.-E. Andersson, K.I. Blomqvist, K.G. Fissum, K. Hansen, L. Isaksson, B. Nilsson, D. Nilsson, H. Ruijter, A. Sandell, B. Schröder, D.A. Sims, Nuclear Instruments and Methods in Physics Research Section A 388 (1997) 17.
[11] L.-J. Lindgren, Nuclear Instruments and Methods in Physics Research Section A 492 (2002) 299.
[12] R.O. Owens, Nuclear Instruments and Methods in Physics Research Section A 288 (1990) 574.
[13] L. Van Hoorebeke, D. Ryckbosch, C. Van den Abeele, R. Van de Vyver, J. Dias, F. De Smet, B. Schröder, D. Nilsson, Nuclear Instruments and Methods in Physics Research Section A 321 (1992) 230.
[14] K.P. Schelhaas, J.M. Henneberg, N. Wieloch-Laufenberg, U. Zurmühl, B. Ziegler, M. Schumacher, F. Wolf, Nuclear Physics A 506 (1990) 307.
[15] B.J. Warkentin, D.L. Hornidge, R. Igarashi, J.C. Bergstrom, E.L. Hallin, N.R. Kolb, R.E. Pywell, D.M. Skopik, J.M. Vogt, G. Feldman, Physical Review C 64 (2001) 014603.

Compton scattering from ^{12}C using tagged photons in the energy range 65–115 MeV

L. S. Myers,[1,*] K. Shoniyozov,[2] M. F. Preston,[3] M. D. Anderson,[4] J. R. M. Annand,[4] M. Boselli,[4,†] W. J. Briscoe,[5] J. Brudvik,[6] J. I. Capone,[5,‡] G. Feldman,[5] K. G. Fissum,[3,§] K. Hansen,[6] S. S. Henshaw,[7,‖] L. Isaksson,[6] R. Jebali,[4] M. A. Kovash,[2] K. Lewis,[5,¶] M. Lundin,[6] I. J. D. MacGregor,[4] D. G. Middleton,[8,#] D. E. Mittelberger,[5,**] M. Murray,[4] A. M. Nathan,[1] S. Nutbeam,[4] G. V. O'Rielly,[9] B. Schröder,[3,6] B. Seitz,[4] S. C. Stave,[7,††] and H. R. Weller[7]
(The COMPTON@MAX-lab Collaboration)
[1]*Department of Physics, University of Illinois at Urbana-Champaign, Urbana, Illinois 61801, USA*
[2]*Department of Physics and Astronomy, University of Kentucky, Lexington, Kentucky 40506, USA*
[3]*Department of Physics, Lund University, SE-221 00 Lund, Sweden*
[4]*School of Physics and Astronomy, University of Glasgow, Glasgow G12 8QQ, Scotland, UK*
[5]*Department of Physics, The George Washington University, Washington, DC 20052, USA*
[6]*MAX IV Laboratory, Lund University, SE-221 00 Lund, Sweden*
[7]*Department of Physics, Duke University, Durham, North Carolina 27708, USA*
[8]*Kepler Centre for Astro and Particle Physics, Physikalisches Institut, Universität Tübingen, D-72076 Tübingen, Germany*
[9]*Department of Physics, University of Massachusetts Dartmouth, Dartmouth, Massachusetts 02747, USA*
(Received 17 January 2014; published 10 March 2014)

Elastic scattering of photons from ^{12}C has been investigated using quasimonoenergetic tagged photons with energies in the range 65–115 MeV at laboratory angles of 60°, 120°, and 150° at the Tagged-Photon Facility at the MAX IV Laboratory in Lund, Sweden. A phenomenological model was employed to provide an estimate of the sensitivity of the ^{12}C$(\gamma,\gamma)^{12}$C cross section to the bound-nucleon polarizabilities.

DOI: 10.1103/PhysRevC.89.035202 PACS number(s): 25.20.Dc, 24.70.+s

I. INTRODUCTION

Much effort has been devoted to studying α and β, the electromagnetic polarizabilities of the proton and neutron. These polarizabilities represent the first-order responses of the internal structure of the nucleon to an external electric or magnetic field. The majority of nucleon-polarizability measurements have utilized the process of nuclear Compton scattering. A review of these experiments can be found in Ref. [1].

The most recent global fit [1] to all the data up to 170 MeV has yielded polarizabilities for the proton in units of 10^{-4} fm^3 of

$$\begin{aligned}\alpha_p &= 10.7 \pm 0.3_{\text{stat}} \pm 0.2_{\text{BSR}} \pm 0.8_{\text{th}},\\ \beta_p &= 3.1 \mp 0.3_{\text{stat}} \pm 0.2_{\text{BSR}} \pm 0.8_{\text{th}},\end{aligned} \tag{1}$$

where the first uncertainty is statistical, the second is due to uncertainties in the Baldin sum rule (BSR), and the third is due to theoretical uncertainty. The Baldin sum rule is given by [2]

$$\alpha + \beta = \frac{1}{2\pi^2}\int_{\omega_{\text{th}}}^{\infty}\frac{\sigma_\gamma(\omega)d\omega}{\omega^2}, \tag{2}$$

where $\sigma_\gamma(\omega)$ is the total photoabsorption cross section for the nucleon and ω_{th} is the threshold energy for pion photoproduction. These results were obtained under the constraint of the present-day evaluation [3] of the BSR for the proton which is

$$\alpha_p + \beta_p = 13.8 \pm 0.4. \tag{3}$$

Similarly, the neutron polarizabilities have been extracted from measurements of ^{2}H$(\gamma,\gamma)^2$H. They have been determined to be

$$\begin{aligned}\alpha_n &= 11.1 \pm 1.8_{\text{stat}} \pm 0.4_{\text{BSR}} \pm 0.8_{\text{th}},\\ \beta_n &= 4.1 \mp 1.8_{\text{stat}} \pm 0.4_{\text{BSR}} \pm 0.8_{\text{th}},\end{aligned} \tag{4}$$

preserving the BSR for the neutron [4]

$$\alpha_n + \beta_n = 15.2 \pm 0.4. \tag{5}$$

It is also reasonable to ask whether the nucleon polarizabilities are modified when the proton or neutron is bound in a nucleus and, if so, to what degree. A multitude of Compton-scattering experiments have been carried out with a variety of light nuclei (see Table I) for the purpose of determining the bound-nucleon polarizabilities (α_{eff} and β_{eff}) given by

$$\alpha_{\text{eff}} = \alpha_N + \Delta\alpha, \quad \beta_{\text{eff}} = \beta_N + \Delta\beta, \tag{6}$$

where α_N and β_N are the nucleon-averaged free polarizabilities and $\Delta\alpha$ and $\Delta\beta$ represent the nuclear modifications [13] which can be extracted from the scattering data.

*Present address: Thomas Jefferson National Accelerator Facility, Newport News, Virginia 23606, USA.
†Present address: European Center for Theoretical studies in Nuclear Physics and Related Areas, Strada delle Tabarelle 286, I-38123 Villazzano, Trento, Italy.
‡Present address: Department of Physics, University of Maryland, College Park, Maryland 20742, USA.
§Corresponding author: kevin.fissum@nuclear.lu.se
‖Present address: National Security Technologies, Andrews AFB, Maryland 20762, USA.
¶Present Address: Trident Training Facility, Navy Submarine Base, Bangor, Washington 98383, USA.
#Present address: Institut für Kernphysik, University of Mainz, D-55128 Mainz, Germany.
**Present Address: LOASIS Program, Lawrence Berkeley National Lab, Berkeley, California 94720, USA.
††Present address: Pacific Northwest National Laboratory, Richland, Washington 99352, USA.

TABLE I. Summary of nuclei studied using Compton scattering below the energy threshold for pion production.

Nucleus	Reference
^{4}He	[5], [6], [7]
^{6}Li	[8]
^{12}C	[9], [10], [11], [12], [13]
^{16}O	[7], [8], [11], [12], [14], [15]
^{40}Ca	[7], [9]

These data sets have been analyzed using a model that parameterizes the Compton-scattering amplitude in terms of the photoabsorption cross section, its multipole decomposition and the bound-nucleon polarizabilities. The results typically produce a value for $\alpha_{\rm eff} + \beta_{\rm eff}$ that is in agreement with the free-nucleon sum rules given above [16]. However, although the sum is unchanged, several measurements [6,15] have reported a significant modification to the electric polarizability ($\Delta\alpha$ approximately -5 to -10) whereas other groups report bound and free polarizabilities that are nearly equal [12]. In this paper we present a substantial new data set for Compton scattering from ^{12}C and report on the extracted values of the bound-nucleon polarizabilities.

II. PHENOMENOLOGICAL MODEL

A phenomenological model has been used to evaluate the sensitivity of the ^{12}C Compton-scattering data to the magnitude of the electromagnetic polarizabilities. This model is based on the work presented in Ref. [9]. The Compton-scattering amplitude can be written [15] in terms of the one- and two-body seagull (SG) amplitudes (which are explicitly dependent on the polarizabilities $\alpha_{\rm eff}$ and $\beta_{\rm eff}$) as

$$R(E,\theta) = R^{\rm GR}(E,\theta) + R^{\rm QD}(E,\theta) + R_1^{\rm SG}(E,\theta) + R_2^{\rm SG}(E,\theta). \tag{7}$$

The first two terms in Eq. (7) are related to the giant resonances ($E1$, $E2$, and $M1$; hereafter referred to as GR) and the quasideuteron (QD) processes, respectively. The amplitudes are given by

$$R^{\rm GR}(E,\theta) = f_{E1}(E)g_{E1}(\theta) + f_{E2}(E)g_{E2}(\theta) + f_{M1}(E)g_{M1}(\theta) + \frac{NZ}{A}r_0[1+\kappa_{\rm GR}]g_{E1}(\theta), \tag{8}$$

and

$$R^{\rm QD}(E,\theta) = \left[f_{\rm QD}(E) + \frac{NZ}{A}r_0\kappa_{\rm QD}\right]F_2(q)g_{E1}(\theta), \tag{9}$$

where the complex forward-scattering amplitudes are denoted by $f_\lambda(E)$ ($\lambda = E1, E2, M1$), the appropriate angular factor is $g_\lambda(\theta)$ (see Ref. [8] for the angular factors), r_0 is the classical nucleon radius, and the enhancement factors $[1+\kappa_{\rm GR}]$ and $\kappa_{\rm QD}$ are the integrals of the GR and QD photoabsorption cross sections in units of the classical dipole sum rule. Since the QD process is modeled as an interaction with a neutron-proton pair, it is modulated by a two-body form factor $F_2(q)$ where q is the momentum transfer.

The seagull amplitudes account for subnucleon and meson-exchange degrees of freedom and are necessary to preserve gauge invariance in the total scattering amplitude. The one-body seagull amplitude is

$$R_1^{\rm SG}(E,\theta) = \left\{\left[-Zr_0 + \left(\frac{E}{\hbar c}\right)^2 A\alpha_{\rm eff}\right]g_{E1}(\theta) + \left[\left(\frac{E}{\hbar c}\right)^2 A\beta_{\rm eff}\right]g_{M1}(\theta)\right\}F_1(q), \tag{10}$$

where the higher-order terms have been omitted. This process is modulated by the one-body form factor $F_1(q)$ which is given by

$$F_1(q) = \frac{4\pi}{q}\int_0^\infty \rho(r)\sin(qr)r\,dr, \tag{11}$$

where $\rho(r)$ is given by the three-parameter Fermi function [17]

$$\rho(r) = \rho_0\frac{1+\frac{wr^2}{c^2}}{1+e^{\frac{r-c}{z}}}, \tag{12}$$

with $w = -0.149$, $c = 2.355$ fm, $z = 0.522$ fm, and the form factor is normalized so that $F_1(0) = 1$.

The two-body seagull amplitude is

$$R_2^{\rm SG}(E,\theta) = \left\{\left[-\frac{NZ}{A}\kappa r_0 + \left(\frac{E}{\hbar c}\right)^2 A\alpha_{\rm ex}\right]g_{E1}(\theta) + \left[\left(\frac{E}{\hbar c}\right)^2 A\beta_{\rm ex}\right]g_{M1}(\theta)\right\}F_2(q), \tag{13}$$

where the exchange polarizabilities are denoted by $\alpha_{\rm ex}$ and $\beta_{\rm ex}$, $\kappa = \kappa_{\rm GR} + \kappa_{\rm QD}$, and the higher-order terms have been dropped. The two-body form factor is chosen by convention as $F_2(q) = [F_1(q/2)]^2$.

The parametrization of the $E1$ resonance is taken from Ref. [9] where the angle-averaged differential cross section was used to extract the $E1$ resonance below 40 MeV. The $E2$ strength between 25 and 35 MeV [12] and an $M1$ resonance [18] were also included. These included resonances are listed in Table II.

Levinger's modified quasideuteron model [19] and a damped Lorentzian lineshape were used to define a piecewise function to parametrize the QD process [Eq. (14)]. This parametrization was fit to the existing total photoabsorption cross-section data [20] above 50 MeV in order to establish the normalization. The QD scattering cross section was taken

TABLE II. $E2$, $M1$, and QD parameters.

Resonance	E_λ (MeV)	σ_λ (mb)	Γ_λ (MeV)
$E2$	26.0	1.8	0.50
	32.3	1.2	2.60
$M1$	15.1	29 780	37×10^{-6}
QD	40	1.0	100

to be

$$\sigma_{\rm QD}(E) = \begin{cases} \frac{1}{2}\left[1+\tanh\frac{E-E_t}{\Delta E}\right]\mathcal{L}_{\rm QD}(E), & E < 50\ \text{MeV} \\ Le^{-D/E}\left[\frac{NZ}{A}\right]\sigma_D(E), & E > 50\ \text{MeV}, \end{cases} \tag{14}$$

where $\sigma_D(E)$ is the deuteron photoabsorption cross section and the parameters $L = 5.0$ and $D = 5.4$ were determined from the fit to the data. The Lorentzian $\mathcal{L}_{\rm QD}(E)$ has the parameters $E_{\rm QD}$, $\Gamma_{\rm QD}$, and $\sigma_{\rm QD}$ given in Table II, with $E_t = 40$ MeV and $\Delta E = 10$ MeV. Since the analysis of Warkentin *et al.* [13] indicated that the extraction of $\alpha_{\rm eff}$ and $\beta_{\rm eff}$ depends only slightly on the parametrization of the QD amplitude, only the above parametrization will be used in this analysis.

III. EXPERIMENT

The experiment was performed at the Tagged-Photon Facility [21,22] located at the MAX IV Laboratory [23] in Lund, Sweden. A pulse-stretched electron beam [24] with nominal energies of 144 MeV and 165 MeV, a current of 15 nA, and a duty factor of 45% was used to produce quasi-monoenergetic photons in the energy range 65–115 MeV via the bremsstrahlung-tagging technique [25,26]. An overview of the experimental layout is shown in Fig. 1.

The size of the photon beam was defined by a tapered tungsten-alloy primary collimator of 19 mm nominal diameter. The primary collimator was followed by a dipole magnet and a postcollimator which were used to remove any charged particles produced in the primary collimator. The beam spot at the target location was approximately 60 mm in diameter.

The tagging efficiency [26] is the ratio of the number of tagged photons which struck the target to the number of postbremsstrahlung electrons which were registered by the associated focal-plane channel. It was measured absolutely during the experiment startup with three large-volume NaI(Tl) photon spectrometers placed directly in the beam (see below) and it was monitored during the experiment itself on a daily basis using a lead-glass photon detector. The tagging efficiency was determined to be $(44 \pm 1)\%$ throughout the experiment.

A graphite block 5.22 cm thick was used as a target. The density of the target was measured to be (1.83 ± 0.02) g/cm^3. The target was positioned such that the photon beam was perpendicular to the face of the target resulting in a target thickness of $(4.80 \pm 0.07) \times 10^{23}$ nuclei/cm^2. The average loss of incident photon-beam flux due to absorption in the target was approximately 7%.

Three large-volume, segmented NaI(Tl) detectors labeled BUNI [27], CATS [28], and DIANA [29] in Fig. 1 were used to detect the Compton-scattered photons. The detectors were located at laboratory angles of 60°, 120°, and 150°. These detectors were each composed of a single, large NaI(Tl) crystal surrounded by optically isolated, annular NaI(Tl) segments. The detectors have an energy resolution of better than 2% at energies near 100 MeV. Such resolution is necessary to unambiguously separate elastically scattered photons from those originating from the breakup of deuterium, a parallel and ongoing experimental effort to be reported upon in the near future.

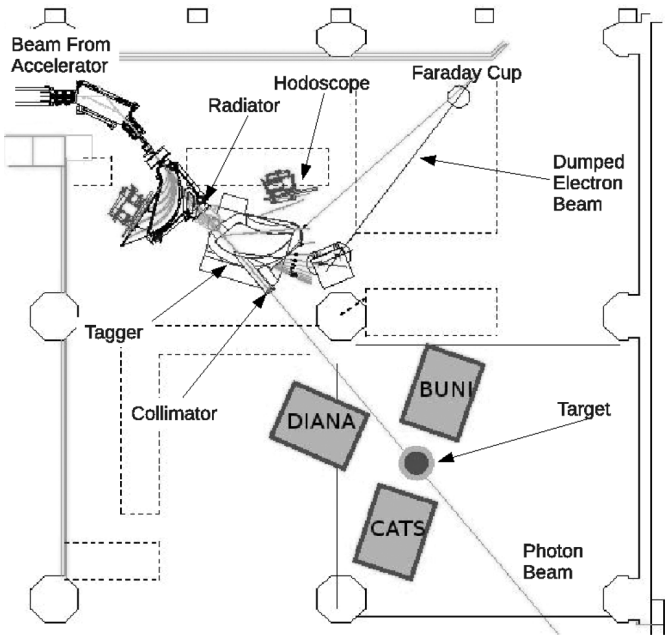

FIG. 1. The layout of the experimental area showing the location of the focal-plane hodoscope, ^{12}C target, and NaI(Tl) detectors labeled DIANA, BUNI, and CATS.

IV. DATA ANALYSIS

A. Yield extraction

The signals from each detector were passed to analog-to-digital converters (ADCs) and time-to-digital converters (TDCs) and the data recorded on an event-by-event basis. The comprehensive dataset presented in this paper was acquired over a five-year period from 2007 to 2012. During this time, the single-hit TDCs used to instrument the tagger focal plane were complemented with multihit TDCs. Data obtained using both types of TDCs are presented here.[1] The ADCs allowed reconstruction of the scattered-photon energies, while the TDCs enabled coincident timing between the NaI(Tl) detectors and the focal-plane hodoscope. The energy calibration of each detector was determined by placing them directly into the photon beam and observing their response as a function of tagged-photon energy. A typical measured in-beam lineshape together with a GEANT4 simulation [32] of the response function of the detector fit to the data is shown in Fig. 2.

Large backgrounds arose when the detectors were moved to the various scattering angles and the beam intensity was increased from 10–100 Hz (for in-beam runs) to 1–4 MHz. Untagged bremsstrahlung photons (related to the beam intensity) and cosmic rays (constant) were the dominant sources of background. An energy cut that accepted only events in the tagged-energy range enabled the prompt peak

[1]The interested reader is directed to Refs. [30,31] for a detailed discussion and comparison of the results obtained using the two different types of TDCs.

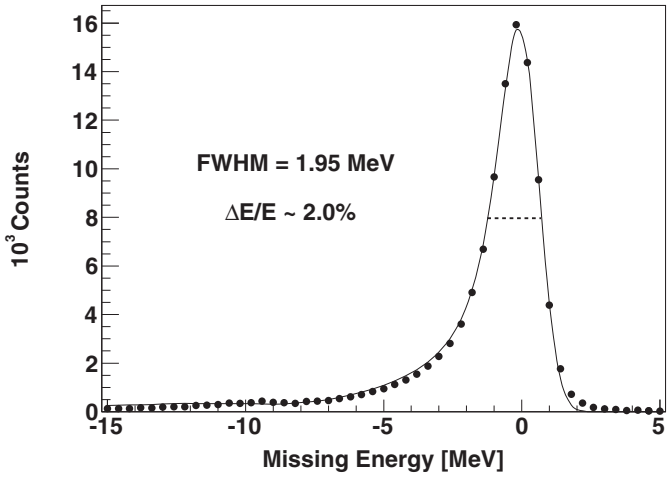

FIG. 2. Typical in-beam detector response to incident photons as a function of missing energy. The curve is the simulated GEANT4 detector response fit to the data.

[representing coincidences between electrons in the focal-plane hodoscope and events in the NaI(Tl) detectors] to be identified in the focal-plane TDC spectra (see Fig. 3). For each NaI(Tl) detector, events occurring within the prompt peak were selected and a prompt missing-energy (ME) spectrum was filled. ME was defined as the difference between the detected photon energy and the expected photon energy based upon the tagged-electron energy. A second cut was placed on an accidental (or random) timing region and an accidental ME spectrum was filled. This process was carried out for each focal-plane channel.

A net sum ME spectrum for each focal-plane channel was generated by removing both the cosmic-ray and untagged-photon backgrounds. Due to the complex nature of the time structure that exists in the focal-plane TDC spectrum, this process was carried out in two steps. First, the cosmic-ray contribution was subtracted from both the prompt and accidental ME spectra by normalizing these spectra in the

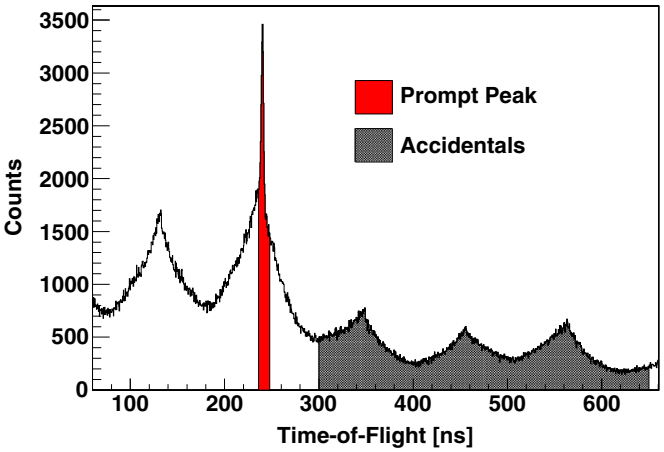

FIG. 3. (Color online) The focal-plane TDC spectrum for the scattering data. The prompt (red) and the accidental (gray) windows are indicated.

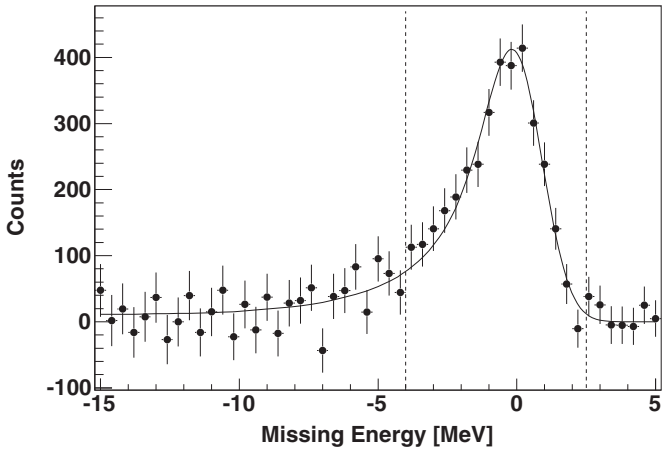

FIG. 4. A typical missing-energy spectrum for a focal-plane bin obtained in one of the scattering configurations, with both cosmics and accidentals removed. The solid line is the fit of the GEANT4 lineshape to the data. The dashed lines indicate the ROI used to determine the yield of Compton-scattered photons (see text).

energy region above the electron-beam energy. Next, the cosmic-subtracted accidentals were removed from the cosmic-subtracted prompts by normalizing the two spectra in the energy range above the tagged-photon energy corresponding to the particular focal-plane channel but below the electron-beam energy. The focal plane was divided into four energy bins, each approximately 9 MeV wide. The background-corrected ME spectrum for each tagged channel in a particular energy bin was then summed to create a ME spectrum for that bin, such as the one shown in Fig. 4.

A GEANT4 simulation was employed to determine the total yield in the elastic-scattering peak and also to quantify any corrections due to finite geometrical effects. The simulation output was first determined for the case of a NaI(Tl) detector positioned directly in the low-intensity photon beam ($\theta = 0^\circ$) as shown in Fig. 2. This intrinsic simulation was then smeared with a Gaussian function to phenomenologically account for the individual characteristics of each NaI(Tl) detector that are difficult to model in GEANT4. The simulated detector response, with the smearing determined as above, was then fit to the scattering data over the region of interest (ROI) indicated by the vertical dashed lines shown in Fig. 4. The fit GEANT4 lineshape was then used to correct for the detection efficiency of the NaI(Tl) detector in the ROI. This efficiency accounts for events that deposit some energy outside the ROI in the detector. Additionally, the correction factor for photons absorbed by the target and the correction to the detector acceptance due to the finite geometry of the experimental setup were obtained from this simulation.

B. Normalization

The scattering-photon yield was then normalized to the number of photons incident on the target and corrected for rate-dependent factors. The number of photons incident on the target was determined from the number of postbremsstrahlung electrons detected in each focal-plane channel and the

TABLE III. Systematic uncertainties.

Type	Variable	Value
Scale	Tagging efficiency	∼1%
	Target thickness	∼1%
	Missed trues	∼1%
	Ghost events	∼2%
Angular	Detector acceptance	3%–4%
Point-to-point	Stolen Trues	2%–4%
Total		5%–7%

measured tagging efficiency. The rate-dependent corrections included "stolen" trues [33], "missed" trues, and "ghost" events [34]. A stolen true arose when a random electron was detected in the focal-plane channel prior to the electron corresponding to the tagged photon. This correction was only applied to the single-hit TDC data. It was determined using the method outlined in Ref. [35] and was typically 20%–45%. Missed trues resulted from dead-time effects in the focal-plane instrumentation electronics. Ghost events were an artifact of the physical overlap of the focal-plane counters. The missed trues and ghost corrections were determined using a Monte Carlo simulation of the focal-plane electronics and amounted to approximately 5% and 1%, respectively.[2]

C. Systematic uncertainties

The systematic uncertainties in this experiment were grouped into three types. The first was an overall scale systematic uncertainty that affected the data obtained at all angles and energies equally. This uncertainty arose from normalization factors such as the tagging efficiency. The second type of uncertainty varied only with angle but not energy and was due to the acceptance of the individual NaI(Tl) detectors. This uncertainty had two origins: (1) the distance and aperture size of the detector in its scattering location; and (2) the effect of placing cuts on the data during analysis. Finally, certain uncertainties were strongly dependent on kinematics and varied with both energy and angle such as the stolen-trues correction. The dominant sources of systematic uncertainties are listed in Table III along with typical values. The systematic uncertainties were combined in quadrature to obtain the overall systematic uncertainty.

D. Cross sections

The ^{12}C elastic scattering cross sections measured in this experiment are presented in Table IV. The results are also shown in Fig. 5, along with the results from [10–13] above 55 MeV. The new data are in excellent agreement with the results from Schelhaas *et al.* [10] and Warkentin *et al.* [13].

[2]The interested reader is directed to Ref. [30] for a detailed discussion of the focal-plane simulation.

TABLE IV. Measured cross sections for ^{12}C(γ,γ) at the laboratory angles listed. The type of TDC used to record coincidences is indicated. The first uncertainty is statistical and the second uncertainty is total systematic.

E_γ (MeV)	$\frac{d\sigma}{d\Omega}(60^\circ)$ (nb/sr)	$\frac{d\sigma}{d\Omega}(120^\circ)$ (nb/sr)	$\frac{d\sigma}{d\Omega}(150^\circ)$ (nb/sr)
	Single-hit TDCs, $E_{\rm beam} = 144$ MeV		
69.6		$618 \pm 24 \pm 42$	$599 \pm 28 \pm 32$
77.9		$502 \pm 19 \pm 32$	$496 \pm 24 \pm 26$
86.1		$423 \pm 17 \pm 26$	$354 \pm 21 \pm 18$
93.4		$354 \pm 16 \pm 23$	$298 \pm 23 \pm 16$
	Single-hit TDCs, $E_{\rm beam} = 165$ MeV		
85.8	$439 \pm 29 \pm 29$	$519 \pm 21 \pm 34$	$389 \pm 21 \pm 22$
94.8	$312 \pm 24 \pm 19$	$358 \pm 16 \pm 23$	$284 \pm 17 \pm 18$
103.8	$261 \pm 21 \pm 17$	$309 \pm 15 \pm 20$	$230 \pm 14 \pm 13$
112.1	$233 \pm 19 \pm 16$	$223 \pm 12 \pm 15$	$156 \pm 13 \pm 9$
	Multi-hit TDCs, $E_{\rm beam} = 165$ MeV		
87.3	$389 \pm 14 \pm 16$	$365 \pm 11 \pm 14$	$381 \pm 11 \pm 14$
96.3	$324 \pm 13 \pm 13$	$312 \pm 10 \pm 13$	$312 \pm 10 \pm 13$
104.7	$212 \pm 11 \pm 11$	$256 \pm 8 \pm 11$	$263 \pm 8 \pm 13$
112.9	$209 \pm 9 \pm 10$	$213 \pm 7 \pm 10$	$166 \pm 7 \pm 8$
	Single-hit TDCs, $E_{\rm beam} = 165$ MeV		
65.5	$562 \pm 42 \pm 35$	$570 \pm 22 \pm 29$	
75.7	$470 \pm 28 \pm 29$	$519 \pm 17 \pm 25$	
86.2	$392 \pm 27 \pm 22$	$398 \pm 16 \pm 18$	
95.9	$281 \pm 23 \pm 14$	$294 \pm 15 \pm 13$	
	Multi-hit TDCs, $E_{\rm beam} = 165$ MeV		
65.5	$517 \pm 34 \pm 22$	$546 \pm 19 \pm 24$	
75.7	$432 \pm 23 \pm 18$	$489 \pm 15 \pm 20$	
86.2	$368 \pm 22 \pm 16$	$372 \pm 14 \pm 15$	
95.9	$250 \pm 20 \pm 10$	$300 \pm 14 \pm 12$	

V. RESULTS

The most recent interpretations of ^{12}C(γ,γ) cross-section data [12,13] utilize multiple Lorentzian lineshapes to construct the $E1$ scattering amplitude. However, in our analysis, the phenomenological model is unable to fit the low-energy data of Wright *et al.* [9] using these lineshapes (see Fig. 6). In an attempt to incorporate all the published data, we have elected to use the analysis procedure detailed in Ref. [9] where the $E1$ resonance is deduced from the low-energy ($\leqslant$40 MeV), angle-averaged Compton-scattering cross section, and the QD scattering amplitude is given by Eq. (14). The $E2$ and $M1$ resonances below 40 MeV are included for completeness but have little effect on the results.

As suggested by Wright *et al.* [9] and reinforced by Warkentin *et al.* [13], we also allowed for the possibility of $E2$ strength above 50 MeV. A third $E2$ resonance was added to the phenomenological model (with an equivalent lineshape subtracted from the QD parametrization so as to not affect the total photoabsorption cross section [14]) with a width of 30 MeV. The best fits to the data were achieved with an $E2$ resonance energy of approximately 90 MeV and a peak strength of approximately 0.2 mb. These values are consistent with the resonance assumed by Warkentin *et al.* The

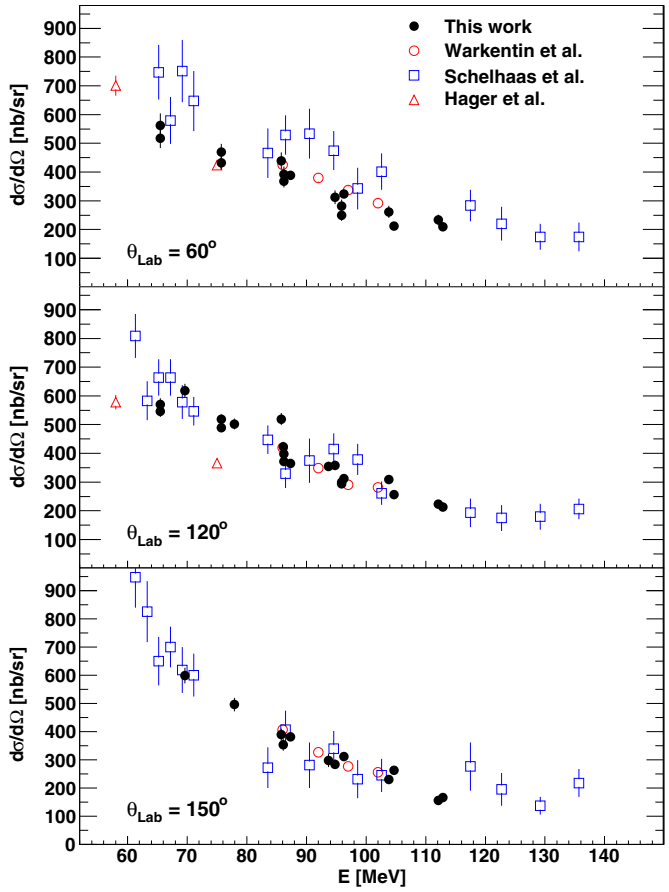

FIG. 5. (Color online) Measurements of the ^{12}C Compton-scattering cross section from previous experiments compared to the results from the current experiment. Statistical uncertainties are shown.

addition of this $E2$ resonance reduced χ^2 by approximately 30% compared to an identical fit without the additional $E2$ strength.

With the above parametrization, we were able to fit the entire world data set (excluding the data from Häger *et al.* [12]) below 150 MeV with the phenomenological model. Four different approaches were used involving different combinations of the BSR, the bound-nucleon polarizabilities ($\alpha_{\rm eff}$ and $\beta_{\rm eff}$), and the exchange polarizabilities ($\alpha_{\rm ex}$ and $\beta_{\rm ex}$) (see Table V). In approach (1), $\alpha_{\rm eff}$ and $\beta_{\rm eff}$ were varied under the BSR constraint while $\alpha_{\rm ex} = \beta_{\rm ex} = 0$ were fixed. In approach (2), the effective polarizabilities were fixed while the exchange polarizabilities were varied. In approach (3), $\alpha_{\rm ex} = \beta_{\rm ex} = 0$ were once again fixed, and $\alpha_{\rm eff}$ and $\beta_{\rm eff}$ were varied without the BSR constraint. In approach (4), using only the BSR constraint, all the polarizabilities were allowed to vary in order to minimize the χ^2/DOF. In all four cases, the additional $E2$ resonance was fixed at $E_{\rm res} = 89$ MeV, $\sigma_{\rm res} = 0.22$ mb, and $\Gamma_{\rm res} = 30$ MeV) as minor variations in the resonance parameters had a negligible effect on the results. Together with the $E1$ parametrization developed by Wright *et al.* [9], this analysis presents a consistent framework for fitting the scattering data from photon energies below the giant dipole resonance to energies near the threshold for pion

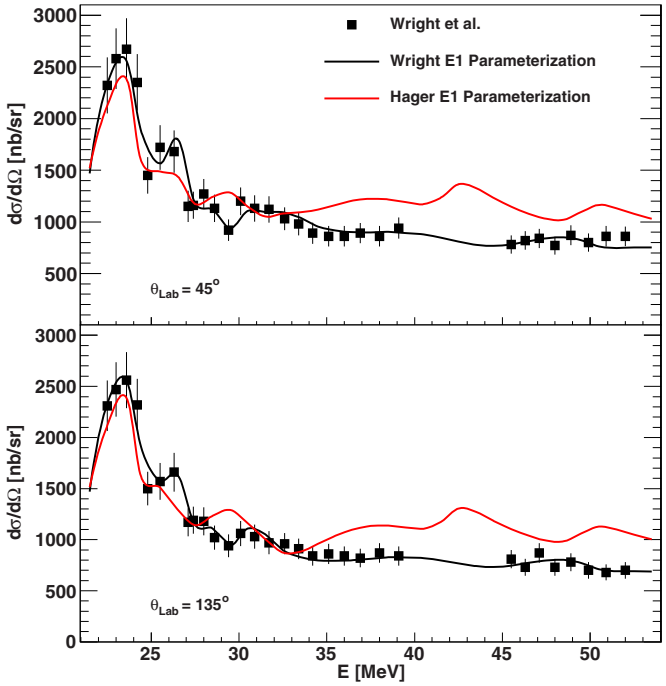

FIG. 6. (Color online) Comparison of the fit to the Wright *et al.* data [9] using the $E1$ resonance parametrization suggested by the author (black) as well as that of Häger *et al.* [12] (red).

production. The results are summarized in Table V (quantities listed without uncertainties were held fixed during the fitting) and are shown in Fig. 7.

The extracted value of $\alpha_{\rm eff}$ varied over the range 3–11. Additionally, the exchange polarizabilities were quite large depending on the values used for $\alpha_{\rm eff}$ and $\beta_{\rm eff}$. Thus, it is clear that this model for Compton scattering is unable to differentiate between in-medium modifications to the free-nucleon polarizabilities and the effects of the two-body exchange polarizabilities. The results of our analysis indicate that the net electric polarizability of the bound nucleon ($\alpha_{\rm eff} + \alpha_{\rm ex}$) is significantly reduced from its free value and that the magnetic polarizability is much larger than its free value. This is in direct opposition to the results reported by Häger *et al.* [12] where the observed bound-nucleon polarizabilities were in agreement with the free values. The sources of this discrepancy are the reported cross sections, especially at the backward scattering angles (see Fig. 5), and the choice of the model parametrization. Fitting the Häger *et al.* [12] data alone with the model developed in this paper (with $\alpha_{\rm ex} = \beta_{\rm ex} = 0$ fixed) produces a value of $\alpha_{\rm eff} = 8.2 \pm 0.5$ and $\beta_{\rm eff} = 6.3 \mp 0.5$. Thus, the

TABLE V. Extracted values of the effective and exchange polarizabilities subject to the constraints outlined in the text.

Approach	$\alpha_{\rm eff} + \beta_{\rm eff}$	$\alpha_{\rm eff}$	$\beta_{\rm eff}$	$\alpha_{\rm ex}$	$\beta_{\rm ex}$
(1)	14.5	3.4(0.2)	11.1(0.2)	0	0
(2)	14.5	10.9	3.6	− 3.9(0.2)	6.4(0.2)
(3)	18.3(0.3)	4.9(0.2)	13.4(0.2)	0	0
(4)	14.5	3.6(1.1)	10.9(1.1)	1.3(0.8)	2.1(0.7)

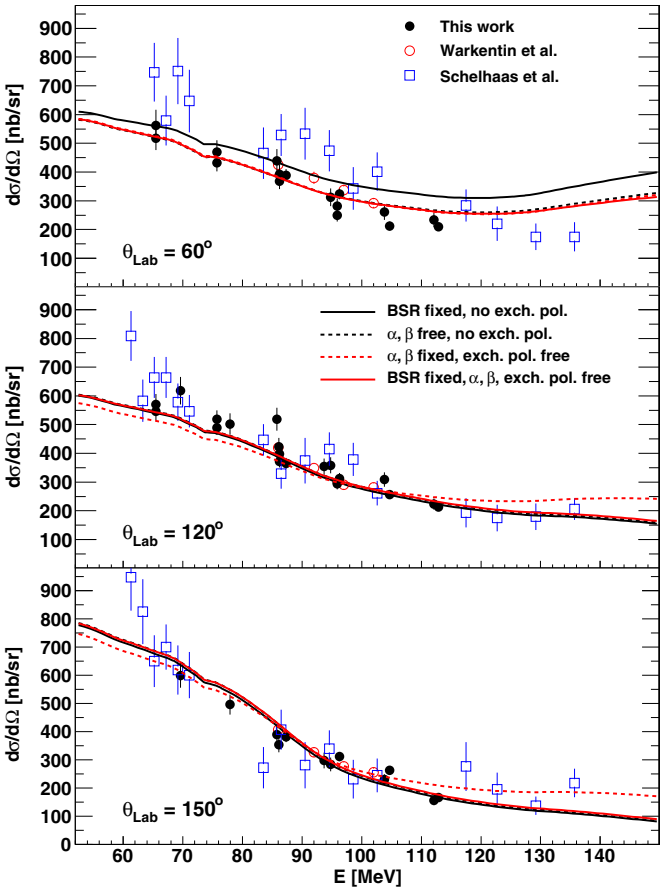

FIG. 7. (Color online) Comparison of the fits to the data obtained by varying $\alpha_{\mathrm{eff,ex}}$ and $\beta_{\mathrm{eff,ex}}$ as described in the text. The uncertainties shown are the statistical and systematic uncertainties added in quadrature.

choice of the resonance parametrization explains part of the discrepancy. We note that the Häger *et al.* [12] cross-section data, especially at the backward angles, are much smaller than those reported in most other experiments [10,11,13]. The effect of a smaller cross section is an increase in the difference $\alpha_{\mathrm{eff}} - \beta_{\mathrm{eff}}$ which, in turn, produces values for the bound polarizabilities much closer to their free values. Based on our data and the analysis presented here, we assert that either the bound-nucleon polarizabilities differ considerably from the free-nucleon values or there are substantial contributions of two-body exchange polarizabilities. Both of these statements agree with the conclusions of Feldman *et al.* [15] drawn based upon ^{16}O(γ,γ) data.

VI. CONCLUSIONS

In this work, we present a new measurement of the ^{12}C Compton-scattering cross section for the energy range 65–115 MeV. The results are in good agreement with the previously published results of Schelhaas *et al.* [10], Ludwig *et al.* [11], and Warkentin *et al.* [13]. However, there is a substantial discrepancy with the results reported by Häger *et al.* [12].

The values of the extracted bound-nucleon polarizabilities were found to be strongly dependent on the parametrization of the cross section. The range of extracted α_{eff} was 3–11 depending on whether or not the exchange polarizabilities were included. Based on the results and analysis, there are in-medium effects and/or exchange polarizabilities that must be accounted for in a full calculation of the Compton-scattering process. Unfortunately, the current world-data set does not indicate which of these effects is more important. The data do seem to have a strong preference for additional $E2$ strength located above 50 MeV which could be experimentally determined.

ACKNOWLEDGMENTS

The authors acknowledge the outstanding support of the staff of the MAX IV Laboratory which made this experiment successful. We also gratefully acknowledge the Data Management and Software Centre, a Danish contribution to the European Spallation Source ESS AB, for generously providing access to their computations cluster. The Lund group acknowledges the financial support of the Swedish Research Council, the Knut and Alice Wallenberg Foundation, the Crafoord Foundation, the Swedish Institute, the Wenner-Gren Foundation, and the Royal Swedish Academy of Sciences. This work was sponsored in part by the U.S. Department of Energy under Grants No. DE-FG02-95ER40901, No. DE-FG02-99ER41110, and No. DE-FG02-06ER41422, the US National Science Foundation under Award No. 0853760 and the UK Science and Technology Facilities Council.

[1] H. W. Grießhammer, J. A. McGovern, D. R. Phillips, and G. Feldman, Prog. Part. Nucl. Phys. **67**, 841 (2012).
[2] A. M. Baldin, Nucl. Phys. **18**, 310 (1960).
[3] V. Olmos de León, F. Wissmann, P. Achenbach, J. Ahrens, H.-J. Arends, R. Beck, P. D. Harty, V. Hejny, P. Jennewein, M. Kotulla *et al.*, Eur. Phys. J. A **10**, 207 (2001).
[4] M. I. Levchuk and A. I. L'vov, Nucl. Phys. A **674**, 449 (2000).
[5] D. P. Wells, Ph.D. thesis, University of Illinois at Urbana-Champaign, 1990.
[6] K. Fuhrberg, D. Häger, T. Glebe, B.-E. Andersson, K. Hansen, M. Hütt, B. Nilsson, L. Nilsson, D. Ryckbosch, B. Schröder *et al.*, Nucl. Phys. A **591**, 1 (1995).
[7] S. Proff, C. Pöch, T. Glebe, J.-O. Adler, K. Fissum, K. Hansen, M.-Th. Hütt, O. Kaltschmidt, M. Lundin, B. Nilsson *et al.*, Nucl. Phys. A **646**, 67 (1999).
[8] L. S. Myers, M. W. Ahmed, G. Feldman, S. S. Henshaw, M. A. Kovash, J. M. Mueller, and H. R. Weller, Phys. Rev. C **86**, 044614 (2012).

[9] D. H. Wright, P. T. Debevec, L. J. Morford, and A. M. Nathan, Phys. Rev. C **32**, 1174 (1985).
[10] K. P. Schelhaas, J. M. Henneberg, N. Wieloch-Laufenberg, U. Zurmühl, B. Ziegler, M. Schumacher, and F. Wolf, Nucl. Phys. A **506**, 307 (1990).
[11] M. Ludwig, B.-E. Andersson, A. Baumann, K. I. Blomqvist, K. Fuhrberg, E. Hayward, G. Müller, D. Nilsson, A. Sandell, B. Schröder *et al.*, Phys. Lett. B **274**, 275 (1992).
[12] D. Häger, K. Fuhrberg, T. Glebe, M. Hütt, M. Ludwig, M. Schumacher, B.-E. Andersson, K. Hansen, B. Nilsson, B. Schröder *et al.*, Nucl. Phys. A **595**, 287 (1995).
[13] B. J. Warkentin, D. L. Hornidge, R. Igarashi, J. C. Bergstrom, E. L. Hallin, N. R. Kolb, R. E. Pywell, D. M. Skopik, J. M. Vogt, and G. Feldman, Phys. Rev. C **64**, 014603 (2001).
[14] K. E. Mellendorf, Ph.D. thesis, University of Illinois at Urbana-Champaign, 1993.
[15] G. Feldman, K. E. Mellendorf, R. A. Eisenstein, F. J. Federspiel, G. Garino, R. Igarashi, N. R. Kolb, M. A. Lucas, B. E. MacGibbon, W. K. Mize *et al.*, Phys. Rev. C **54**, R2124(R) (1996).
[16] M.-Th. Hutt, A. I. L'vov, A. I. Milstein, and M. Schumacher, Phys. Rep. **323**, 457 (2000).
[17] C. W. de Jager, H. D. Vries, and C. D. Vries, At. Data Nucl. Data Tables **14**, 479 (1974).
[18] E. Hayward, in *Giant Multipole Resonances*, edited by S. Costaand C. Schaerf (Springer-Verlag, Berlin, 1977), p. 340.
[19] J. S. Levinger, Phys. Lett. B **82**, 181 (1979).
[20] J. Ahrens, H. Borchert, K. H. Czock, H. B. Eppler, H. Gimm, H. Gundrum, M. Kröning, P. Riehn, G. S. Ram, A. Zieger *et al.*, Nucl. Phys. A **251**, 479 (1975).
[21] https://www.maxlab.lu.se/node/1090
[22] J.-O. Adler, M. Boland, J. Brudvik, K. Fissum, K. Hansen, L. Isaksson, P. Lilja, L.-J. Lindgren, M. Lundin, B. Nilsson *et al.*, Nucl. Instrum. Methods Phys. Res., Sect. A **715**, 1 (2013).
[23] https://www.maxlab.lu.se
[24] L.-J. Lindgren, Nucl. Instrum. Methods Phys. Res., Sect. A **492**, 299 (2002).
[25] J.-O. Adler, B.-E. Andersson, K. I. Blomqvist, B. Forkman, K. Hansen, L. Isaksson, K. Lindgren, D. Nilsson, A. Sandell, B. Schröder *et al.*, Nucl. Instrum. Methods Phys. Res., Sect. A **294**, 15 (1990).
[26] J.-O. Adler, B.-E. Andersson, K. I. Blomqvist, K. G. Fissum, K. Hansen, L. Isaksson, B. Nilsson, D. Nilsson, H. Ruijter, A. Sandell *et al.*, Nucl. Instrum. Methods Phys. Res., Sect. A **388**, 17 (1997).
[27] J. P. Miller, E. J. Austin, E. C. Booth, K. P. Gall, E. K. McIntyre, and D. A. Whitehouse, Nucl. Instrum. Methods Phys. Res., Sect. A **270**, 431 (1988).
[28] F. Wissmann, V. Kuhr, O. Jahn, H. Vorwerk, P. Achenbach, J. Ahrens, H.-J. Arends, R. Beck, M. Camen, G. Caselotti *et al.*, Nucl. Phys. A **660**, 232 (1999).
[29] L. S. Myers, Ph.D. thesis, University of Illinois at Urbana-Champaign, 2010.
[30] L. S. Myers, G. Feldman, K. G. Fissum, L. Isaksson, M. A. Kovash, A. M. Nathan, R. E. Pywell, and B. Schröder, Nucl. Instrum. Methods Phys. Res., Sect. A **729**, 707 (2013).
[31] M. F. Preston, L. S. Myers, J. R. M. Annand, K. G. Fissum, K. Hansen, L. Isaksson, R. Jebali, and M. Lundin, Nucl. Instrum. Methods Phys. Res., Sect. A **744**, 17 (2014).
[32] S. Agostinelli, Nucl. Instrum. Methods Phys. Res., Sect. A **506**, 250 (2003).
[33] R. O. Owens, Nucl. Instrum. Methods Phys. Res., Sect. A **288**, 574 (1990).
[34] B. E. MacGibbon, Ph.D. thesis, University of Illinois at Urbana-Champaign, 1995.
[35] L. V. Hoorebeke, D. Ryckbosch, C. V. den Abeele, R. V. de Vyver, J. Dias, F. D. Smet, B. Schröder, and D. Nilsson, Nucl. Instrum. Methods Phys. Res., Sect. A **321**, 230 (1992).